Nanopatterning for Optoelectronic Manipulation of Organic Solar Cells

Dissertation submitted for the degree of Doctor of Natural Sciences (Dr. rer. nat.)

Presented by

Thomas Johannes Pfadler

at the

Universität Konstanz

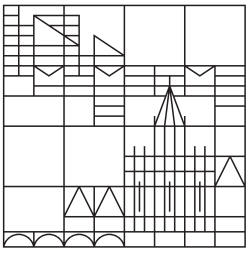

Faculty of Mathematics and Natural Sciences
Department of Physics

Date of the oral examination: December 4, 2015
First referee: Professor Dr. Lukas Schmidt-Mende
Second referee: apl. Professor Dr. Johannes Boneberg

Contents

Abstract

The rapidly advancing field of organic electronics has attracted increasing scientific as well as commercial interest during the last decades. Unique mechanical properties of organic semiconductors make them feasible for high-throughput roll-to-roll fabrication processes at low production costs. Modern nanotechnology is frequently applied to organic photovoltaics to investigate and to further improve this young and emerging technology.
This thesis focuses on nanostructure-induced optoelectronic manipulation of organic solar cells. Two approaches are employed to manipulate optical properties, i.e., the absorption behavior of organic thin-film photovoltaics.
First, the coherent electric-field distribution in (flat interfaces) 1D photonic multilayer solar cells is investigated both by experiment and simulation. For this purpose, the transparent indium tin oxide electrode is replaced and further compared to a novel high-performance and temperature-stable $TiO_2/Ag/TiO_2$ multilayer electrode. Such a multilayer electrode allows a decoupled optimization of absorption and photoexciton conversion process with respect to the employed photoactive material. A transfer-matrix algorithm is used to computationally maximize the photocurrent generation in the active medium of bulk heterojunction (BHJ) solar cells featuring a 1D photonic device configuration. The photocurrent maximization is accessible by increasing the electric field intensity in the active material by varying the $TiO_2/Ag/TiO_2$ multilayer electrode, thereby tuning the occurrence of coherent *Fabry-Perot* cavity modes. The decoupled optimization is succesfully shown by means of two very different state-of-the-art organic BHJ solar cell systems. Very good agreement between experiment and simulation is obtained validating the universality of the presented approach.
Second, periodically structured TiO_2 electrodes are introduced to thin-film photovoltaics to tackle the typically partial light absorption. Arising consequences on light management in such thin-film solar cells featuring a 2D photonic structure are elucidated. Wavelength-scale patterns are transferred to the electron-selective TiO_2 bottom electrodes via direct laser interference patterning. In the main absorption region of the employed photoactive materials, the efficiency of the structure-induced light in-coupling is spectroscopically shown to be determined by the refractive index n(active material) with respect to $n(TiO_2)$. The structuring is delineated to be beneficial for the total absorption enhancement if a high n active material is deposited on TiO_2, but detrimental for a low n material. Furthermore, the study outlines that the macroscopic Fresnel equations can be used to investigate the spectroscopically observed asymmetry in light in-coupling at the nanostructured TiO_2 active material interfaces by visualizing the difference in reflectivity caused by the asymmetry in refractive indices.
Beside the elucidation of light in-coupling in the main absorption region of the photoactive material, structure-induced light-trapping effects targeting at a resonant enhancement of the very weak tail-state absorption present in polymer:fullerene BHJ solar cells are additionally investigated. The presented approach paves the way to potentially close the gap between net optical and electric band gap of organic solar cells, which is stated as an intrinsic energy loss mechanism in donor-acceptor systems. Furthermore, fully vectorial electromagnetic simulations using the Discontinuous Galerkin Time Domain method were performed to obtain time-averaged Poynting vectors along with spatially resolved dependencies of the power loss densities. The simulations underline the experimental findings and further outline the tuneability of the absorption resonances towards arbitrary wavelength regions.

Electronic manipulation in terms of the macroscopic device performance of organic solar cells is achieved by artificially controlling the (n-type/p-type) donor-acceptor interfacial geometry on a nanometer scale. Comb-like bilayer all-polymer morphologies featuring a controlled enhancement in donor–acceptor interfacial area are experimentally realized and further employed as a model system to investigate the fundamental processes of exciton separation and polaron recombination. A unique processing methodology is introduced to obtain all-solution processed comb-like morphologies via nanoimprint lithography along with subsequent photo-crosslinking of the n-type polymeric bottom layer. The nanostructured topography of the n-type layer is thereby preserved even after solution coating of the p-type polymer on top. The different nanostructures are characterized locally by SEM/AFM, and the buried interdigitating interface of the final device architecture is statistically verified on a large area via advanced grazing incidence X-ray scattering techniques. Complementary optoelectronic characterization tools focusing on different working regimes of the solar cells give access to fundamental processes of exciton separation and polaron recombination. The results show equally enhanced harvesting of photoexcitons in both donor and acceptor materials directly correlated to the total enhancement of interfacial area. Apart from this beneficial effect, the enhanced interface leads to significantly increased polaron recombination losses both around the open-circuit voltage and maximum power point, which is determined in complement with diode dark current characteristics, impedance spectroscopy, and transient photovoltage measurements. From these findings it is inferred that a spatially optimized comb-like donor–acceptor nanonetwork alone is not the ideal morphology even though often postulated. Moreover, the energetic landscape has to be considered. A perfect morphology for an excitonic solar cell must be spatially and energetically optimized with respect to the donor–acceptor interface.

Zusammenfassung

Das sich rasch weiterentwickelnde Forschungsfeld der organischen Elektronik erregte in den letzten Jahrzehnten wissenschaftlich und auch wirtschaftlich zunehmend an Interesse. Einzigartige mechanische Eigenschaften organischer Halbleiter ermöglichen eine kostengünstige Rolle-zu-Rolle-Produktion mit hohem Durchsatz. Methoden der modernen Nanotechnologie finden häufig im Bereich der organischen Photovoltaik Anwendung und helfen dabei, diese junge und aufstrebende Technologie weiterzuentwickeln und zudem besser zu verstehen.
Gegenstand dieser Dissertation ist die nanostrukturierungsbedingte optoelektronische Modifikation von organischen Solarzellen. Zwei Ansätze werden verfolgt, um die optischen Eigenschaften, das heißt das Absorptionsverhalten von organischen Dünnschichtsolarzellen, zu modifizieren.
Zunächst wird die kohärente Verteilung des elektrischen Feldes in eindimensional photonischen Mehrschichtsolarzellen (mit flachen Grenzschichten) sowohl durch Experimente als auch durch Computersimulationen untersucht. Dazu wird die transparente Indiumzinnoxid (ITO)-Elektrode durch eine neuartige leistungsstarke und zudem noch temperaturstabile $TiO_2/Ag/TiO_2$ Mehrschichtelektrode ersetzt und außerdem verglichen. Diese Mehrschichtelektrode ermöglicht eine unabhängige Optimierung der Absorption und der Exzitonenausbeute unter Berücksichtigung der speziellen optoelektronischen Eigenschaften des jeweilig verwendeten photoaktiven Materials. Ein Transfermatrix-Algorithmus wird verwendet, um numerisch die Photostromgeneration im aktiven Medium von Bulk-Heteroübergang-Solarzellen zu maximieren, die einem als eindimensionale photonische Struktur zu bezeichnendem Aufbau folgen. Diese Photostrom-Erhöhung wird erreicht, indem die Intensität des elektrischen Feldes innerhalb der aktiven Schicht maximiert wird, was über eine Variation der $TiO_2/Ag/TiO_2$ Mehrschichtelektroden-Komposition und damit über eine Variation der kohärenten *Fabry-Perot-Resonatormoden* gesteuert wird. Diese unabhängige Optimierung wird erfolgreich an zwei verschiedenen dem aktuellen Stand der Technik entsprechenden Bulk-Heteroübergang-Solarzellensystemen exemplarisch durchgeführt. Eine sehr gute Übereinstimmung zwischen Experiment und Simulation konnte ermittelt werden, was die Allgemeingültigkeit des präsentierten Verfahrens unterstreicht.
Im zweiten Ansatz werden periodisch strukturierte TiO_2 Elektroden in Dünnschichtsollarzellen eingebaut, um der typischerweise spektral abhängigen unvollständigen Lichtabsorption entgegenzuwirken. Konsequenzen in Bezug auf das Lichtmanagement in zweidimensional-photonischen Dünnschichtsolarzellen werden somit untersucht. Wellenlängen großer periodischer Strukturen werden mithilfe direkter Laser-Interferenz-Musterung auf die elektronenselektiven TiO_2-Bodenelektroden übertragen. Spektroskopische Messungen belegen, dass die Effizienz der strukturell manipulierten Lichteinkopplung im Hauptabsorptionsbereich der jeweilig verwendeten photoaktiven Materialien vom Brechungsindex n des aktiven Materials selbst und dem des TiO_2 bestimmt ist. Es zeigt sich, dass die Strukturierung vorteilhaft für die absolute Absorptionserhöhung ist, wenn ein aktives Material mit hohem n (im Vergleich zu TiO_2) verwendet wird, jedoch von Nachteil für ein Material mit niedrigem n. Außerdem legt die Untersuchung dar, dass die makroskopischen Fresnel-Gleichungen herangezogen werden können, um die spektroskopisch bestimmte asymmetrische Lichteinkopplung an der nanostrukturierten TiO_2/aktives Material-Grenzschicht zu verstehen. Dies ist möglich durch eine Visualisierung des Unterschieds der Reflektivität aufgrund der asymmetrischen Brechungsindizes.
Neben dem Lichteinkopplungsverhalten im Hauptabsorptionsbereich der photoaktiven Materialien werden zusätzlich strukturell bedingte Effekte der resonanten Population, das heißt der Lichtkonzentration, von niederenergetischen und schwach absorbierenden Zuständen un-

tersucht, die speziell in Polymer-Fullerene-Bulk-Heteroübergang-Solarzellen zu finden sind. Diese Herangehensweise stellt eine neue Methode dar, um dem intrinsischen Energieverlust entgegenzuwirken, also dem Unterschied zwischen den tatsächlichen elektronischen und optischen Bandlücken in Donator-Akzeptor Systemen. Darüber hinaus werden voll vektorielle elektromagnetische Simulationen, die auf der "Discontinuous Galerkin Time Domain" Methode basieren, durchgeführt, um die zeitgemittelten Poynting-Vektoren und die damit verbundene ortsaufgelöste Energiedissipationsdichte zu ermitteln. Die Computersimulationen bestätigen die experimentellen Ergebnisse und zeigen ferner, dass die resonante Lichtkonzentration nahezu beliebig durchstimmbar ist.
Weiterhin werden elektronische Modifikationen, die sich in den makroskopisch messbaren Eigenschaften einer organischen Solarzelle widerspiegeln, aufgrund von künstlich auf der Nanometerskala kontrollierten (n-leitend/p-leitend) Donator-Akzeptor Grenzschichtgeometrien gesteuert. Kammartige Zweischicht-Polymer-Polymer-Morphologien, deren Grenzschichtfläche kontrolliert vergrößert wird, können experimentell hergestellt werden und dienen außerdem als ein Modelsystem zur Erforschung grundlegender Prozesse wie der Exzitonenausbeute und Polaronrekombination. Eine neuartige Prozessierungsmethode, basierend auf Nano-Imprint-Lithographie und anschließender lichtinduzierter Vernetzung des n-leitenden Materials, wird eingeführt, um rein lösungsprozessierte und kammartige Morphologien zu verwirklichen. Die Oberflächenstrukturierung der n-leitenden Polymerschicht bleibt durch die Vernetzung erhalten, selbst wenn das p-leitende Polymer aus einer Lösung auf die Nanostruktur aufgebracht wird. Die verschiedenen Nanostrukturen werden lokal mittels Rasterelektronen- und Rasterkraftmikroskopie charakterisiert. Die im Volumen versteckte und fingerförmig ineinandergreifende Grenzschicht der gefertigten Strukturen wird statistisch durch Rötengenstreuungsexperimente unter streifendem Einfall bestätigt. Komplementäre optoelektronische Messmethoden, die jeweils auf unterschiedliche Arbeitsbereiche der Solarzellen abzielen, werden verwendet, um Einblicke in grundlegende Prozesse wie die Exzitonenaufspaltung und Polaronrekombination zu erhalten. Die Ergebnisse zeigen eine gleichermaßen erhöhte Ausbeute an Exzitonen, sowohl aus dem Donator als auch aus dem Akzeptor, die sich direkt proportional zur Vergrößerung der absoluten Grenzschichtfläche verhält. Neben den Vorteilen, die eine vergrößerte Grenzschichtfläche bietet, führt diese auch zu erhöhten Polaronrekombinationsverlusten, sowohl unter Leerlaufbedingung, als auch am maximalen Leistungspunkt der Solarzelle, was komplementär mit Strom-Spannungsmessungen im Dunklen, Impedanzspektroskopie und zeitaufgelöster Photospannungsabfallmessungen ermittelt wird. Basierend auf diesen Messungen lässt sich ableiten, dass ein rein räumlich optimiertes, kammartiges Donator-Akzeptor Nanonetzwerk allein nicht die häufig als perfekt postulierte Morphologie darstellt. Darüber hinaus muss die energetische Potentiallandschaft beachtet werden. Die perfekte Morphologie für eine exzitonische Solarzelle kann demnach nur durch sowohl räumliche als auch energetische Optimierung der Donator-Akzeptor-Grenzschicht erreicht werden.

1. Introduction

The interdisciplinary field of modern *Nanotechnology* comprises science, engineering, and technology that all in common deal with controlled manipulation of matter on an atomic, molecular, and supramolecular scale[1]. One nanometer is a billionth (i.e., 10^{-9}) of a meter, abbreviated 1 nm.
The original motivation to investigate *Nanotechnology* was the idea to realize bottom-up fabrication processes of macroscale products by precisely controlling interactions and thereby the arrangement of atoms and molecules at the very first production level, i.e., the nanoscale building block alignment.[1, 2] Long before the term *Nanotechnology* was introduced by Norio Taniguchi, "On the Basic Concept of *Nano-Technology*", in 1974 and later by K. Eric Drexler in his ambitious and imaginative book "Engines of Creation: The Coming Era of Nanotechnology" in the late 1980s, the theoretical capability was already envisioned by physicist Richard Feynman with a talk entitled "There's Plenty of Room at the Bottom" at an American Physical Society meeting at the California Institute of Technology (CalTech) in 1959.[3–5] Richard Feynman introduced his avant-garde ideas with the words: "What I want to talk about is the problem of manipulating and controlling things on a small scale. [...]In the year 2000, when they look back at this age, they will wonder why it was not until the year 1960 that anybody began seriously to move in this direction."[5]
Nowadays we know that it took another two decades of research until microscopes were developed that allowed to "see" and to further manipulate nanoscale objects even down to the atomic scale. This was an imperative necessity for modern *Nanotechnology* to be born. Although scanning electron microscopy (SEM) was commercially available as early as 1965, it was the groundbreaking invention of the scanning tunneling microscope (STM) by Gerd Binnig and Heinrich Rohrer in the early 1980s at *IBM Research-Zürich* and the subsequent development of atomic force microscopy (AFM) by Gerd Binnig, Calvin F. Quate, and Christopher Gerber in 1986 that made modern *Nanotechnology* accessible.[6–8]
The development of the transistor[2] and the subsequent findings in semiconductor technology on the detrimental role of impurity atoms in bulk silicon, that macroscopically cause the difference between n-type or p-type functionality, impressively show the key role of modern *Nanotechnology* to manipulate matter on an atomic scale.[9] Especially the successful miniaturization of transistors down to dimensions of 50 nm

[1] atomic; on the order of $\sim 10^{-10}$ m
molecular; on the order of $\sim 10^{-9}$ m
supramolecular; on the order of $\sim (10^{-9}$ - $10^{-7})$ m

[2] Invented in 1947 by John Bardeen, Walter Brattain, and William Shockley. A transistor is a semiconductor component which can be used to switch and to amplify electronic signals.

(i.e., $\sim$ 100 atoms) with very smooth oxide layers of less than 2 nm need to be attributed to modern *Nanotechnology*.[9]
Another example of progress in semiconductor technology is reflected in the rapid development of photovoltaic cells specifically over the last two decades. Therefore the "Progress in Photovoltaics" has been updated every six months for a range of photovoltaic devices and module technologies since 1993.[10] Besides the impressive development of crystalline silicon, alternative low-cost solar cells have been investigated in order to be competitive with conventional energy generation in terms of the levelized cost of energy (LCOE)[3].[11] In 1991, Brian O'Regan and Michal Grätzel published their work on conceptual novel solar cells, "A low-cost, high-efficiency solar cell based on dye-sensitized colloidal TiO_2 films".[12] Their and also the success of modern *Nanotechnology* is based on the preparation of transparent thin-films of high interfacial area TiO_2 nanostructures decorated with a covalently bound monolayer of an organic charge-transfer dye to sensitize these films for efficient light harvesting. Different low-cost thin-film solar cells based on photoactive in-organic and/or organic semiconductors have been successfully investigated in the last two decades.[10] Such thin-film solar cells basically feature inorganic/organic multilayer structures consisting of functionally aligned material combinations with layer thicknesses on the order of 10 nm - 100 nm.
In the context of modern *Nanotechnology* and additionally well-fitting to the recent *United Nations* resolution[4] entitled "**International Year of Light and Light-based Technologies, 2015**" to highlight the importance of light and optical technologies to the world citizens, this dissertation investigates the controlled manipulation of optoelectronic properties of organic thin-film solar cells.

Outline of the Thesis

An introduction along with a theoretical description of basic working principles of excitonic (e.g., organic) solar cells is given in section 2. Subsequently, important computational as well as experimental methods which are employed in this work are summarized in section 3. Section 4 focuses on the investigation of manipulated absorption properties of organic thin-film devices, and section 5 on electronic device properties of artificially nanostructured solar cells. A final conclusion and outlook is given in section 6.
"Nanopatterning for Optoelectronic Manipulation of Organic Solar Cells" is the title of this thesis. Two approaches are employed to manipulate the optical properties, i.e., the absorption behavior of organic thin-film photovoltaics. First, the coherent electric-field distribution (cf. section 4.1) in 1D photonic multilayer solar cells is investigated both by experiment and simulation. For this purpose, the transparent indium tin oxide (ITO) bottom electrode is replaced and further compared to a transparent $TiO_2/Ag/TiO_2$ multilayer electrode. This novel sandwich electrode is examined to possibly allow a decoupled optimization of absorption and photoexciton conversion process with respect

[3] levelized cost of energy (LCOE), i.e., \$/MWh
[4] The resolution A/RES/68/221 proclaiming the international year of light (IYL) 2015 was accepted on 20 December 2013 at a plenary meeting of the 68th Session of the UN (United Nations) General assembly.[13]

to specific optoelectronic properties of photoactive layers sandwiched between bottom and backelectrode (i.e., backmirror). A transfer-matrix algorithm is used to computationally maximize the photocurent generation in the active medium of bulk heterojunction (BHJ) solar cells featuring a 1D photonic device configuration by varying the TiO_2/Ag/TiO_2 multilayer electrode, thereby tuning the occurrence of coherent *Fabry-Perot* cavity modes. Second, periodically structured TiO_2 electrodes are introduced to thin-film photovoltaics to tackle the typically present and spectrally dependent partial light absorption. Arising consequences on light management (i.e., light in-coupling and light-trapping) in such thin-film solar cells featuring a 2D photonic structure are examined. Wavelength-scale patterns are transferred (cf. section 3.3) to electron-selective bottom electrodes via direct laser interference patterning. The efficiency of structure-induced light in-coupling (cf. section 4.2.2) is spectroscopically investigated as a function of the refractive indices n_i of different photoactive materials deposited on top with respect to the structured TiO_2 bottom layer. Additionally, structure-induced light-trapping effects (cf. section 4.2.3) to obtain resonant absorption enhancement in BHJ solar cells featuring a 2D photonic structure are investigated in detail. Beside experiments, fully vectorial electromagnetic simulations using the Discontinuous Galerkin Time Domain (DGTD) method were performed to obtain time-averaged Poynting vectors along with spatially resolved dependencies of the power loss densities as a function of the specific 2D photonic geometry.
Electronic manipulation in terms of the macroscopic device performance (cf. section 5) of organic solar cells is elucidated by artificially controlling the donor-acceptor interfacial geometry on a nanometer scale. Comb-like bilayer all-polymer morphologies featuring a controlled enhancement in donor–acceptor interfacial area are experimentally realized via nanoimprint lithography (cf. section 3.5). Different nanostructures are characterized locally by SEM/AFM, and the periodic patterns are statistically examined on a large area via advanced grazing incidence X-ray scattering techniques. Furthermore, complementary optoelectronic characterization tools focusing on different working regimes of the solar cells are employed to give access to the fundamental processes of exciton separation and polaron recombination in such a model system for an excitonic solar cell.

2. Excitonic Solar Cells

Organic semiconductors are widely used in organic electronic devices such as solar cells or light emitting diodes. Generally speaking, the term "organic" originates from the field of organic chemistry that deals with carbon atoms and their respective single, double or triple bonds. The optoelectronic properties of organic semiconductors arises from the presence of delocalized π-electrons, which originate from the hybridisation of atomic orbitals of carbon atoms when forming chemical bonds with each other or with hydrogen atoms for instance.[14] Molecules with alternating single and multiple bonds (i.e., conjugated organic molecules) feature an extended system of delocalized π-electrons.
The most famous conjugated molecule is the polymer polyacetylene. The semiconducting properties of polyacetylene was investigated by Shirakawa, Heeger, and MacDiarmid in the late 1970s.[15–17] Later, in the year 2000, Shirakawa, Heeger, and MacDiarmid were awarded the Nobel Prize in Chemistry for the discovery and development of "Conductive Polymers".

2.1. External and Internal Quantum Efficiency

The introduction, i.e., the first paragraph of this section is based on the research paper *Influence of interfacial area on exciton separation and polaron recombination in nanostructured bilayer all-polymer solar cells* which I have written as part of my Ph.D.[18] For this study I fabricated all solar cells and did most of the measurements for data shown in the publication. *M. Coric* did initial experiments and optimization. I wrote the manuscript and was responsible for editing.

Thin-film solar cells have the potential to deliver cheap and clean energy by converting the incident solar flux into electrical current. The mechanism of photocurrent harvesting in a solar cell is based on the photovoltaic effect that involves the generation of electrons and holes in a semiconductor device under illumination and the subsequent extraction of the charge carriers at their respective electrodes. Organic solar cells are often classified as excitonic solar cells owing to their distinctively different charge carrier separation mechanism compared to conventional pn junction solar cells.[19] The binding energy of coulombically bound electron-hole pairs (i.e., excitons) in this class of solar cells cannot be thermally overcome and excitons need to be separated with help of the electrochemical driving force given at a type II heterojunction cf. Figure 2.2).[20] Such strongly bound excitons that typically occur in low dielectric constant organic semiconductors are referred to as *Frenkel Excitons*, in contrast to weakly bound *Wannier Excitons* which are present in most inorganic semiconductors.[21] In

1986, Tang et al. presented an organic bilayer heterojunction (Figure 2.1a) device based on the subsequent vacuum evaporation of copper phthalocyanine (CuPc) and a perylene tetracarboxylic derivative (PV).[22] This research outlined the importance of a second organic semiconducting layer on the charge generation efficiency in organic solar cells. In 1995, Yu et al. elucidated the high quantum efficiency of exciton separation in blends of poly(2-methoxy-5-(2'-ethyl-hexyloxy)- 1,4-phenylene vinylene) (MEH-PPV) and phenyl-C61-butyric acid methyl ester ($PC_{61}BM$) at the timescale of photoinduced charge transfer across the donor-acceptor heterojunction that is more than 10^3 times faster than the radiative or non-radiative decay of photoexcitons in these systems.[23] Simultaneously, Yu et al. prooved the concept of efficient charge separation that exclusively occurs at a type II heterojunction for an all-polymer MEH-PPV and cyano-polyphenylene vinylene (CN-PPV) bulk-heterojunction (BHJ) (Figure 2.1b) device.[24] Detailed studies on the limiting influence of exciton diffusion, e.g., the spatial donor-acceptor phase-separation in MEH-PPV and CN-PPV BHJ solar cells were performed by Halls and co-workers who recognized that the exciton diffusion range is typically one order of magnitude smaller than the optical absorption depth, thus limiting efficient exciton separation.[25] Brabec et al. further investigated the influence of phase-separation in bulk heterojunction (BHJ) solar cells and found that the choice of solvent offers the possibility to indirectly control the macro-phase-separation, improving the overall device performance of BHJ solar cells.[26] The necessity of a two-phase morphology which provides a donor-acceptor interface for efficient photoconversion due to charge carrier separation gives rise to four different morhoplogical concepts which are schematically shown in Figure 2.1.
The simplest configuration (Figure 2.1a) features a bilayer or planar heterojunction

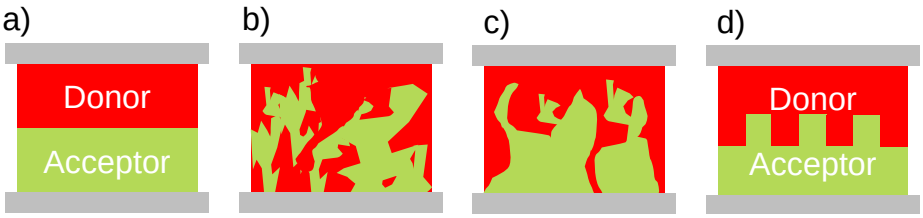

Figure 2.1.: Schematic of morphological architectures used in organic solar cells. **a)** flat interface organic bilayer, **b)** bulk heterojunction (BHJ), **c)** back-infiltrated, and **d)** comb-like donor-acceptor architecture.

between two strictly phase-separated electron donating and accepting materials. On the one hand, the beneficial built-in continuity of the respective material phase provides direct percolation pathways for polarons (i.e., charge carriers) to the respective electrodes. On the other hand, the so called exciton bottleneck, i.e., the typical relatively long optical absorption length ($L_A \approx 50\ nm$) compared to the typical length scale for exciton diffusion ($L_D \approx 10\ nm$) limits efficient exciton harvesting in bilayer architectures to excitons photogenerated within L_D with respect to the donor-acceptor interface. [27–29]
The BHJ architecture (Figure 2.1b) consists of spontaneously phase-separated inter-

penetrating donor-acceptor networks, ideally featuring phase-separations on the order of L_D. This architecture greatly benefits from the increased interfacial area since the probability for exciton harvesting, i.e., exciton diffusion towards the donor-acceptor interface and the subsequent exciton dissociation is proportional to the overall amount of donor-acceptor interfaces within the bulk of the active material.[30–32] BHJs are typically fabricated by solution casting a blended solution of donor and acceptor materials or by thermal co-evaporation. Therefore, a phase continuity to the respective electrodes is not necessarily provided as indicated in Figure 2.1b.
Recently, high interfacial area back-infiltrated (Figure 2.1c) donor-acceptor architectures which intrinsically feature a built-in continuity of the respective material phases were introduced.[33, 34] A detailed description of the back-infiltration methodology is given in section 3.6.
The comb-like donor-acceptor architecture (Figure 2.1d) is often hypothetically regarded as the perfect morphology, since the exciton bottleneck can be potentially overcome due to a highly ordered spatial arrangement (with respect to L_D) of donor and acceptor materials in lateral direction and vertically optimized towards maximum absorption. An in-depth investigation of comb-like donor-acceptor architectures is given in section 5.1 and summarized in Figure 5.13.
The external quantum efficiency (EQE) of an organic solar cell can be expressed as a product of the efficiencies η_i (cf. Figure 2.2) of single processes involved from light absorption to current extraction.[35, 36]

$$\eta_{\mathrm{EQE}} = \eta_{\mathrm{absorption}} \cdot \eta_{\mathrm{IQE}} \tag{2.1}$$

Where η_{IQE} describes the internal quantum efficiency which is determined by processes that are covered by the electronic properties of the photoactive materials and the spatial ordering of the donor-acceptor network.[37]

$$\eta_{\mathrm{IQE}} = \eta_{\mathrm{exiton\ diffusion}} \cdot \eta_{\mathrm{exciton\ dissociation}} \cdot \eta_{\mathrm{charge\ collection}} \tag{2.2}$$

Note, the validity of equations 2.1 and 2.2 is not restricted to excitonic solar cells. For a conventional silicon-based pn-junction for instance, the efficiency of single excitonic processes are negligible due to the dominant generation of weakly bound and strongly delocalized *Wannier Excitons* upon light absorption, therefore:
$\eta_{\mathrm{exiton\ diffusion}} \cdot \eta_{\mathrm{exciton\ dissociation}} \simeq 1$. Generally speaking, η_{EQE} is defined as the number of photogenerated electrons in the external circuit of the device normalized to the number of incident photons and η_{IQE} correspondingly as:

$$\eta_{\mathrm{EQE}} = \frac{\text{number of photogenerated electrons per second}}{\text{number of incident photons per second}} \tag{2.3}$$

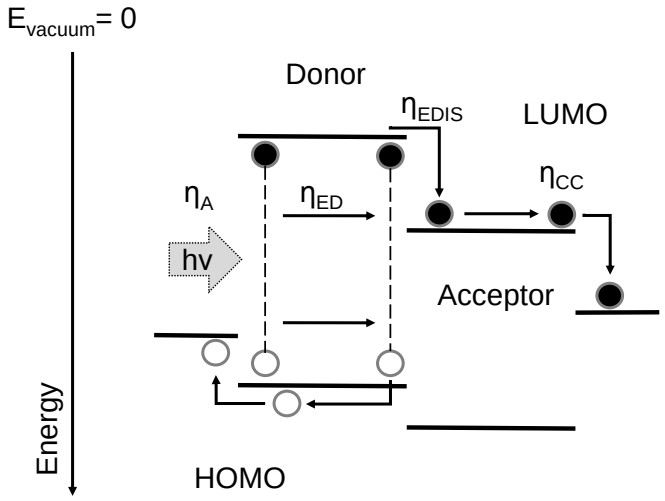

Figure 2.2.: Simplified schematic of photoconversion in an organic solar cell with the processes of photon absorption η(A), exciton diffusion η(ED), exciton dissociation η(EDIS) by charge transfer, and charge carrier collection η(CC) denoted. Compare to equation 2.1 and 2.2. Based on Menke and Holmes.[38]

$$\eta_{\mathrm{IQE}} = \frac{\text{number of photogenerated electrons per second}}{\text{number of absorbed (within active material) photons per second}} \tag{2.4}$$

Section 3.2 provides a detailed discussion how to model photocurrent action spectra and thereby η_{EQE} in organic BHJ devices featuring a 1D photonic structure.

2.2. Absorption of Electromagnetic Radiation

The interaction of semiconductors with electromagnetic radiation plays a decisive role for an optoelectronic device such as a solar cell. The spectral range of electromagnetic radiation with relevance to a solar cell's power generation is determined by the incident solar spectrum. The spectral ranges of interest are ultraviolet (UV), visible (VIS), and near infrared (NIR).[1] In 1961 Shockley and Queisser presented an upper theoretical limit for the efficiency of a silicon pn-junction solar cell based on the laws of thermodynamics by using a detailed-balance approach.[40] Therefore, a system is described where absorption and emission from a solar cell take place across a single band gap with $\eta_{\mathrm{IQE}} = 1$ (cf. equation 2.2) above the optical bandgap. The maximum achievable efficiency was calculated as a function of the semiconductor's bandgap $\mathrm{E_{gap}}$, the sun and the cell were assumed to be blackbodies with temperatures of 6000° K and 300° K,

[1] UV: $\lambda = 250 - 400\ nm$, i.e., $E = 3 - 5\ eV$
VIS: $\lambda = 400 - 800\ nm$, i.e., $E = 1.6 - 3\ eV$
NIR: $\lambda = 800 - 2000\ nm$, i.e., $E = 0.6 - 1.6\ eV$ (from [39])

respectively. The maximum efficiency of a single absorber junction device was found to be 30 % corresponding to an optimized E_{gap} of 1.1 eV. Recently, Koster and co-workers extended the Shockley and Queisser approach to maximize the efficiency of organic donor-acceptor BHJ devices as a function of $E_{gap,\ donor}$ and $E_{gap,\ acceptor}$, respectively and δ_{LUMO} ($\equiv$ $LUMO_{donor}$ - $LUMO_{acceptor}$; Figure 2.2)[2].[42] In BHJ devices, most of the photocurrent is generated through light absorption by the donor and/or acceptor, but most of the electroluminescence (i.e., radiative recombination) is due to emission of an interfacial (donor-acceptor) lower energy charge-transfer (CT) state.[43–45] In other words, absorption and emission in excitonic solar cells takes place at different energies and transitions between very different states are involved. Koster et al. included the classic *Marcus Theory* for the description of interfacial exciton dissociation and recombination.[42, 46] Based on their approach, a maximum efficiency of around 20 % is estimated for an optimized BHJ system with $E_{gap,\ donor} = E_{gap,\ acceptor} = 1.4$ eV and δ_{LUMO}=0.15 eV.[42]
The absorption coefficient α [m^{-1}] is related to intrinsic material properties, which are macroscopically described by the complex refractive index $\tilde{n}$ as follows [47]:

$$\alpha = \frac{4 \cdot \pi \cdot k}{\lambda} \tag{2.5}$$

where $\tilde{n} = n + ik$. Experimentally, the absorption $Abs(\lambda)$ can be approximated from a measurement of the absorbance $A(\lambda)$ obtained from the total transmittance $T(\lambda)$ through bulk samples (reflection is included):

$$Abs(\lambda) \simeq 1 - T(\lambda) \simeq 1 - 10^{-A(\lambda)} \tag{2.6}$$

$$A(\lambda) = \alpha \cdot x \simeq -\log_{10}\left(\frac{I_1(\lambda)}{I_0(\lambda)}\right) \tag{2.7}$$

where x is the thickness of the absorbing medium, $I_0(\lambda)$ denotes the incident intensity and $I_1(\lambda)$ the transmitted intensity of an absorbing medium upon illumination. Equation 2.7 is based on the well known *Beer-Lambert* law.[48, 49]
More precisely, $A(\lambda)$ can be defined in terms of the internal transmittance $\tilde{T}$ (i.e., the radiant flux Φ_e^e of energy emitted by a sample related to the radiant flux of energy received Φ_e^r by that sample (reflection is excluded):

$$\tilde{T} = \frac{\Phi_e^e}{\Phi_e^r} = 10^{-A(\lambda)} \tag{2.8}$$

Note, internal transmittance describes energy loss due to absorption, whereas the total transmittance is that due to absorption, reflection, and scattering.[50] Based on the above considerations concerning accurate absorbance measurements (i.e., to account

[2]Note, from a energetic point of view, the lowest unoccupied molecular orbital (LUMO) and highest occupied molecular orbital (HOMO) in organic semiconductors corresponds to the conduction and the valence band of inorganic semiconductors, respectively.[41]

for reflection of the samples) an integrating sphere in double-beam mode (sample and reference beam) is necessary as described in section 3.1 and 4.2.2.

2.3. Exciton Diffusion

As discussed in the previous section 2.1 the limitation of the exciton diffusion length L_D ($\approx 10\ nm$) in the context of the exciton bottleneck limits the absorption-diffusion efficiency product $\eta(\mathrm{A}) \cdot \eta(\mathrm{ED})$ (Figure 2.2 and equation 2.1) thereby η_{EQE}. If organic materials could be realized with enhanced $\mathrm{L_D}$ which is comparable to the absorption length $\mathrm{L_A}$ of the respective organic semiconductor, even simple bilayer devices as shown in Figure 2.1a could be realized with an absorption-diffusion efficiency product close to unity.
In the following section, different energy transfer mechanisms which are considered to be responsible for exciton migration along with a simplified exciton diffusion model are discussed. A detailed description of the involved energy transfer mechanisms and an in-depth differentiation of singlet and triplet excitons can be found for instance in the textbook of Turro et al., and the topic of exciton diffusion in organic solar cells was recently reviewed by Mikhnenko et al., and Menke and Holmes.[38, 51, 52] Note, a singlet exciton is always generated upon light absorption in the first place (optical transition rule), but triplet or charge transfer excitons are not further discussed in this section on exciton diffusion due to their similarity to singlets in the context of basic working mechanisms in excitonic solar cells.
Three types of energy transfer mechanisms are considered to be responsible for exciton migration: cascade energy transfer, Förster resonant energy transfer (based on Coulomb interactions), and Dexter energy transfer (mediated by electron exchange interactions). Cascade energy transfer involves the emission and subsequent reabsorption of a photon between a donor and an acceptor molecule. Note, in this section on diffusive motion of excitons, an acceptor molecule refers to a neighboring molecule in the same material phase and does not necessarily refer to an molecule in the n-type acceptor phase. Cascade energy transfer can occur over long length scales comparable to the absorption length and should be considered when there is a reasonable overlap between the absorption and emission spectra of the organic material, i.e., if a material shows a small Stokes shift.[53]
Förster resonant energy transfer is a non-radiative energy transfer that is mediated by the Coulombic coupling of the electromagnetic field between donor and acceptor. This energy transfer can be mechanistically treated as the emission and subsequent reabsorption of a virtual photon. Therefore, a spectral overlap between the luminescent excited donor molecule and the ground state acceptor molecule is crucial. Förster approximated the energy transfer rate with a pair of weakly coupled point dipoles.[54] The rate equation for Förster resonant energy transfer is expressed in terms of the exciton

lifetime (τ), the intermolecular separation (d), and the Förster radius (R_0) as follows:

$$k_F(d) = \frac{1}{\tau} \cdot \left(\frac{R_0}{d}\right)^6 \tag{2.9}$$

The Förster radius R_0 is defined as:

$$R_0^6 = \frac{9 \cdot \eta_{PL} \cdot \kappa^2}{128 \cdot \pi^5 \cdot n^4} \cdot \int \lambda^4 \cdot F_D(\lambda) \cdot \sigma_A(\lambda) d\lambda \tag{2.10}$$

where η_{PL} is the photoluminescence efficiency of the excited state, κ^2 is the dipole orientation factor, n is the refractive index at the spectral position where the spectral overlap integral is maximized, λ the wavelength, F_D is the normalized donor fluorescence, and σ_A is the absorption cross section of the acceptor molecule. Note, the assumption of weakly coupled dipoles breaks down if the intermolecular spacing is more and more reduced, since higher order multi-pole interactions start to play a significant role for the description of Coulombic interactions between molecules. However, Förster resonant energy transfer typically occurs over a relatively long length scale (R_0 = 1 - 10 nm) in comparison to typical intermolecular spacings ($d \lesssim 1$ nm).[52, 55–58]
Dexter energy transfer theory (also referred to as Dexter electron transfer) describes direct electron transfer between an excited molecule and an nearby ground state acceptor molecule that is based on orbital interactions.[59] Therefore, the overlap between the electron densities of both excited donor and the ground state acceptor molecule is required to describe the electron transfer. The rate equation for Dexter energy transfer is expressed as follows:[51]

$$k_D(d) = K \cdot J \cdot \exp(-\frac{2 \cdot d}{L}) \tag{2.11}$$

where d is the intermolecular separation, K is related to the specific orbital interaction, J is the normalized (to the extinction of the acceptor at the ground state) spectral overlap integral, and L is the van der Waals radius. Dexter energy transfer is a short-range (compared to Förster transfer) nearest-neighbor process with length scales of around $0.1 - 1$ nm.[55] Note, Dexter energy transfer can occur between states that are non-radiative, therefore it is thought to be the underlying mechanism for the migration of long-life triplet excitons.[55]
In literature, there is a huge variety of theoretical descriptions of exciton diffusion with varying degrees of complexity.[60–63] Generally speaking, diffusion is a random motion of particles in space that leads to a particle redistribution from areas of high concentration to areas of low concentration driven by the gradient in particle density.[52] Exciton diffusion can be described as an ensemble of hopping events (e.g., exclusively between nearest neighbors) identical to a random walk.[53] Therefore, the above discussed nanoscopic energy transfer mechanisms (cascade energy transfer, Förster resonant energy transfer, and Dexter energy transfer) can be connected to mesoscopic exciton transport, if exciton diffusion is modeled as an ensemble of self-energy transfer hopping events on a cubic lattice for instance. Following Ahn et al. a generalized

diffusion coefficient D can be written as follows:[64]

$$D = \frac{A}{6} \sum_{N} d^2 \cdot k_{ET}(d) \tag{2.12}$$

where the factor A is accounting for disorder, d is the distance of a single hop, and k_{ET} is the energy transfer rate to a specified lattice point of set N. Furthermore, in the absence of second order processes such as annihiliation and fission for instance, exciton diffusion can be modeled with a second order differential equation as follows:[38]

$$\frac{dn}{dt} = D \cdot \bigtriangledown^2 n(r) - \frac{n(r)}{\tau} + G(r) \tag{2.13}$$

where n is denoted as the exciton density, τ is the exciton lifetime, r is the position in space, and G is the exciton generation rate. The first term on the right represents exciton diffusion which is driven by the gradient in exciton density, the second term accounts for exciton recombination, and the third term represents excition generation (equation 3.11) upon photon absorption as discussed in section 3.2. Finally, the characteristic length scale for exciton diffusion, the exciton diffusion length L_D, can be written as follows:

$$L_D = \sqrt{D \cdot \tau} \tag{2.14}$$

As mentioned in the beginning of this section on exciton diffusion, L_D is a very critical material property for organic semiconductors employed in photovoltaics, since it reflects the characteristic distance over which an exciton can migrate thereby limiting the absorption-diffusion product (i.e., the exciton bottleneck) with respect to the employed donor-acceptor architecture (cf. Figure 2.1) for a specific material composition.

2.4. Exciton Dissociation

The primary process in electrical power generation of solar cells is the utilization of incident solar energy to generate free electronic charges in a semiconducting device. As already mentioned in the previous section 2.1, organic solar cells are often classified as excitonic solar cells due to their relatively high exciton binding energies (E_B^{exc}) in comparison to the thermal energy ($k_\mathrm{B}T$) at room temperature ($E_B^{exc} \gg k_\mathrm{B}T \backsimeq 25$ meV) of photogenerated excitons along with the consequences on exciton dissociation (Figure 2.3). Therefore, excitons play a decisive (even limiting) role as previously discussed in the context of the exciton bottleneck (section 2.3).
The attractive electron-hole Coulomb interaction (i.e., E_B^{exc}) needs to be overcome for efficient exciton dissociation. Following a simple point charge picture, the Coulomb potential (V_C) of an exciton can be described as follows:[65]

$$V_C(r) = \frac{e^2}{4 \cdot \pi \cdot \epsilon_r \cdot \epsilon_0 \cdot r} \tag{2.15}$$

where e is the elementary charge, ϵ_r is the dielectric constant of the surrounding medium, ϵ_0 is the permittivity of free space, and r is the electron-hole separation distance. As discussed by Gregg, the fundamental different working principles of organic solar cells in comparison to their inorganic counterparts arises from the difference in E_B^{exc} (i.e., V_C).[19] The difference in V_C (equation 2.15) is caused by the intrinsic dielectric screening porperties of the employed materials on the one hand, which is macroscopically expressed by ϵ_r, and additionally due to the difference in localization (i.e., the average r in equation 2.15) of the involved electronic states on the other hand.
Overcoming the Coulomb attraction in solar cells based on silicon pn junctions for in-

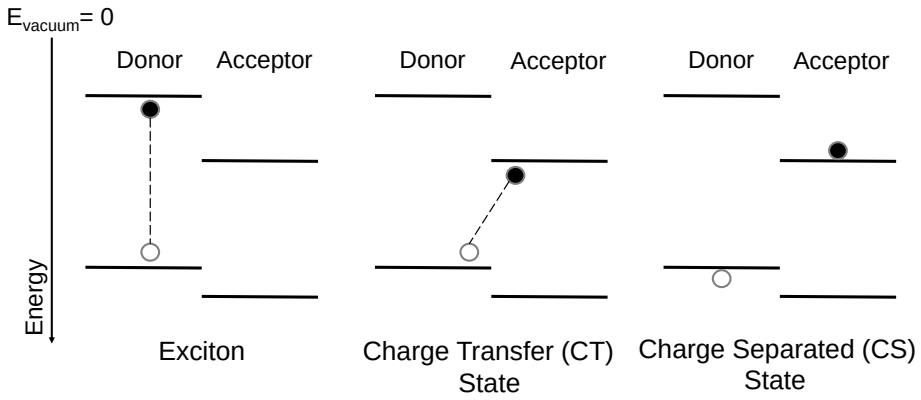

Figure 2.3.: Simplified schematic of an exciton, a charge transfer state, and a charge separated state at an organic donor-acceptor interface. Coulomb attraction is indicated as a dashed line and the exciton and CT binding energies are indicated due to the vertical position of the electron as well as the hole with respect to the molecular energy levels, respectively. The CT state can be split up if the energy gain due to the occupation of the final CS state ("free" electron and hole polaron in the acceptor and donor, respectively) exceeds the binding energy of the charge transfer state. Based on Schmidt-Mende and Weickert.[66]

stance, is facile due to the high dielectric screening ($\epsilon_r \backsimeq 12$) and because the involved electronic states already being highly delocalized.[67] However, overcoming the Coulomb attraction in solar cells based on molecular materials is significantly more demanding due to their typically smaller dielectric screening ($\epsilon_r \backsimeq 2-4$) and because of the more localized nature of the involved electronic states. In literature, there is a huge variety of theoretically calculated and experimentally determined values for E_B^{exc} ranging from less than 0.1 eV to over 1 eV for conjugated polymers such as poly(para-phenylene vinylene) (PPVs) for instance.[68, 69] The binding energy for a CT state (E_B^{CT}) is usually estimated to be lower than E_B^{exc}, due to the increased electron-hole separtion distance at the donor acceptor interface (Figure 2.3). Literature values for E_B^{CT} ranging from 0.1 eV to 0.5 eV are typically estimated.[70–73] However, source of differing results, at least partially originate from the disordered nature of polymers, different processing conditions, different donor-acceptor ratios, different raw material sources, and different materials that all together influence the morphology and thereby the observed properties. For instance, Loi et al. noted that the CT state energy can be tuned by altering the

blend composition in a F8DTBT:PCBM BHJ device.[74] The reduction of CT state energy due to an enhanced PCBM concentration in polymer:fullerene BHJs was observed by different groups and is attributed to effectively increased ϵ_r and higher delocalization (average r in equation 2.15) of electronic states in PCBM.[75–77] The shown state

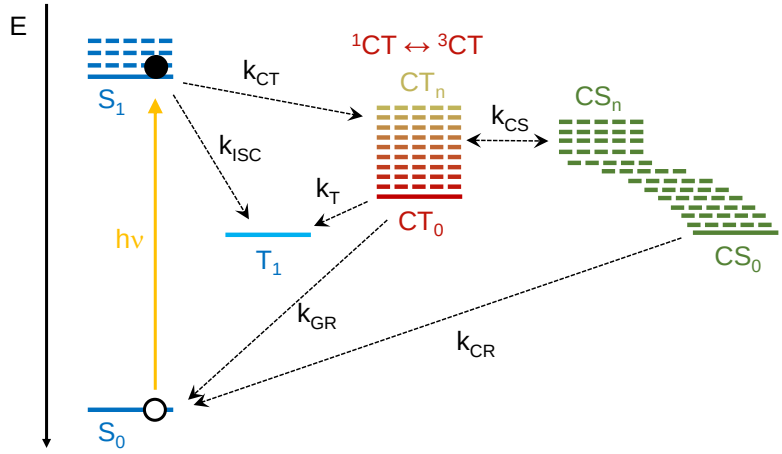

Figure 2.4.: State energy level diagram showing the kinetic competition of processes occuring during charge photogeneration in organic solar cells. After photoexcitation a charge transfer state can be populated, followed by separation of electron and hole into a charge separated state (cf. Figure 2.3). Based on intersystem crossing (ICS) it is also possible that a singlet-triplet transission occurs. Depending on the donor-acceptor combination there is a certain energy distribution of CT states and an activation energy is necessary in order to reach a charge separated (CS) state from the lowest charge transfer state CT_0. Based on Schmidt-Mende and Weickert.[66]

energy level diagram (Figure 2.4) summarizes the contemporary picture of all competing dynamic processes (for different rates k) involved in charge separation at an organic donor-acceptor interface. For simplicity, formation of excitons in the acceptor phase are neglected. Therefore, the absorption of a photon in the donor (Figure 2.3) promotes the generation of the S_1 singlet exciton (Figure 2.4) due to the photoexcitation of an electron from the donor's HOMO into the LUMO. This donor S_1 state can be quenched due to an electron transfer from the donor (at a rate k_{CT}) to the acceptor by forming an interfacial CT_n state at different thermal excitation levels that are often referred to as *cold* (n=0) and *hot* (n=1,2,3,...). Based on the relatively weak electronic coupling, a reasonable rapid spin mixing between its singlet (^{1}CT) and triplet states (^{3}CT) is considered and thereby the transition from ^3CT_n states to the lowest triplet state T_1 in the donor can occur at a reasonable rate k_T.[78, 79] Beside the transition to the T_1 state, CT_n states can undergo geminate recombination to form the S_0 ground state at a rate k_{GR}. Note, the energy of the CT_0 state can be experimentally determined from its radiative recombination (i.e., electroluminescence) to the S_0 ground state.[80] Alternatively, CT_n states can undergo transitions to one of many possible CS_n states and vice versa at rates k_{CS}. Furthermore, charge separated states CS_n can undergo non-geminate charge recombination at a rate k_{CR}.

The complexity of the state energy level diagram (Figure 2.4) along with the kinetic competition of different pathways and most importantly the difference of the investigated material systems limits a clear understanding of charge photogeneration in organic solar cells, which is therefore still under debate. Object of discussion between the two school of thought is the question whether CS_n is populated from the lowest (thermally relaxed and more localized) CT_0 state or from a hot (and more delocalized) CT_n state.[81–83]
A fundamental theoretical description on electron-hole separation has been proposed by Onsager in 1938 and was extended by Braun in 1984.[84] The Onsager-Braun theory treats an electron-hole pair as a pair of point charges bounded through attractive Coulomb interaction (equation 2.15). The charge carriers are considered to be free if a critical radius (r_c) is reached that corresponds to a Coulomb potential which is equal to the thermal energy k_BT. A probability distribution for charge separation is obtained that depends on the initial thermalization length r_a ($r_a < r_c$). Based on the work of Braun and Tachiya, the initial probability distribution was modified by a possible deformation of the attractive Coulomb potential in the presence of an electric field.[85, 86] Furthermore, finite lifetimes of the excited electron-hole pair along with geminate and non-geminate recombination of charge carriers were considered. However, a quantitative description of experimental values typically fails for organic systems, most likely due to energetic disorder, hence overestimating r_c.[87–89]

2.5. Charge Collection

So far, the previous topics of this section on working principles of excitonic solar cells focused on donor-acceptor architectures with respect to their spatial and energetic arrangements to realize efficient exciton harvesting upon photoexcitation. As already mentioned in the discussion of the different morphologies employed in organic solar cells (section 2.1), a phase continuity of the respective donor and acceptor phases is detrimental for the photoconversion process (Figure 2.2) including efficient charge carrier (i.e., polaron) collection at the respective electrodes. Generally speaking, the exciton dissociating donor-acceptor interface needs to be "wired" to the electrodes. Note, in contrast to a conventional silicon pn junction, an organic donor-acceptor solar cell is a majority charge carrier device with electron polarons exclusively in the n-type phase and hole polarons in the p-type phase due to the asymmetry in exciton dissociation at the donor-acceptor interface.[19] Geminate (cf. Figure 2.4) and non-geminate recombination in organic solar cells featuring a bicontinuous phase-separation is dominated by recombination channels at interfaces as discussed by Street and Schöndorf.[90] However, a clear molecular-level picture which provides a full theoretical understanding of recombination mechanism in organic solar cells is absent as recently reviewed.[91] Lakhwani and co-workers elaborated how recombination dynamics turn out to be dependent on mobility, temperature, electric field, charge carrier concentration, and trapped charges.[91] However, non-geminate (i.e., bimolecular) recombination is found to be the dominant recombination channel in optimized organic solar cells at short-circuit conditions.[31, 92] Furthermore, as shown by Credington and Durrant, bimolecular recombination effec-

tively controls the J-V characteristics moving from short-circuit to open-circuit conditions: the charge density within the photoactive layer increases, thereby bimolecular recombination which is accompanied by a decreasing fill factor.[92] Many theoretical descriptions on bimolecular recombination were originally derieved for amorphous silicon (charge carrier mobilities of about 10 cm^2 V^{-1} s^{-1}, but were modified with respect to the specific properties of organic semiconductors.[93–95] Opposite to high-mobility semiconductors where direct tunneling recombination is dominant, Langevin theory (developed in 1903) can be applied to describe recombination in low-mobility semiconductors, since the likelihood of opposite charges to find each other and to recombine depends on the charge carrier concentration and the relative mobility of electron and hole polarons.[96] Early work in the late 1960s on crystalline organic semiconductors (e.g., on anthracene single crystals with mobilites of around 1 cm^2 V^{-1} s^{-1}) successfully showed the feasibility of Langevin theory.[97–100] However, Langevin theory turned out to be incongruous for the description of disordered and very low-mobility organic semiconductors like polymeric systems. Note, the hole mobility in P3HT for instance has been measured to be about $3 \cdot 10^{-4}$ cm^2 V^{-1} s^{-1}.[101, 102] Figure 2.5 summarizes different developed recombination models, which comprise very low-mobility (i.e., hopping transport), energetic disorder and an donor-acceptor interface. A detailed comparison of the different models was recently reviewed by Lakhwani et al.[91] As mentioned above, charge transport in semiconductors can differ by several orders of magnitude. On the one hand, charge carrier mobilities in doped and highly ordered inorganic semiconductors like germanium for instance can exceed 1000 cm^2 V^{-1} s^{-1}.[103] Such a strongly undisturbed charge transport is known as a band-like transport and is theoretically described by the propagation of highly delocalized plane waves which can be scattered at inpurities or interact with phonons. On the other hand, charge transport in highly disordered (e.g., organic) semiconductors can be completely dominated by scattering. Therefore, charge carriers effectively travel via hopping from one site to another at very low macroscopic, i.e., supramolecular mobilities on the order of 10^{-4} cm^2 V^{-1} s^{-1}.[101, 102] Anisotropic charge carrier mobilities with respect to molecular alignment and a more detailed discussion on charge transport in organic semiconductors can be found for instance in the reviews of Coropceanu et al. and Bässler and Köhler.[104, 105]

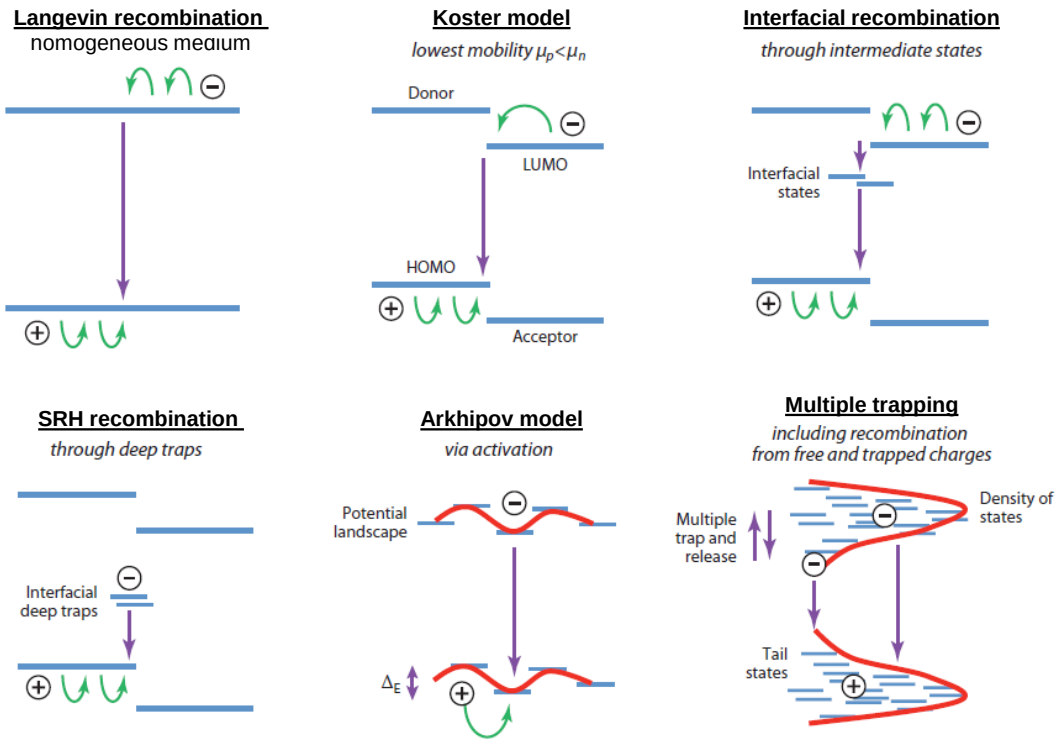

Figure 2.5.: Schematic representation of different bimolecular recombination models. These models were established or further developed to account for the influence of mobility, temperature, electric field, charge carrier concentration, trapped charges, and energetic disorder which is present in disordered and very low-mobility semiconductors as employed in organic solar cells. Based on Lakhwani et al.[91]

3. Methods

This section summarizes important experimental as well as computational methods, which play a key role in the following sections of this dissertation. Section 4 focuses on the investigation of manipulated absorption properties of organic thin-film devices and section 5 on electronic device properties of artificially nanostructured solar cells.

3.1. Optoelectronic and Structural Characterization Tools

The following description of optoelectronic and structural characterization tools is partly based on the research papers *Influence of interfacial area on exciton separation and polaron recombination in nanostructured bilayer all-polymer solar cells* and *A comparison of light-coupling into high and low index nanostructured photovoltaic thin films* which I have both written as part of my Ph.D. I wrote the manuscripts and was responsible for editing.[18, 106]

J-V and EQE spectra were recorded using an automated LabView program controlling a Keithley 2400 sourcemeter. J-V characterization under illumination was acquired using a 150 W Xe lamp solar simulator. A Frauenhofer Institute certified Si reference solar cell equipped with a KG5 filter was used for calibration. Dark diode characteristics were similarly recorded, but the devices were shielded from illumination. Spectrally resolved EQE measurements (compare to section 2.1) were performed using a xenon white light source focused into a grating monochromator (LOT-Oriel Omni 150) equipped with a set of appropriate edge pass filters. Cells were illuminated through a shadow mask with an illuminated area of 0.125 cm^2 according to the device characterization guidelines by Snaith.[107] All measurements were done at room temperature.
Microscopic quantum processes which are affecting the macroscopic J-V and EQE device characteristics will be discussed in detail using artificially nanostructured solar cells featuring a controlled enhancement of donor-acceptor interfacial area in section 5.2. Further details on the lay out of the employed set-up can be found in the dissertation of the constructor Holger Hesse.[108]

Transient Photovoltage (TPV) measurements allow for the investigation of polaron recombination kinetics directly in the time domain under quasi-open circuit conditions.[109] A pulsed (10 Hz, 532 nm) laser with approximately 4 ns pulse length was focused onto the solar cells. Devices were background-illuminated with a solar simulator (LOT-Oriel LS0106) with an AM 1.5G solar spectrum and a light intensity of 100 mW cm^{-2}.

Signals were recorded with a digital oscilloscope (Tekscope DPO 7254) and a termination resistance of 1 MΩ was used. All measurements were done at room temperature.
A schematic of the set-up along with an in depth analysis of experimental data on artificially nanostructured solar cells are discussed in section 5.2 and summarized in Figure 5.10. Further details on the lay out of the employed set-up can be found in the dissertation of the constructor Holger Hesse.[108]

Impedance Spectroscopy (IS) gives experimental access to characterize solar cells under working conditions.[110–112] Impedance spectra were recorded with an Ecochemie Autolab Potentiostat/Galvanostat. Devices were put in a light-tight grounded metal box and illuminated with a white light diode with approximately 100 mW cm^{-2} (adjusted using a silicon reference diode), characterized at different applied biases (0.2 V - 0.45 V) and frequencies (1 MHz – 10 Hz). Data modeling was done using the software *ZView*. All measurements were done at room temperature.
A schematic of the set-up along with an in depth analysis of experimental data on artificially nanostructured solar cells are discussed in section 5.2 and summarized in Figure 5.11. Further details on the employed set-up can be found in the Master thesis of Michael Puls and Eugen Zimmermann, respectively.[113, 114]

Photoluminescence Measurements. Steady state photoluminescence (PL) were measured using a Horiba Jobin Yvon Fluorolog-3 Fl3-122 spectrometer equipped with a 500 W halogen lamp. Details on PL measurements can be found for instance in the textbook of Klingshirn.[115] Samples were illuminated from the front side (not through the glass substrate) under an angle of 30° and the signal was detected under an angle of 60° in order to avoid direct reflection of the excitation light into the emission channel. Appropriate long pass filters were additionally placed in the emission channel. Spectra were typically recorded with step width of 1 nm - 5 nm and integration times of 0.1 s - 2 s per data point. All measurements were done at room temperature.
Experimental data on artificially nanostructured solar cells are discussed in section 5.2 and summarized in Figure 5.9.

Total Absorption measurements were performed by either measuring the total reflection at the backport of an integrating sphere (150 mm diameter) or inside the integrating sphere with help of a *Center Mount Sample Holder*. Substrate sizes were 14×14 mm^2 but a shadow mask defines the illuminated area to be typically 0.5 cm^2. The spectroscopy system is a double-beam (sample and reference beam) CARY 5000 UV-VIS-NIR. Samples were masked, the default zero/baseline (white reflectance standard) correction was applied and the minimum in absorption for each spectra was linearly downshifted to zero absorption, respectively. Note, the total absorption A_{tot} is determined by measuring the total reflectance R_{tot} (A_{tot} = 1 - R_{tot}) since the transmission through the Ag back-reflector can be neglected as shown by Snaith et al.[116] Therefore, A_{tot} is measured in units of absorbance $A(\lambda)$ (equation 2.6).

Polarization-dependent total absorption measurements: Incident light is parallelized through appropriate lenses and polarized through a Glan-Taylor Polarizer placed in front of the integrating sphere. The polarization-dependent total reflection at the back-port of the integrating sphere was recorded for polarizer positions ranging from 0° to 180°. Since the intensity of the sample beam was polarization-dependent, the baseline (white reflectance standard) was recorded for each polarization and used to normalize each polarization scan, respectively. Finally, the background (baseline) is estimated and removed by fitting a second order polynomial to the spectra by minimizing a non-quadratic cost function following Mazet et al.[117]
Quantitative total absorption measurements play a decisive role in section 4 when 1D and 2D photonic structures are investigated in thin-film photovoltaics for the purpose of light-management to obtain absorption enhancement. All measurements were done at room temperature.

Atomic Force Microscopy (AFM) topographies were recorded using a Bruker Multimode 6 AFM in tapping mode. Scans were typically realized on $(1\mu\text{m} - 5\mu\text{m})^2$. Especially, topographic height variations on a nanometer scale can be determined even though convolution of tip shape on sample topography needs to be considered.[118, 119]

Scanning Electron Microscopy (SEM) was carried out with a *Zeiss Ultra high resolution FESEM* in the *Nanostructure Laboratory* at the *University of Konstanz* at acceleration voltages of 1 kV - 10 kV and working distances of 1 mm - 5 mm. Samples were placed on steel stubs with the help of carbon tape and approximately 2 nm Au were sputtered onto the samples to suppress charging effects if necessary. Sample structures are imaged by scanning it with a focused high energy electron beam. The interaction with the sample atoms contains informations about the sample surface topography and material compositions.[120]

Variable Angle Spectroscopic Ellipsometry (VASE). Details on ellipsometry can be found for instance in the textbook of Tompkins.[121] Wavelength dependent n and k values (refractive index: $\tilde{n} = n + ik$) for the different materials (Sb_2S_3, P3HT:$PC_{61}BM$, TiO_2; deposited on Si [100]) discussed in section 4.2.2 (shown in Figure 4.10a and appendix Figure B1) were measured by VASE Ellipsometry on a *Nanofilm Ellipsometer Version EP3* in the *Nanostructure Laboratory* at the *University of Konstanz*. The optical parameters, Ψ and Δ, were obtained for 60° to 80° angle of incident and for wavelengths between 400 nm and 880 nm. The n and k values were batch-fitted to a Fresnel model with a fixed layer thickness. The layer thicknesses were obtained beforehand by AFM measurements. All fits have small RMSE (< 5) and the absolute deviation for n and k is 2 %, respectively.

Advanced Scattering Experiments using X-Rays. The reciprocal space structure characterization was performed i.a., in collaboration by *Claudia M. Palumbiny* under supervision of *Prof. Peter Müller-Buschbaum* from the *Technical University of Munich*

(TUM). The analytical techniques are discussed in section 5.1 along with experimental data concerning artificially nanostructured interfaces in all-polymer solar cells and further summarized in a broader context in the final report of the SPP1355 (a priority program of the DFG funding research on basics of organic solar cells).[122] The data is shown in Figure 5.5 and 5.6, respectively.
Grazing incidence resonant soft X-ray scattering (GI-RSoXS) was used at the synchrotron beamline 11.0.1.2 of the Advanced Light Source (ALS) at the Berkeley National Laboratory (LBNL) in Berkeley (USA). The measurement set-up is under high vacuum due to the high absorption of soft X-rays in air. The energy of the X-rays was stepwise altered around the resonant scattering of carbon from 283 to 284 eV (4.381 to 4.366 nm) with a step size of 0.1 eV. An incident angle $\alpha_i = 5°$ was chosen for all measurements. The strongest contrast between P(NDI2OD-T2) and P3HT near the carbon K edge was found to be at 283.8 eV. The scattering signal was collected by a CCD camera with a size of 2048 pixel x 2048 pixel (pixel size of 13 μm x 13 μm). The measuring time was 20 s. Grazing incidence small angle X-ray scattering (GISAXS) measurements were performed at the beamline 7.3.3. at the ALS at the LBNL in Berkeley. The sample-detector distance was chosen to be 3549.24 mm using an evacuated flight tube and a Pilatus 1M detector. The X-ray energy was 10 keV and the incident angle was varied in steps of 0.01° from 0.1° to 0.4°. Typically an angle of 0.16° is used under these conditions for polymeric systems.

3.2. Transfer-Matrix Algorithm to Simulate Coherent Electric-Field Distributions in 1D Photonic Structures

The following section describes the employed transfer-matrix formalism to simulate optical electric-field intensity distributions and corresponding absorption in flat interface multilayer solar cells (i.e., 1D photonic structures). A more detailed description concerning this formalism is given by Pettersson et al., and Peumanns et al.[27, 123] Burkhard et al. later used this formalism to make accurate IQE measurements by simulating absorption profiles and further provid the employed Matlab script for download.[124, 125] Fundamental assumptions are firstly that all employed materials are homogeneous, isotropic and can therefore be macroscopically described by a complex index of refraction $\tilde{n}$ and secondly, that all interfaces are optically flat. Note, $\tilde{n} = n + ik$, where n is the real part of the refractive index and k is the imaginary part, the so called extinction. Both are directly related via the *Kramers–Kronig relations* to intrinsic dielectric material properties.[126] The attenuation of a propagating electromagnetic wave is related to the extinction k, whereas the phase velocity within a medium and furthermore the refraction at an interface of two media is determined by the real refractive indices n. A 1D photonic solar cell structure is sandwiched between two semi infinite layers ($j = 0$ /glass, $j = m + 1$ /air) as shown in Figure 3.1. Note, the $j = m$ layer in thin-film solar cells is typically a 150 nm thick metal (Ag, or Al) backcontact. For the simulation, it is assumed that the light source is in an n=1 environment (air) and that the first layer is a thick superstrate (e.g., glass), so that incoherent reflection from the air/1st

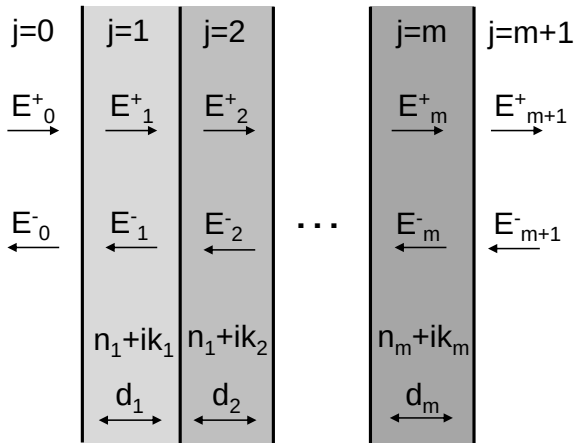

Figure 3.1.: Geometry of the 1D photonic multilayer stack used in the optical electric-field calculations. It is assumed that all materials are homogeneous and isotropic and that all interfaces are optically flat. 1D photonic solar cell structures are sandwiched between two semi infinite layers ($j = 0$ /glass, $j = m + 1$ /air). Based on Peumanns et al.[27]

layer interface is taken into account before the coherent interference is calculated in the remaining layers. The 1D photonic structure is illuminated from the left side (i.e., in positive x-direction) along the surface normal.
At the interface between layer i and j the change of the electrical field is given by the interface matrix $I_{i,j}$ as follows:

$$\begin{pmatrix} E_i^+ \\ E_i^- \end{pmatrix} = I_{i,j} \cdot \begin{pmatrix} E_j^+ \\ E_j^- \end{pmatrix} = \begin{pmatrix} \frac{1}{t_{i,j}} & \frac{r_{i,j}}{t_{i,j}} \\ \frac{r_{i,j}}{t_{i,j}} & \frac{1}{t_{i,j}} \end{pmatrix} \begin{pmatrix} E_j^+ \\ E_j^- \end{pmatrix} \tag{3.1}$$

The electrical field amplitude of a propagating wave in the positive x-direction is denoted by E^+ and the one propagating in the negative x-direction is denoted by E^- and the indices (i, j) denote the respective layer. The coefficients $r_{i,j} = \frac{\tilde{n}_i - \tilde{n}_j}{\tilde{n}_i + \tilde{n}_j}$ and $t_{i,j} = \frac{2 \cdot \tilde{n}_j}{\tilde{n}_i + \tilde{n}_j}$ are the complex Fresnel reflection and transmission coefficients for normal incidence of light.[127]
The layer matrix L_j accounts for the caused phase shift and attenuation of the propagating plane wave within layer j.

$$L_j = \begin{pmatrix} e^{-ik_j d_j} & 0 \\ 0 & e^{ik_j d_j} \end{pmatrix} \tag{3.2}$$

where $k_j = \tilde{n}_j \cdot \frac{2\pi}{\lambda}$ is the wavevector of the plane wave in the medium j and d_j is the respective layer thickness as sketched in Figure 3.1.
The electric field in the two outermost layers ($j = 0$ and $j = m+1$) of the 1D photonic structure are related to each other via the transfer-matrix S:

$$\begin{pmatrix} E_0^+ \\ E_0^- \end{pmatrix} = S \cdot \begin{pmatrix} E_{m+1}^+ \\ E_{m+1}^- \end{pmatrix} \tag{3.3}$$

$$S = I_{0,1} \cdot L_1 \cdot I_{1,2} \cdot ... \cdot L_m \cdot I_{m,m+1} \tag{3.4}$$

In order to attain the electric field in one specific layer j the S-matrix is noted as follows:

$$S = S_j^- \cdot L_j \cdot S_j^+ = \begin{pmatrix} S_{11} & S_{12} \\ S_{21} & S_{22} \end{pmatrix} \tag{3.5}$$

where S_j^- contains all matrices up to layer j and S_j^+ contains all matrices from layer j to $m+1$. The total electrical field at an arbitrary position in layer j is given in terms of the incident wave by:

$$E_j(x) = E_j^+(x) + E_j^-(x) \tag{3.6}$$

$$= \left(t_j^+ e^{ik_j x} + t_j^- e^{-ik_j x} \right) E_0^+ \tag{3.7}$$

where $t_j^{\pm}$ denote the transmission coefficient for all layers up to layer j in positive (+) and negative (-) x-direction,

$$t_j^+ = \frac{E_j^+}{E_0^+} = \frac{\frac{1}{S_{j11}^-}}{1 + \frac{S_{j12}^- S_{j21}^+}{S_{j11}^- S_{j11}^+} \cdot e^{2ik_j d_j}} \tag{3.8}$$

$$t_j^- = \frac{E_j^-}{E_0^+} = t_j^+ \cdot \frac{S_{j21}^+}{S_{j11}^+} \cdot e^{2ik_j d_j} \tag{3.9}$$

where $S_j^{\pm}$ denote the matrix entries of the $S_j^{\pm}$ matrices. The described formalism enables to calculate the coherent electric field distribution of a 1D photonic solar cell as exemplarily shown in Figure 3.2 for an inverted organic P3HT:$PC_{61}BM$. The time averaged absorbed power Q at an arbitrary position is then calculated as follows:

$$Q_j(x, \lambda) = \frac{4\pi \cdot c \cdot \epsilon_o \cdot k_j \cdot n_j}{2\lambda} \cdot |E_j(x, \lambda)|^2 \tag{3.10}$$

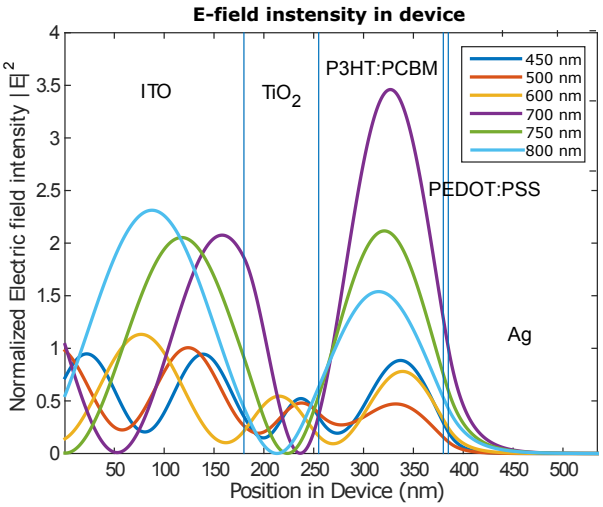

Figure 3.2.: Simulated electric field distribution in the 1D photonic solar cell structure: glass|ITO(180 nm)|TiO_2(75 nm)|P3HT:PC_{61}BM(125 nm)|PEDOT:PSS(5 nm)|Ag(150 nm). Reprinted with permission from Pfadler et al.[106] Copyright (2015), AIP Publishing LLC.

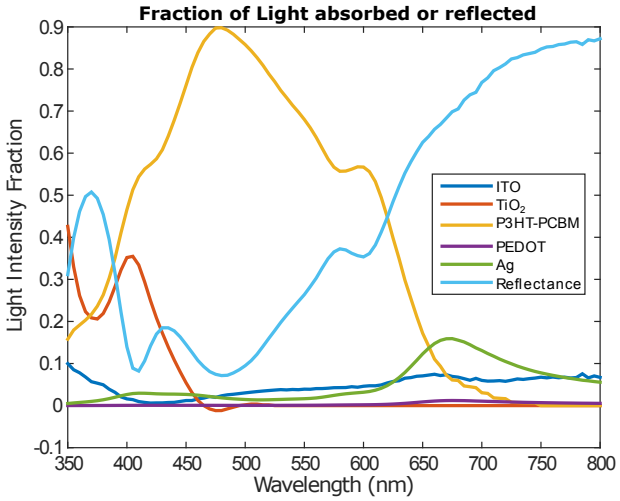

Figure 3.3.: Simulated absorption in the 1D photonic solar cell structure: glass|ITO(180 nm)|TiO_2(75 nm)|P3HT:PC_{61}BM(125 nm)|PEDOT:PSS(5 nm)|Ag(150 nm). Reprinted with permission from Pfadler et al.[106] Copyright (2015), AIP Publishing LLC.

where c is the speed of light, ϵ_o is the permittivity of free space, λ is the wavelength and $E_j(x, \lambda)$ is determined in equation 3.7. Based on equation 3.10 the corresponding absorption to the electric field distribution shown in Figure 3.2 can be determined as shown in Figure 3.3. The exciton generation rate at an arbitrary position $G_j(x, \lambda)$ for

the respective layer is consecutively attained from:

$$G_j(x,\lambda) = \frac{\lambda}{h \cdot c} \cdot Q_j(x,\lambda) \tag{3.11}$$

One approach to obtain an upper limit for the generated photocurrent $J^{photo}(\lambda)$ and correspondingly η_j^{EQE} of a 1D photonic solar cell featuring only one ($j = k$) active layer (e.g., an organic BHJ device) reads as follows:

$$J_{j=k}^{photo}(\lambda) = q \cdot \int G_{j=k}(x,\lambda) \cdot \eta_{j=k}^{\mathrm{IQE}} dx \tag{3.12}$$

where q is the elementary charge and $\eta_{j=k}^{\mathrm{IQE}}$ (equation 2.2) needs to be fixed. The η_j^{EQE} is defined as the number of photogenerated electrons in the external circuit (per second) normalized to the number of incident photons (per second), therefore

$$\eta_{j=k}^{\mathrm{EQE}}(\lambda) = \frac{J_{j=k}^{photo}(\lambda)/q}{\frac{1}{2} \cdot c \cdot \epsilon_{\mathrm{o}} \left|E_0^+(\lambda)\right|^2 \cdot (h \cdot c/\lambda)^{-1}} \tag{3.13}$$

i.e., generated photocurrent density in the active layer of the BHJ device with respect to the incident spectral photon flux. Where c is the speed of light, ϵ_{o} is the permittivity of free space, λ is the wavelength, q is the elementary charge and h is Planck's constant. Note, BHJ devices with η_{IQE} approaching 100 % have been reported by Park and co-workers.[35] The presented approach will be used in section 4.1.2 in order to investigate the potential photocurrent maximization for representative polymer:fullerene BHJ devices as a function of the design of the employed transparent electrode in a 1D photonic structure arrangement. Note, any incident solar spectrum $S(\lambda)$ (e.g., the AM 1.5G) can be considered by multiplying $G_{j=k}(x,\lambda)$ in equation 3.12 with $S(\lambda)$. Furthermore, equation 3.12 is exclusively valid for optimized BHJ devices, where resulting exciton populations in the respective layers do not necessarily have to be considered.
Peumanns et al. discussed a more general approach, where the exciton population (i.e., the exciton density) for each layer is considered and the continuum steady-state exciton diffusion equation (compare to equation 2.12) for every layer j along with appropriate boundary conditions is determined.[27] The J_j^{photo} contribution from a DA interface for instance is calculated from the exciton diffusion current towards this interface.

3.3. Direct Laser Interference Patterning

The description of the direct laser interference patterning (DLIP) processing is based on work presented in the research paper *A comparison of light-coupling into high and low index nanostructured photovoltaic thin films* which I have written as part of my Ph.D.[106] The laser structuring was realized in collaboration with *Martin Stärk* under supervision of *Prof. Johannes Boneberg* at the *University of Konstanz*. I wrote the

manuscript and was responsible for editing.

Direct laser interference patterning is a versatile technique, which enables the direct transformation of various interference patterns to the surface of different materials such as metals, semiconductors, polymers, ceramics, and magnetic thin films.[128–131] In

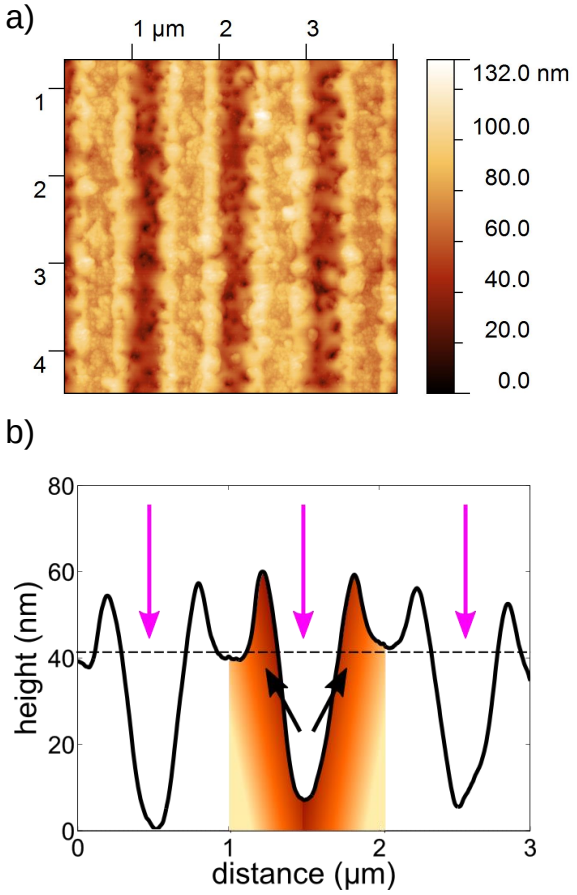

Figure 3.4.: AFM topographic height profile of laser structured TiO_2 (a) where too much energy was deposited. **(b)** The shown profile is statistically averaged over 750 AFM line scans. The pink arrows indicate the maxima of the interference pattern, whereas the black arrows indicate the direction of lateral material redistribution. The former flat surface line is sketched (dashed line) as a guide for the eye. Reprinted with permission from Pfadler et al.[106] Copyright (2015), AIP Publishing LLC.

this work, we use two-beam interference patterning to structure an approximately 60 nm thick layer of anatase TiO_2. A schematic of the DLIP set-up is shown in Figure 4.7a. The patterning is realized by using a Q-switched Nd:YAG laser, which produces 12 ns pulses at 10 Hz repetition rate. The fourth harmonic of the infrared fundamental beam (1064 nm) is chosen, due to the strong absorption of TiO_2 at 266 nm. The samples are placed on a vertically aligned x-z stage (laser beam in the x-y plane). The laser

beam on the sample is approximately 2 mm in diameter, whereas the lateral intensity distribution follows a Gaussian beam profile. Therefore, a spacing of x=1 mm (x-z position table) is chosen and the stage is moved with a velocity v_z=2 mm s^{-1}. The grooves are aligned along the z-direction of the stage. The laser fluence is typically around 100 mJ cm^{-2}. Preliminary results on laser patterning of anatase TiO_2 are shown in Figure 3.4, which shows an AFM topographic height profile of a patterning pre experiment where too much energy was deposited. The statistically averaged (750 line scans) topographic line section (Figure 3.4b) shows a lateral redistribution of the TiO_2. The pink arrows indicate the maxima of the interference pattern (equation 3.14). We sketched the black arrows, which indicate the direction of material redistribution that is driven by the thermal gradient (color gradient in Figure 3.4b). Note, both incident beams in our two-beam interference set-up (Figure 4.7a) show identical energy, polarization, and phase due to the arrangement of the beam splitter and subsequent symmetric propagation pathes for the two beams, respectively. Therefore, the intensity distribution and corresponding maxima of the two-beam interference pattern can be determined as shown in the dissertation of *Stephen Riedel*:[132]

$$I(x) = 2 \cdot I_0 \{cos(2 \cdot k \cdot x \cdot sin\Theta) + 1\} = 4 \cdot I_0 \cdot cos^2(k \cdot x \cdot sin\Theta) \tag{3.14}$$

where I_0 is denoted as the intensity of one single beam, $k = \frac{2\pi}{\lambda}$, and the angle of incidence Θ with respect to the surface normal.

$$d = \frac{\lambda}{2 \cdot sin\Theta} \tag{3.15}$$

The obtained intensity distribution of the two-beam interference arrangement shows a periodic pattern with maxima in intensity $I_{max} = 4 \cdot I_0$ and a periodicity d.

3.4. Discontinuous Galerkin Time Domain Method

The following section on the Discontinuous Galerkin Time Domain (DGTD) method is based on the research paper *Structure induced Resonant Tail-State Absorption in Polymer:Fullerene Bulk-heterojunction Solar Cells* which I have written as part of my Ph.D.[133] The computational examination was performed by *Thomas Kiel*, *Julia Werra* under supervision of *Dr. Christian Matyssek* in the group of *Prof. Kurt Busch* at the *Humbold-Universität zu Berlin* and the *Max Born Institute Berlin*. I wrote the manuscript and was responsible for editing. The technique is used in section 4.2.3 to obtain time-averaged Poynting vectors along with spatially resolved dependencies of the power loss densities of solar cells featuring a 2D photonic structure.

We model the electromagnetic propagation in the solar cells presented in section 4.2.3 by using a Discontinuous Galerkin Time-Domain method (DGTD).[134–136] From the solution of the fully vectorial Maxwell equations, the absorption spectra, time averaged power-loss density and Poynting vector are calculated. For modelling purposes we approximate the laser-patterned centimetre large chip as a translationally invariant structure in direction orthogonal to the structuring (y-direction). Therefore, it is sufficient to model the two-dimensional unit cell with periodic boundary conditions in the second lateral direction (x-direction). In the propagation direction of the exciting radiation (z-direction) we terminate the domain by perfectly matched layers (PML) approximating an infinitely large domain.[137, 138] The different material interfaces are either approximated as entirely flat or - for the structured interfaces - by a cosine-shaped boundary. The complete structure is finally discretized by triangular tesselation (see Figure 3.5) using the software Trelis.
The different material layers are presented in Figure 3.5. The glass substrate (subdivided into three layers) is followed by a layer of ITO (thickness d = 180 nm), a structured layer of TiO_2 (socket: 15 nm, cosine peak-to-peak amplitude: 100 nm), the structured active layer of P3HT-PCBM (d = 125 nm), a layer of PEDOT:PSS (d = 10 nm) and finally capped with a layer of silver (150 nm minimal thickness). The simulation domain is then terminated by layers of air. The exemplary periodicity shown in Figure 3.5 is chosen as 470 nm.

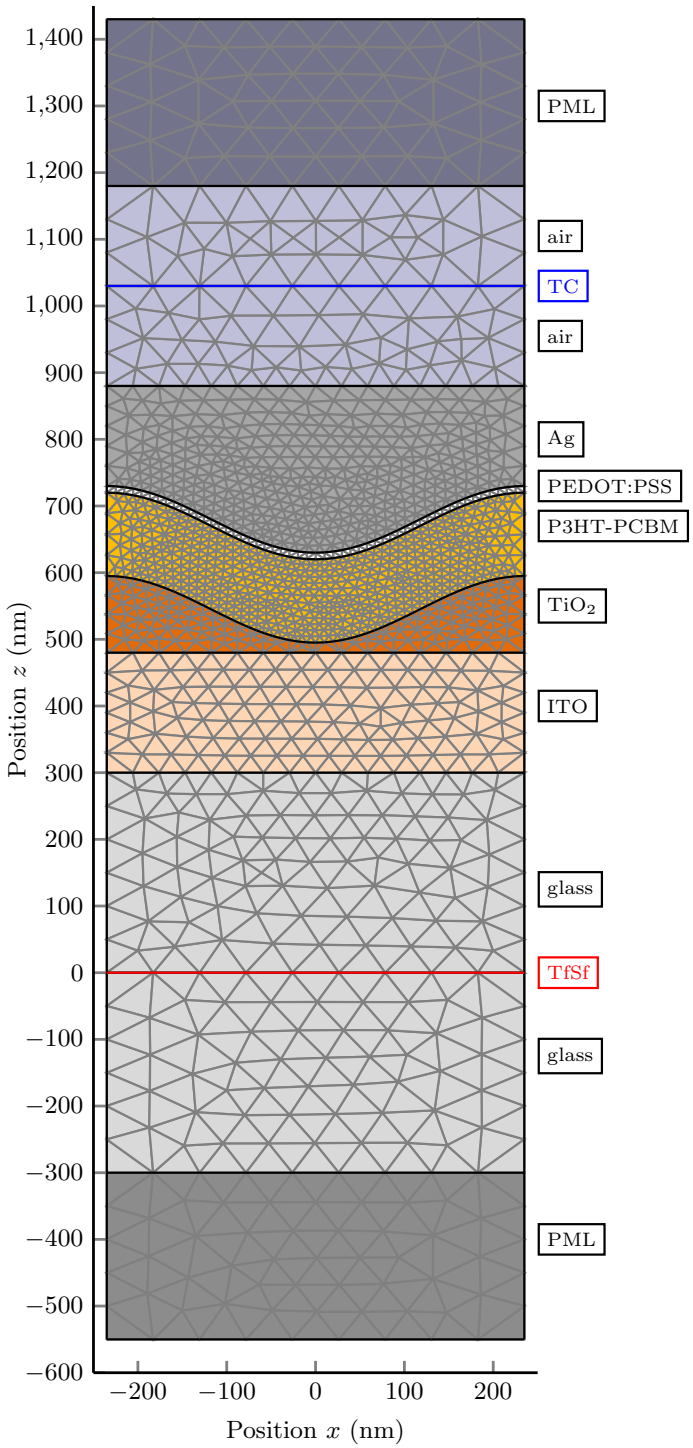

Figure 3.5.: Mesh of the unit cell used within the DGTD method to solve the Maxwell equations for the 470 nm periodic solar cell presented in the corresponding section 4.2.3. Besides from the different material layers, the total-field/scattered-field contour (TfSf, red line) for the incident field induction and reflectance calculation as well as the contour for the transmittance calculation (TC, blue line) are shown. Note that the incident field is launched from the the TfSf contour in the upward direction. Adapted from Pfadler et al.[133]

This tessalated geometry is the basis for the calculation of the electromagnetic field propagation in the DGTD solving the differential equations of motion using a low-storage Runge Kutta method of fourth order with 14 stages. Additionally, the fields are spatially expanded into fourth order Lagrange polynomials on the triangular elements. Via a total field - scattered field (TfSf) contour between the two glass domains in Figure 3.5 (red line) we induce the fields into the simulation domain.[136, 137] The permittivities of the different dielectric materials are approximated by Drude-Lorentz models

$$\epsilon(\omega) = \epsilon_\infty - \sum_p^D \frac{\omega_\mathrm{p}^2}{\omega(\omega + \mathrm{i}\gamma_\mathrm{p})} + \sum_p^L \frac{\Delta_\epsilon^{(p)}\omega_\mathrm{p}^2}{\omega_\mathrm{p}^2 - \omega^2 - \mathrm{i}\gamma_\mathrm{p}\omega}\,, \tag{3.16}$$

fitted to own ellipsometry or reference data. The numerous material fit parameters which were used to describe the different materials involved are presented in the tables 3.1–3.4.
The permittivity of the glass substrate is approximated with $\epsilon_\infty = 2.25$. In this setup we calculate reflectance $R(\omega)$ with the help of the incidence power spectrum

$$C_\mathrm{inc}(\omega) = \int \mathbf{S}_\mathrm{inc}(\omega) \cdot \mathrm{d}\mathbf{A}\,, \tag{3.17}$$

according to the time-averaged Poynting vector $\mathbf{S}(\omega)$, using

$$R(\omega) = \frac{1}{C_\mathrm{inc}(\omega)} \int \mathbf{S}_\mathrm{refl}(\omega) \cdot \mathrm{d}\mathbf{A} \tag{3.18}$$

by recording the reflected (scattered) fields and the according Poynting vector on the TfSf contour (cf. 3.5, red line). Analogously, we can define the transmittance

$$T(\omega) = \frac{1}{C_\mathrm{inc}(\omega)} \int \mathbf{S}_\mathrm{trans}(\omega) \cdot \mathrm{d}\mathbf{A}, \tag{3.19}$$

where the corresponding integration contour is the interface between the two layers of air (cf. Figure 3.5, blue line). In the above equations, $\mathbf{S}$ describes the Poynting vector. Specifically, $\mathbf{S}_\mathrm{inc}$ denotes the Poynting vector calculated from the incident fields alone, while $\mathbf{S}_\mathrm{refl}$ and $\mathbf{S}_\mathrm{trans}$ denote, respectively, the Poynting vectors calculated from the reflected and transmitted fields. The total absorption spectrum is then calculated by

$$A(\omega) = 1 - R(\omega) - T(\omega)\,. \tag{3.20}$$

The absorption spectra for the single layers as shown in Figure 4.13(c,d) in section 4.2.3 can be obtained, calculating the reflectance and transmittance on the corresponding layer top and bottom interfaces.

Table 3.1.: PEDOT:PSS permittivity data used in the simulation. Fit for reference data from Pettersson et al.[139]

Pole p	ϵ_∞ or $\Delta_\epsilon^{(p)}$	$\omega_p\,(10^{15}\,\mathrm{rad\,s^{-1}})$	$\gamma_p\,(10^{15}\,\mathrm{s^{-1}})$
Drude	2.050	1.949	$7.519 \cdot 10^{-1}$
Lorentz	$4.270 \cdot 10^{-1}$	9.527	$5.471 \cdot 10^{-1}$
Lorentz	$3.905 \cdot 10^{-2}$	2.442	1.259

Table 3.2.: ITO permittivity data used in the simulation. Fit for reference data from Schubert.[140]

Pole p	ϵ_∞ or $\Delta_\epsilon^{(p)}$	$\omega_p\,(10^{15}\,\mathrm{rad\,s^{-1}})$	$\gamma_p\,(10^{15}\,\mathrm{s^{-1}})$
Drude	3.461	2.588	$1.839 \cdot 10^{-1}$
Lorentz	$8.004 \cdot 10^{-1}$	7.585	$3.103 \cdot 10^{-1}$

Table 3.3.: Silver permittivity data used in the simulation. Fit for reference data from Johnson et al.[141]

Pole p	ϵ_∞ or $\Delta_\epsilon^{(p)}$	$\omega_p\,(10^{15}\,\mathrm{rad\,s^{-1}})$	$\gamma_p\,(10^{15}\,\mathrm{s^{-1}})$
	1.475	–	–
Drude	1.000	$1.389 \cdot 10^{+1}$	$4.161 \cdot 10^{-2}$

Table 3.4.: TiO_2 permittivity data used in the simulation. Fit for reference data from [142].

Pole p	ϵ_∞ or $\Delta_\epsilon^{(p)}$	$\omega_p\,(10^{15}\,\mathrm{rad\,s^{-1}})$	$\gamma_p\,(10^{15}\,\mathrm{s^{-1}})$
	3.323	–	–
Lorentz	3.181	6.200	$1.976 \cdot 10^{-1}$

Table 3.5.: P3HT:PCBM permittivity data used in the simulation. Fit for measured data, cf. Figure 3.6 and section 3.1

Pole p	ϵ_∞ or $\Delta_\epsilon^{(p)}$	$\omega_p\,(10^{15}\,\mathrm{rad\,s^{-1}})$	$\gamma_p\,(10^{15}\,\mathrm{s^{-1}})$
	1.475	–	–
Lorentz	$9.695 \cdot 10^{-2}$	3.673	$4.023 \cdot 10^{-1}$
Lorentz	$8.626 \cdot 10^{-2}$	3.984	$6.760 \cdot 10^{-1}$
Lorentz	$1.821 \cdot 10^{-2}$	3.160	$1.373 \cdot 10^{-1}$
Lorentz	1.261	7.882	2.588
Lorentz	$6.727 \cdot 10^{-2}$	3.409	$2.863 \cdot 10^{-1}$

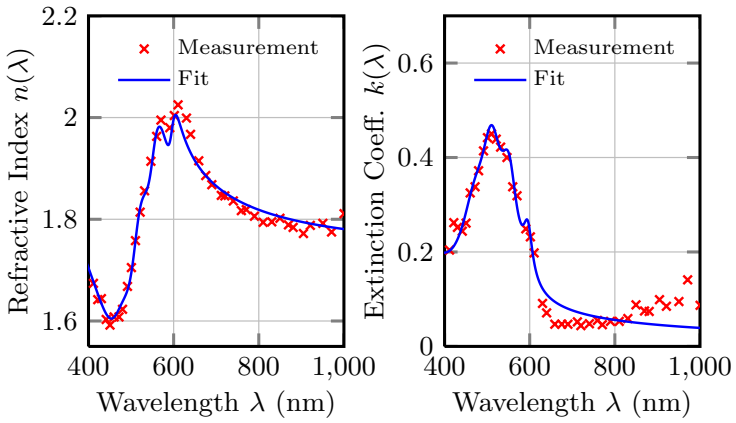

Figure 3.6.: Measured ellipsometric data and the material fit used for P3HT-PCBM to describe the solar cells presented in section 4.2.3. The refractive index data $n(\lambda)+\mathrm{i}k(\lambda) = \sqrt{\epsilon(\lambda)}$ is fitted by a Drude-Lorentz model according to equation (3.16) with the material parameters presented in table 3.5. Adapted from Pfadler et al.[133]

3.5. Nanoimprint Lithography

The following section on Nanoimprint Lithography is based on the book chapter *Controlled Nanostructures in Organic and Hybrid Solar Cells* which I have written as part of my Ph.D.[143] I wrote the section on Nanoimprint Lithography. The technique is used in section 5.1 to fabricate all-polymer solar cells with a nanoembossed comb-like donor-acceptor morphology.

Nanoimprint Lithography (NIL) is a low-cost lithographic approach from the field of nanoscience. This high-throughput method was first introduced by Chou et al. in 1995 and it greatly benefits from its simplicity.[144, 145] Unlike traditional photoresist based lithographic processes this technique only relies on direct mechanical deformation of organic materials, e.g., the active layer in organic solar cells.[146]
The general requirements to successfully realize NIL is firstly a suitable target material with controllable phase conditions and secondly a mold with a defined surface topography. Suitable materials are able to follow the surface structure of the stamps during molding and they are capable to preserve the structure after de-molding. Beside photoresist based materials which can be cured with UV light to adapt the structure by developing the resist, polymeric materials with a specific glass transition temperature fulfill the conditions as well.[146] A polymer layer can be in situ structured and thermally developed in a mechanical hotpress. During molding, the organic material is heated above its glass transition temperature. Under the influence of pressure and after a certain time, the polymer relaxes into the adjacent structure. By cooling down below the glass transition, the polymer crystalizes, a stiff network is thermally developed. Finally, sample and mold can be separated. Solvent Assisted Nanoimprint lithography (SANIL) is an alternative approach to patter an organic layer. This method can be

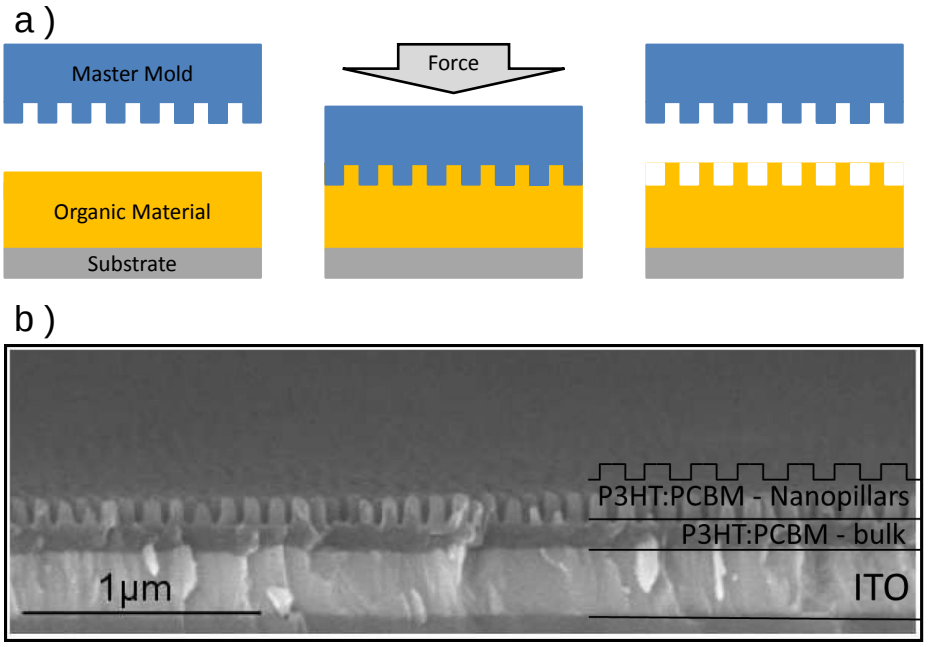

Figure 3.7.: Basic working principle of NIL. a) An organic layer is deposited on a substrate and subsequently imprinted with a mold. After separation, the reverse master structure is transferred to the organic layer. **b)** SEM cross-section of a nanostructured OPV material. The active layer is deposited on an ITO coated glass substrate. An Anodized Aluminum Oxide (AAO) honeycomb membrane is used as imprint stamp. Adapted from Dorman and Pfadler et al.[143]

realized at room temperature without thermally influencing the phase of the material since the organic layer is softened due to the exposure to a solvent-vapor saturated environment. He et al. used this technique in a double imprinting process, which enabled the preparation of nanostructured bilayer interfaces.[147]
Master molds with ordered surface features up to nano-scale sizes are either lithographically realized in a top down process or grown in a self-organized bottom up process. Highly periodic structures on Si can be manufactured via optical interference lithography. A large area interference pattern is transferred on a resist. Electron beam lithography for instance can be used to structure a resist on a smaller area, but with periods beyond the optical diffraction limit.[148] As schematically shown in Figure 3.8, both resist based lithographic approaches are followed by the deposition of a hard masking layer, e.g., a metal and a selective lift-off. Finally, the unmasked region is selectively removed by anisotropic RIE etching. Hexagonally ordered AAO molds can be produced in an electrochemically driven self-organized bottom up process. Lee et al.[150] discussed different self-ordering regimes and the effect of processing conditions on structure parameters like interpore distance D_{int} or pore diameter D_p (Figure 3.9). The high surface area of imprinting molds lead to strong adhesion of the polymer layer to the mold. The most widely used solution to this problem is to incorporate an anti-

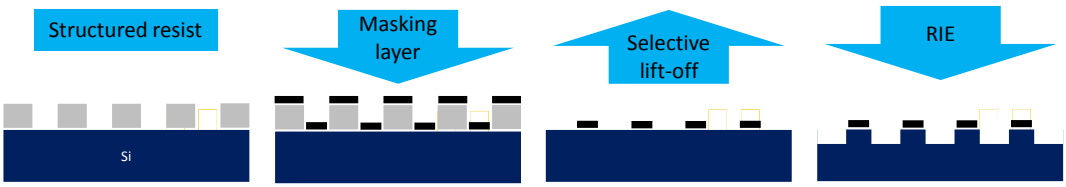

Figure 3.8.: Schematic illustration of a Si mold fabrication process. A lithographically structured resist is covered with a hard masking layer. The mask on top of the resist is selectively removed and the unprotected Si surface is etched in a reactive ion etching process (RIE). Following Jansen et al.[149]

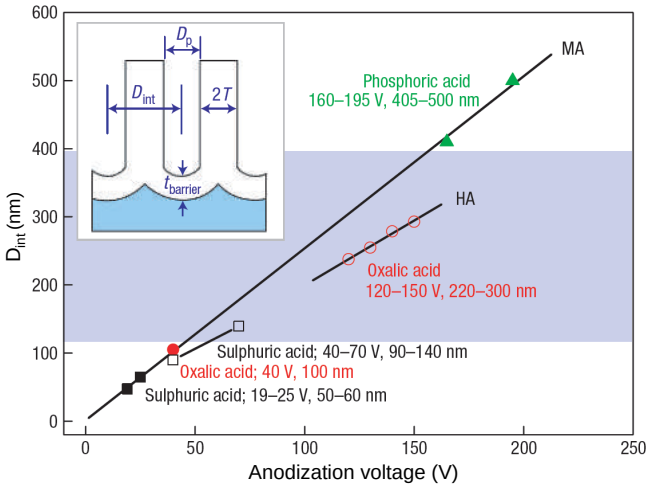

Figure 3.9.: Summary of self-ordering voltages and corresponding interpore distance (D_{int}) of different nanoporous anodic aluminum oxide (AAO) structures. The inset shows a schematic cross-section of the porous aluminum oxide structure; D_{int} = interpore distance, D_p = pore diameter, T = thickness of the pore wall, $t_{barrier}$ = thickness of the barrier layer. Based on Lee et al.[150]

adhesion layer on top of the mold to decrease its surface energy.[151] The standard approach is to fluorinate the surface by vapor deposition of fluorinated silane chains, e.g., tridecafluoro-(1,1,2,2)-tetrahydrooctyl-trichlorosilane (F13-TCS). The method can be applied to Si, SiO_2, Al_2O_3 or in general to oxide surfaces since the bounding to the surface only requires terminal hydroxyl groups.[152]

3.6. Photo-Crosslinking for Phase Separated Polymeric Networks

The following section on photo-crosslinking is based on the book chapter *Controlled Nanostructures in Organic and Hybrid Solar Cells* which I have written as part of my Ph.D.[143]. I wrote the section on photo-crosslinking. The photo-crosslinking procedure is used in section 5.1 to fabricate solution processed comb-like all-polymer solar cells. The nanoembossed polymeric bottom layer (n-type) and its artificially structured (nanoimprinted) topography is photo-crosslinked and therefore preserved when the second polymeric layer (p-type) is spincoated on top. The photo-crosslinking was realized with help of the profound knowledge of *Dr. Rui-Qi Png* in the group of *Prof. Peter Ho* at the *National University of Singapore*. The material was synthesized in the group of *Prof. L.L. Chua* at the *National University of Singapore*.

The basic working mechanism of excitonic solar cells along with a discussion of advantages and disadvantages of different morphological concepts in OPVs - the strictly phase separated donor-acceptor bilayer or flat heterojunction and the spontaneously phase separated BHJ devices for instance are introduced in section 2.1. It is shown that the BHJ concept greatly benefits from the increased interfacial area since the probability for exciton harvesting i.e., exciton diffusion towards the donor-acceptor interface and the subsequent exciton dissociation is proportional to the overall amount of donor-acceptor interfaces within the bulk of the active material. Comparing the flat and the bulk heterojunction concept in terms of overall efficiency the BHJ wins in most of the cases since the advantages of the concept are outweighing the disadvantages.
Nanostructured bilayer solar cells with an ordered and controlled interfacial donor-acceptor area can serve as a model system for a conceptual proof of principle. Such systems allow the investigation of fundamental processes influencing the macroscopic overall device efficiency. A study on controlled enhancement of interfacial area in nanostructured bilayer devices is presented in section 5.1. The external quantum efficiency of excitonic solar cells crucially depends on morphological aspects. A bi-continuous network of donor and acceptor materials that ensures path continuity to the respective electrodes is determining the charge carrier collection efficiency η(CC) (Figure 2.2 and equation 2.2). The total interfacial area of donor and acceptor materials at a fixed volume determines the exciton diffusion-dissociation product $\eta(\mathrm{ED}) \cdot \eta(\mathrm{EDIS})$ (Figure 2.2 and equation 2.2). Png and co-workers demonstrated a photo-crosslinking methodology based on sterically hindered bis(fluorophenyl azide)s (sFPAs) to realize two approaches of phase separated donor/acceptor networks under controlled conditions. On the one hand a back-infiltrated bi-continuous heterostructure network and on the other hand a so called contiguous interpenetrating heterostructure.[33] Both concepts are based on the usage of sFPA, an FPA ring with a steric substitution of an isopropyl group which can be generally mixed into polymer semiconductor solutions.

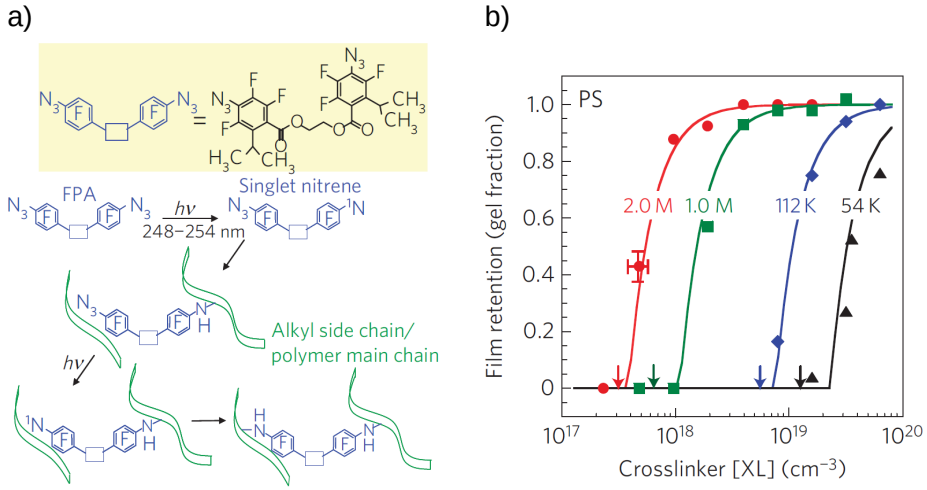

Figure 3.10.: sFPA photo-crosslinking. a) Schematic of the desired sFPA photo-crosslinking. **b)** Gel curves for monodispersed PS standards with sFPA as crosslinker. Based on Png et al.[33]

The photo-crosslinking of polymer chains is activated when exposed to deep-ultraviolet light (DUV). It is shown that a moderate concentration of sFPA in polymer OSC materials negligibly influences the device performance in OPVs. The photolysis (DUV, 254 nm) of azides generates singlet nitrenes whose predominant reaction is the desired singlet nitrene insertion into alkyl CH bonds (cf. Figure 3.10a). The photo-crosslinking efficiency is experimentally evaluated by plotting the film retention (optical density before and after exposure to DUV and subsequent solvent washing) against crosslinker concentration (cf. Figure 3.10b). The controlled back-infiltrated heterostructure is prepared for instance by infiltrating an acceptor material into a photo-crosslinked donor matrix. Islands of trapped donor as well as acceptor phases (that can occur in BHJ devices) can be excluded since this approach intrinsically features a controlled built-in continuity of donor and acceptor phases, respectively. A wide range of acceptor materials beside the typical n-type organic PCBM can be easily studied since the back-infiltrated morphology is not dictated by the natural tendency of phase separation and intermixing of donor and acceptor materials. Direct percolation pathways to the electrodes that determine $\eta_{\text{charge collection}}$ (equation 2.2) are given in all cases. The so called contiguous interpenetrating heterostructure differs from the back-infiltrated concept in an additional preparation step. A sacrificial phase-directing agent (PDA) is additionally blended into the donor layer in order to be selectively removed before the photo-crosslinker is activated and the acceptor is deposited (Figure 3.11). Higher aspect ratio donor structures are built by subsequently repeating the procedure before the deposition of the molecular donor material. Due to the phase separation with a PDA either a columnar or a more or less poriferous (sponge-like) acceptor matrix is produced.

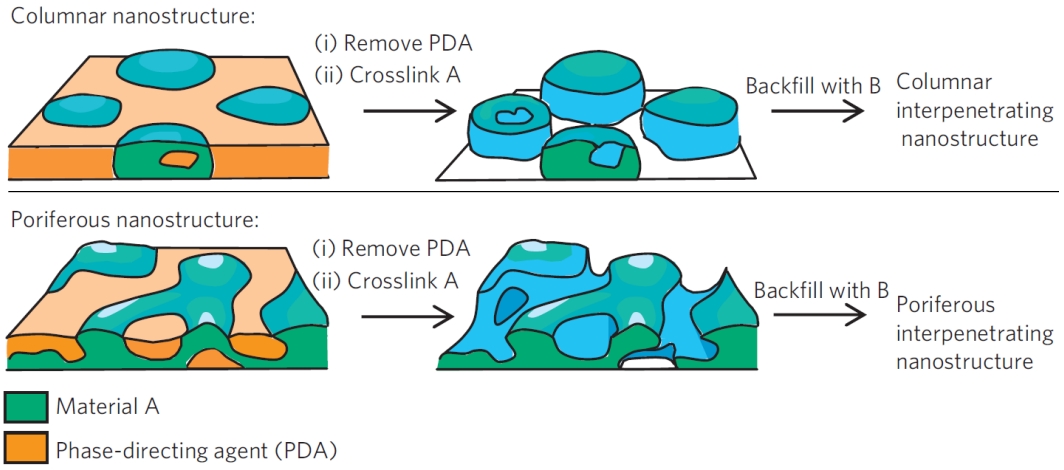

Figure 3.11.: Phaseseparation with a phase-directing agent (PDA) gives either a columnar or poriferous nanostructure of material A. Material B is deposited on top to give the controlled interpenetrating heterostructure. Based on Png et al.[33]

4. Absorption Enhancement

The interaction of semiconductors with electromagnetic radiation is introduced in section 2.2. Important quantum processes involved in the power generation of an organic solar cell upon illumination are discussed in the introductory section 2 on working principles of excitonic solar cells. Spectrally-resolved absorption profiles of thin-film solar cells are recorded by either measuring the total reflection at the backport of an integrating sphere or inside the integrating sphere (cf. section 3.1). Controlled manipulations of the overall device absorption of thin-film solar cells featuring either a 1D or 2D photonic structure are investigated in the following sections.

4.1. Energy Harvesting in 1D Photonic Multilayer Solar Cells

The following section is based on the research paper *Decoupling Optical and Electronic Optimization of Organic Solar Cells using High-Performance Temperature-Stable $TiO_2/Ag/TiO_2$ Electrodes* which was written as part of my Ph.D.[153] All experiments and measurements for this study were performed by *Dr. Kwang-Dea Kim*. I designed the project, helped with simulations and interpretation of the data and wrote most parts of the manuscript.

4.1.1. Device preparation

ITO-free electrode fabrication. The $TiO_2/Ag/TiO_2$ (TAT) multilayer was sequentially deposited onto glass substrate (PGO) by dc sputtering of a TiO_2 target (99.99 % purity) and Ag target (99.99 % purity) at room temperature in a high vacuum system with a base pressure of $3 \cdot 10^{-7}$ Torr. TiO_2 and Ag were deposited using dc power of 100 W. The thicknesses of the TiO_2 layer and Ag were calibrated using spectroscopic ellipsometry and atomic force microscopy (section 3.1), respectively.

OPV device fabrication: To fabricate the inverted OPV devices, layers of a donor-acceptor blend, PEDOT:PSS, and Ag top-electrode were sequentially deposited onto TiO_2-coated ITO glass and TAT-coated glass ($14 \times 14\,mm^2$) which were annealed at 400°C for 30 min under vacuum condition ($5 \cdot 10^{-3}$ Torr). For the preparation of the active layer, PTB7 (1-Material) and $PC_{71}BM$ (Solenne) (8:12 mg) were dissolved in chlorobenzene/1,8-diiodooxtane (CB/DIO; 0.97/0.03 ml, Aldrich). Both donor and acceptor materials are used without further purification. The solution was stirred at 45°C

overnight. The active layer was deposited onto the TiO_2-coated ITO glass (Lumtec) and TiO_2/Ag/TiO_2 coated glass substrate using spin-coating at 1000 rpm for 40 s under N_2 atmosphere. For the preparation of the PEDOT:PSS (Clevios P VP AI 4083, Heraeus) solution, PEDOT:PSS and IPA were mixed in a ratio of 1:10. This solution was spin-coated onto the active layer at 5000 rpm for 60 s under N_2 condition. The 150 nm Ag top electrode was thermally evaporated onto the PEDOT:PSS layer at an evaporation rate of 1 Å s^{-1} at a pressure of $5 \cdot 10^{-6}$ Torr.

4.1.2. Decoupling Optical and Electronic Optimization of Organic Solar Cells using High-Performance Temperature-Stable TiO_2/Ag/TiO_2 Electrodes

Organic photovoltaic (OPV) devices have attracted much interest during the last two decades, due to the possibility of low-cost fabrication, lightweight, flexibility, and simple fabrication processing.[23, 154–156] Power conversion efficiencies up to 10 % have been reported recently,[157, 158] even though this is still inferior to the theoretically predicted 20 % efficiency for organic single junction devices.[159] OPVs are classified within the distinct class of excitonic solar cells, i.e., coulombically bound electron-hole pairs are generated upon light-absorption with binding energies exceeding the thermal energy (k_BT) at room temperature. The electrochemical driving-force given at a type II staggered heterointerface is necessary for free charge-carrier generation.[20] Therefore, only excitons generated within the exciton diffusion length (typically around 10 nm) towards a donor-acceptor interface are successfully harvested. Internal quantum efficiencies (IQEs) up to 100 % have been reported.[35] In case of the IQE being unity every absorbed photon, i.e., generated exciton is separated and all photogenerated polarons are extracted from the active layer and collected at the external electrodes of the device.[18, 35, 160–162] Electronically optimized organic thin films with suitable donor-acceptor macro phase separation exhibiting such high IQE can only be realized using film thicknesses around 100 nm, which results in severe performance losses due to limited light absorption.[67, 160] In contrast, thicker layers exhibiting virtually complete photon harvesting, but suffer from reduced IQEs owing to pronounced charge carrier recombination losses. This trade-off motivates researcher to introduce light management structures into the photocurrent generating layers that either localize the electro-magnetic energy in the near-field of plasmonic nanostructures or increase the optical path length due to scattering into lateral modes.[163, 164] One requirement for their successful implementation is that the structural changes due to the light management structures do not influence the electronic properties of the organic layer, which is crucial especially for spontaneously intermixed BHJ devices. Therefore, it is necessary to introduce a simple and suitable device design ideally featuring flat interfaces in order to allow for decoupling of optical and electronic optimization. Here, we focus on the tuneability of the coherent electro-magnetic field distribution in flat interface OPVs that naturally define an optical cavity (Figure 4.1a). The tuneability of the cavity is accessible by replacing the commonly used ITO with a TiO_2/Ag/TiO_2 (TAT) sandwich structure and a variation of the respective layer thicknesses. In particular, variation

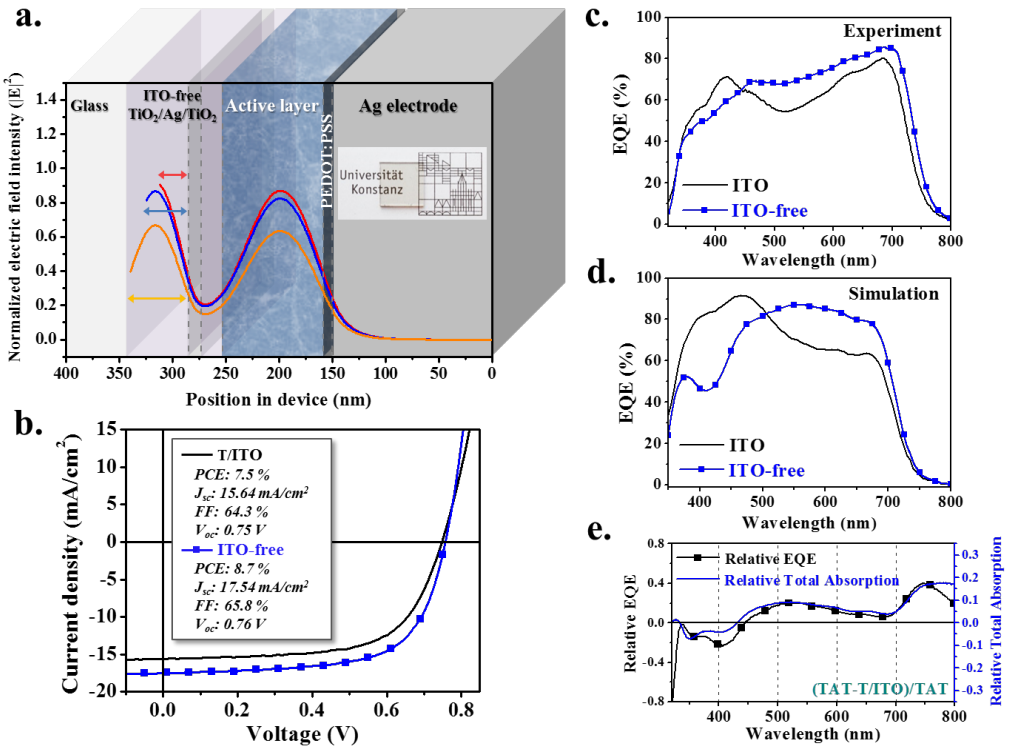

Figure 4.1.: Schematic device structure and characterization of device performance and optical properties. (a) Schematic view of the fabricated photovoltaic cells, picture of TiO_2/Ag/TiO_2 (TAT): 20/12/28 nm (ITO-free) electrode, and simulation of optical electric field profiles in terms of the normalized intensity ($|E|^2$) depending on the bottom TiO_2 thickness (28 nm; red, 40 nm; blue and 55 nm; yellow); here, the wavelength of 550 nm was chosen. **(b)** Current-voltage (J-V) characteristics of OPVs with T/ITO and TAT (ITO-free) electrodes. **(c)** Experimentally measured and **(d)** simulated EQE spectra of devices with T/ITO and TAT (ITO-free) electrodes. **(e)** Relative EQE and absorption of (TAT-T/ITO)/TAT. Reprinted with permission from Kim and Pfadler et al.[153] Copyright (2015), AIP Publishing LLC.

of the thickness of the bottom TiO_2 layer does not influence the electronic properties of the electrode since the charge collecting second TiO_2 layer, which is in contact with the organic active layer, remains unchanged. In general, high transparency of the transparent conducting electrode (TCE) is of great importance for the effective light absorption in the device, which is finalized by an Ag/Al backelectrode (backmirror).[165–167] ITO has been commonly used for various optoelectronic devices as transparent electrode due to its excellent transparency and electrical properties. However, the price of ITO is rising due to the limited availability of indium.[168, 169] Besides, ITO deposition requires high-temperature vacuum processing and ITO has a low thermal stability caused by ion diffusion at temperatures exceeding 300°C.[170] The thickness of the ITO layer determines its properties (electronic and optical transmission). ITO thin films have a fixed thickness of around 200 nm for optimum performance for solar

cell applications. These drawbacks of ITO are the driving force for researchers to investigate alternative materials - a number of promising candidates have been already identified. One class are doped metal oxides such as Al- and Ga-doped ZnO (AZO and GZO), which are cheaper than ITO.[167] Additionally, the use of conducting carbon materials including carbon nanotubes, graphene, and conducting polymers such as poly(3,4-ethylenedioxythiophene):poly-(styrenesulfonate) (PEDOT:PSS) has been proposed, which allows solution-processing of the transparent electrode.[171, 172] However, most alternative materials are inadequate as replacement for ITO due to their lower optical transparency and/or conductivity in comparison to ITO. Recently, oxide/metal/oxide (OMO) multilayer structures featuring very thin metal layers (Ag, Au, or Cu) sandwiched between two metal oxides (TiO_2, ZnO, or MoO_3) have been demonstrated as TCEs.[166, 173–175] Sandwich structures based on TiO_2 are promising candidates due to their transparency in the visible, and the strong mechanical and chemical stability of TiO_2.[176] Dhar et al. demonstrated TAT multilayer electrodes with good optoelectronic properties exhibiting a sheet resistance (R_{sheet}) of 5.7 Ω $\square^{-1}$ and an average optical transmittance of 90 % at 590 nm.[173] However, these structures have not been successfully applied to thin-film devices like OPVs, dye-sensitized solar cells (DSSC), or the recently emerging perovskite solar cells.
In this section we demonstrate high-performance state of the art OPVs using TAT multilayers as an ITO-free electrode which allows for single junction efficiencies up to 8.7 %. The possibility to individually control the film thicknesses in the multilayer allows for an optimization of the light intensity profile in the active layer as a function of the photoactive material, which directly translates into higher photocurrents and more efficient devices.

Results and Discussion. ITO-free transparent electrodes with a TAT multilayer structure on glass were prepared by sputtering at room temperature without any vacuum break (see Figure 4.1a). To fabricate these OPVs, the ITO-free electrode consisting of the top TiO_2 layer as an electron collector was annealed at 400°C for 30 min. This thermal processing is crucial for charge collection, directly evident from current density-voltage curves, mostly reflected in improved fill factors. Interestingly, the R_{sheet} of TAT electrodes is stable after annealing even at elevated temperatures up to 550°C with slight increase in R_{sheet} value of only 1.69 Ω $\square^{-1}$ (from 6.75 to 8.44 Ω $\square^{-1}$), whereas the R_{sheet} of TiO_2-coated ITO (T/ITO) annealed at the same condition was significantly increased from 11.23 to 21.65 Ω $\square^{-1}$ (Figure 4.2). This indicates that the TAT electrodes have a high thermal stability and maintain their good electrical properties. In contrast, upon the same thermal treatments ITO electrodes show significantly deteriorating performance. Owing to this low thermal stability, ITO has been narrowly used only for the application of electric devices fabricated at temperatures below 300°C.[170] The advantage of better thermal stability of our TAT electrodes provides a wide opportunity in this field and makes them viable for a number of devices based on TiO_2 electrodes like DSSCs, perovskite photovoltaics, and other hybrid inorganic-organic solar cells. Besides the superior thermal stability of TAT electrodes in comparison to ITO electrodes they have the advantage that the absorption behaviour,

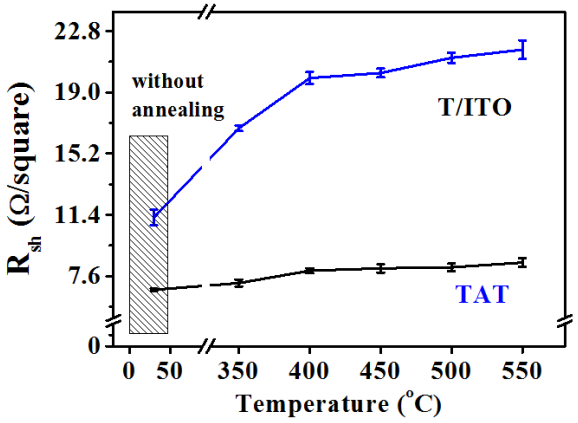

Figure 4.2.: Thermal stability test of T/ITO and TAT electrodes. Sheet resistance (R_{sh}) of T/ITO and TAT (20/12/28 nm) electrodes depending on different annealing temperature at 350, 400, 450, 500 and 550°C for 30 min under vacuum condition of $3 \cdot 10^{-3}$ Torr. Reprinted with permission from Kim and Pfadler et al.[153] Copyright (2015), AIP Publishing LLC.

i.e., the coherent electric field intensity ($|E|^2$) distribution inside the active layer of the device can be maximized by varying the thickness of the TiO_2 layers without the danger of structure-induced changes to the active layer morphology. Therefore, matching the optical cavity for an optimized active material processing parameter like the active layer thickness results in a maximized device performance due to enhanced light harvesting, while keeping the electronic properties of the organic layer completely unaffected. The computational results in Figure 4.1a show the coherent electric field profiles inside OPV devices as a function of the bottom-TiO_2 layer thickness. Optical simulations based on a transfer matrix algorithm (section 3.2) show that changes in thickness of the individual layers crucially influences the appearance of the optical cavity mode.[124] Figure 4.1b shows the current density-voltage (J-V) characteristics of poly[[4,8-bis[(2-ethylhexyl)oxy]benzo[1,2-b:4,5-b']dithiophene-2,6-diyl][3-fluoro-2-[(2-ethylhexyl)carbonyl] thieno[3,4-b]thiophenediyl]] (PTB7): [6,6]-phenyl C71-butyric acid methyl ester ($PC_{71}BM$) OPVs fabricated with two different electrodes, namely T/ITO and TAT multilayer. Using the TAT: 20/12/28 nm multilayer, a representative power conversion efficiency (PCE) of 8.7 % (fill factor, FF of 65.8 % and open circuit voltage, V_{OC} of 0.76 V) is reached with a significantly higher short-circuit current density (J_{SC}) of 17.54 mA cm^{-2}. This is a relative enhancement of 12 % in J_{SC} ([J_{SC},TAT-J_{SC},T/ITO]/J_{SC},T/ITO) with slightly increased FF and V_{OC} in comparison to a representative ITO-based device with a J_{SC} of 15.64 mA cm^{-2} (7.5 % overall efficiency, FF of 64.3 % and V_{OC} of 0.75 V). In order to determine the origin of the superior performance, experimental external quantum efficiencies (EQEs) for two different OPVs featuring T/ITO and TAT multilayer electrodes are compared. As shown in Figure 4.1c the EQE in the wavelength range of 450-800 nm (i.e., the main absorption of the PTB7:$PC_{71}BM$ blend) with the TAT electrode is higher than with ITO, while there is a slight reduction

in the EQE observed between 350 and 450 nm. These findings are in good agreement with simulated EQE spectra as evident from Figure 4.1d. To verify the decoupling of the optical absorption and the IQE in the measured EQE data, relative EQE and relative total absorption calculated as (TAT-T/ITO)/TAT are compared (Figure 4.1e). Good agreement between relative EQE and relative total absorption was obtained, indicating that the IQE of the active film remains unchanged and the improvement in EQE can be directly attributed to the increase in light absorption. Figure 4.3 shows the

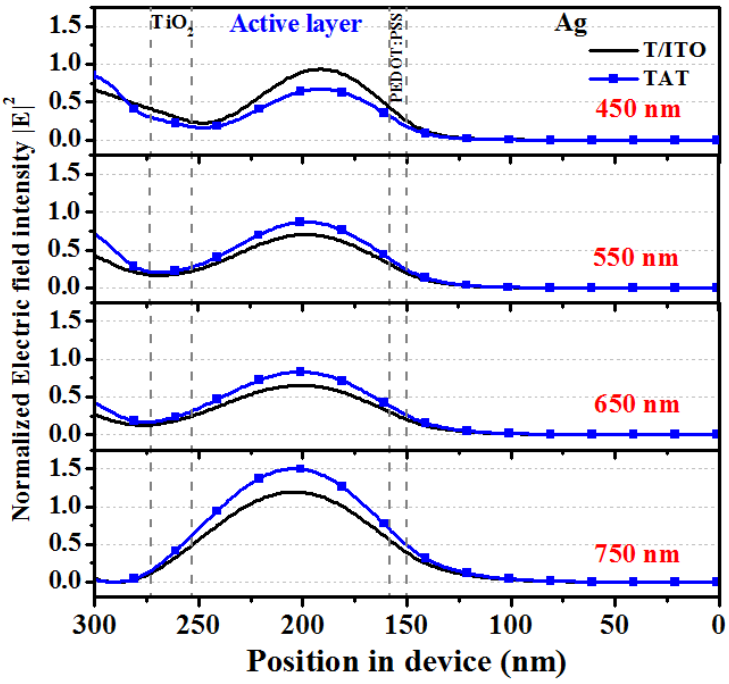

Figure 4.3.: Electric field profile inside the OPV system. Simulated result of the optical electric field profile for OPVs structured as Ag (150 nm)/PEDOT (8 nm)/PTB7-$PC_{71}BM$ (95 nm) on TiO_2 (20 nm)/ITO (170 nm) and TiO_2 (20 nm)/Ag (12 nm)/TiO_2 (28 nm) shown in Figure 4.1b depending on the wavelength of incident light (450, 550, 650 and 750 nm). Reprinted with permission from Kim and Pfadler et al.[153] Copyright (2015), AIP Publishing LLC.

simulated optical electric field profiles in the TAT and T/ITO devices from Figure 4.1b as a function of the wavelength of incident light ranging from 450 nm to 750 nm. The full optical electric field profiles ranging from 450-850 nm are presented in Figure 4.4. The simulations show that a higher intensity (i.e., $|E|^2$) for wavelengths above 450 nm can be obtained in OPVs with TAT electrode in comparison to the T/ITO reference. Accordingly, light absorption is enhanced in this wavelength region, resulting in an improvement of device performance due to enhanced photocurrent generation. While

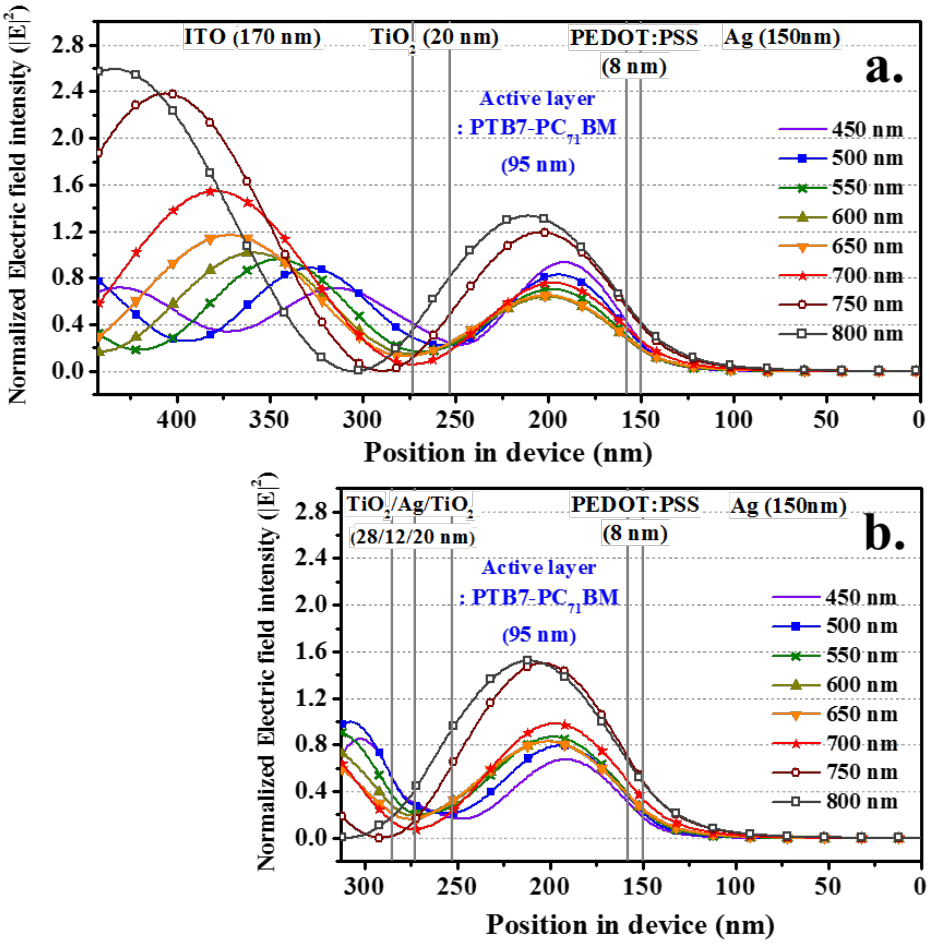

Figure 4.4.: Optical electric field profile inside the OPV system. Simulated result of the optical electrical field profile for OPVs structured as Ag (150 nm)/PEDOT (8 nm)/PTB7-$PC_{71}BM$ (95 nm) on **(a)** TiO_2 (20 nm)/ITO (170 nm) and **(b)** TiO_2 (20 nm)/Ag (12 nm)/TiO_2 (28 nm) shown in Figure 4.1b depending on the wavelength of incident light (450-800 nm). Reprinted with permission from Kim and Pfadler et al.[153] Copyright (2015), AIP Publishing LLC.

these are the representative results for one defined set of layer thicknesses of the TAT electrode, the optical electric field can be greatly influenced by the thickness of each layer in the sandwich electrode. This allows adjusting the TAT electrode to arbitrary active layers with different optimized film thicknesses and/or intrinsic optical properties. In other words, the presented TAT electrodes allow the tailored optimization of OPVs through the control of thickness of the TiO_2 layers in the TAT multilayer system. There, the optimum condition for the TAT electrode can be predicted using optical modelling of the respective photoactive film. In order to outline this methodology Figure 4.5 summarizes J_{SC} simulations for OPVs structured as Ag (150 nm)/PEDOT (8 nm)/active layer on TiO_2/ITO or TiO_2/Ag/TiO_2 with dependencies of the layer

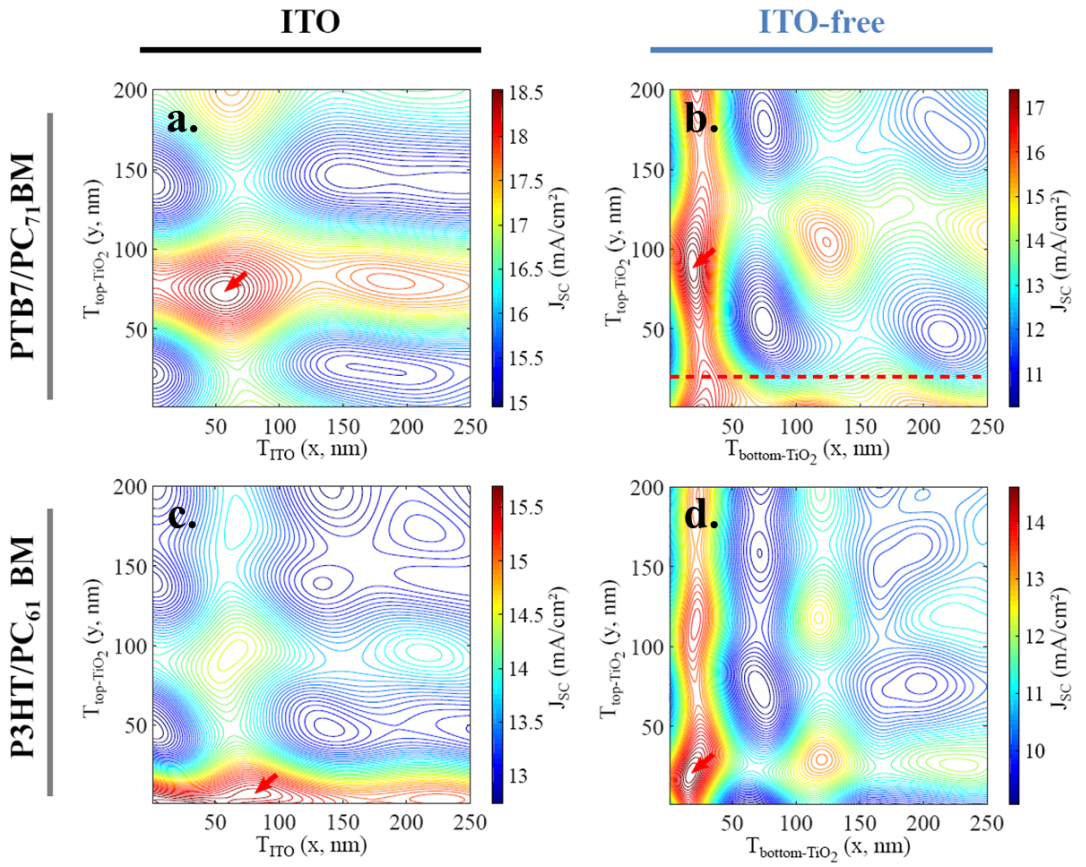

Figure 4.5.: Photocurrent simulation. Contour plot of simulated photocurrent of OPV structured as Ag (150 nm)/PEDOT (8 nm)/active layer on TiO_2/ITO (170 nm) and TiO_2/Ag (12 nm)/TiO_2 with change in the thickness of **(a)** and **(c)** ITO (x)-TiO_2 (y) and **(b)** and **(d)** bottom (x) top (y) TiO_2, respectively. The simulation of two different active layer system which are **(a)** and **(b)** PTB7:$PC_{71}BM$ (95 nm) and **(c)** and **(d)** P3HT:$PC_{61}BM$ (300 nm) was obtained. The thickness of Ag was fixed to 12 nm in this simulation. Reprinted with permission from Kim and Pfadler et al.[153] Copyright (2015), AIP Publishing LLC.

thickness of ITO (x) vs TiO_2 (y) and bottom (x) vs top (y) of TiO_2, respectively. The contour plots of J_{SC} for OPVs with active layers of 95 nm of PTB7:$PC_{71}BM$ (Figure 4.5a and b) and 300 nm of P3HT:$PC_{61}BM$ (Figure 4.5a and b), representing two different examples of electronically optimized OPV active layers, show a pronounced current density-dependency on the layer thicknesses. This result implies that the optimum condition for high-performance can be effectively discovered by controlling the thickness of each layer in the simulation for different types of photovoltaic devices with different absorption spectra of the photoactive materials and different active layer thicknesses. The highest J_{SC} value in each condition is indicated by a red arrow. In the OPV device with PTB7:$PC_{71}BM$ on ITO (Figure 4.5a), the maximum J_{SC} value of 18.5 mA cm^{-2} is observed at the thickness condition of TITO = 60 nm and $TTiO_2$ = 70 nm. In

contrast, the OPV with exactly the same active layer but on a TAT electrode shows a highest J_{SC} value of 17.5 mA cm^{-2} ($T_{bottom\text{-}TiO_2}$ = 20 nm, 12 nm Ag and $T_{top\text{-}TiO_2}$ = 90 nm). While these results indicate slightly higher possible photocurrents in the ITO system it should be noted that the fabrication of high-performance devices using such thicknesses is challenging because not only optical but also electrical properties of the multilayer devices should be considered. In the case of ITO, the resistance is exponentially increased as the film thickness is decreased. For instance, high sheet resistances ($> R_{sheet} = 50\ \Omega\ \square^{-1}$) have been reported for thicknesses below 100 nm, which would directly result in reduced FFs.[177] Hence, the optimum condition from optical simulations would not allow for achieving a high-performance device in case of the ITO electrode. In contrast, the conductivity of the TAT electrode is mostly provided by the thin Ag film, and the sheet resistance is only marginally influenced by the thickness of the top and bottom-TiO_2 film (Figure 4.4). Furthermore, the simulations

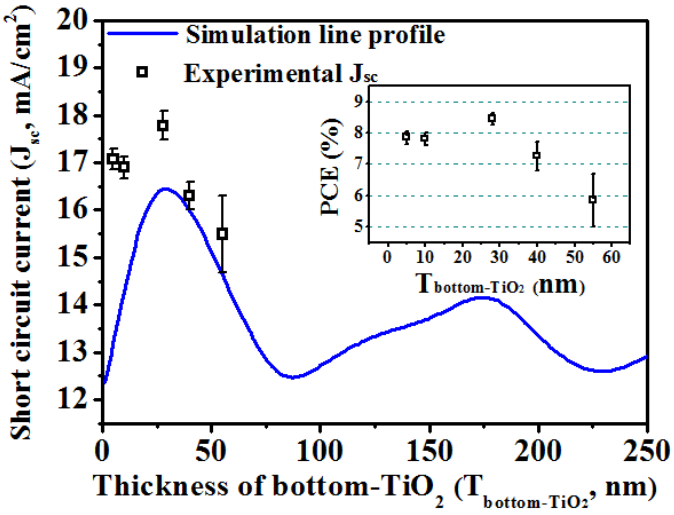

Figure 4.6.: Simulated and experimental J_{SC} with PCE of device. Simulated J_{SC} profile of TAT multilayer with fixed Ag/top-TiO_2 layer thickness of 12/20 nm (blue line) and experimental J_{SC} (open square) with changing in the thickness of bottom-TiO_2 layer (5, 10, 28, 40 and 55 nm). Inset: Power conversion efficiency (PCE). The dotted line in Figure 4.5b represents this simulation result. Reprinted with permission from Kim and Pfadler et al.[153] Copyright (2015), AIP Publishing LLC.

underline how important it is to optimize the active layer thickness to gain a maximum photocurrent generation in different active layer systems as shown for the two examples of PTB7- and P3HT-based OPVs. While commercial ITO substrates are typically fabricated at a fixed layer thickness at which balanced sheet resistance and transitivity are obtained, the TAT electrodes allow to individually adjust the layer thicknesses in order to maximize light absorption in the active layer. As a proof of concept, the decoupled optical cavity optimization of devices equipped with the TAT multilayer electrodes is exemplarily performed, both by experiment and simulation. For this purpose only the bottom TiO_2 layer is varied in order to keep the thickness of the top layer comparable

for the ITO and the TAT film. As found in optimization experiments the thickness of the top TiO_2 layer influences the electronic properties of the device, mostly due to an increased series resistance and film roughness for thicker layers. While this issue requires further optimization of the TiO_2 processing in the future in order to enable even wider tunability, the fundamental principle presented in this study is outlined for the exclusive variation of the bottom TiO_2 layer. The resulting experimentally obtained J_{SC} values are compared to the simulated values (Figure 4.6). $T_{bottom\text{-}TiO_2}$ thicknesses of 5 and 10 nm resulted in J_{SC} values of 17.08 ± 0.22 and 16.89 ± 0.23 mA cm^{-2}, respectively. The highest J_{SC} value was 17.78 ± 0.31 mA cm^{-2} for $T_{bottom\text{-}TiO_2}$ of 28 nm, in good agreement with the simulated curves. By increasing $T_{bottom\text{-}TiO_2}$ from 40 to 55 nm, the J_{SC} values were gradually decreased from 16.30 ± 0.28 to 15.49 ± 0.80 mA cm^{-2}. Detailed information for the device performance is presented in Table A1. We note that the experimentally measured J_{SC} value has a similar trend as the simulated J_{SC} ($\geq T_{bottom\text{-}TiO_2}$ of 10 nm), although the J_{SC} value in experimental results was slightly higher than the values obtained from simulations. In addition, the PCE follows the J_{SC} tendency, as shown in Figure 4.6 (inset), underlining that the electronic properties of the active layer are not affected by tuning the TiO_2 bottom layer. This further implies that the change in thickness of the bottom-TiO_2 layer is exclusively responsible for the device performance as it directly determines the coherent electric field distribution in the active layer of the photovoltaic device.

Conclusion and Outlook. We have achieved high performing OPVs exhibiting state of the art efficiencies with the PTB7:$PC_{71}BM$ system using a TAT multilayer electrode as replacement for ITO. Our TAT multilayers show a superior thermal stability than T/ITO, making them viable for application in other photovoltaic systems like DSSCs and perovskite solar cells. As outlined by a combination of experiments and optical simulation it is possible to tune the electric field intensity inside the device by controlling the thickness of the TAT layer, and with this the properties of the optical cavity. Our results show that in particular the front (or bottom) TiO_2 layer can be tuned in thickness without changing the electronic properties of the TAT electrode, which allows the tailored optimization of device performance for arbitrary active layer compositions and thicknesses.

4.2. Light-coupling and Light-Trapping in Nanostructured Thin-Film Solar Cells featuring a 2D Photonic Structure

The following sections are based on the research papers *A comparison of light-coupling into high and low index nanostructured photovoltaic thin films* and *Structure-induced Resonant Tail-State Absorption in Polymer:Fullerene Bulk-Heterojunction Solar Cells* which I have both written as part of my Ph.D.[106, 133] For these studies I fabricated all solar cells and absorption samples for data shown in the publications. Direct laser

interference patterning (DLIP) was realized with the help of *M. Stärk* (cf. section 3.3) and fully vectorial electromagnetic simulations (cf. section 3.4) were performed in collaboration with *T. Kiel* and co-workers. I wrote the manuscripts and was responsible for editing.
Following the previous definition of 1D photonic structures for the description of multilayer material stacks with literally only one finite dimension in vertical direction (e.g., the thickness of the respective layer in z-direction) we define 2D photonic structures by additionally introducing a lateral periodicity in one of the horizontal directions (e.g., in x-direction). The obtained lateral periodicity and more important the vertical dimension of the periodic structures are comparable to the thicknesses of the active materials.

4.2.1. Device preparation

TiO_2 deposition: ITO substrates (PGO, 10 Ω $\square^{-1}$) were cleaned by ultrasonic bath using deionized water with dishwashing detergent, acetone and isopropanol for at least 5 min each followed by 7 min O_2 plasma cleaning (Diener Femto). Approximately 60 nm of TiO_2 was deposited via spray pyrolysis of a titanium diisopropoxy bisacetonate precursor (Sigma Aldrich) solution diluted 1:10 (vol:vol) in ethanol. Clean substrates were heated to 450°C with a ramp rate of $30°C \cdot min^{-1}$. The precursor solution was then deposited using a spray nozzle, annealed at 450°C for 15 min, and slowly cooled to room temperature over a time of approximately 2h.
Direct laser interference patterning (section 3.3) was then directly applied on approximately 60 nm thick anatase TiO_2 films. A second approximately 15 nm thick TiO_2 layer is deposited (according to the above described procedure) on the patterned as well as the flat reference devices.

Organic active material system. A layer of approximately 125 nm of the P3HT:PC_{61}BM blend (1:0.8) was spincoated (1 min/ 1000 rpm) on clean glass/ITO/ TiO_2 substrates. P3HT was purchased from Merck and PCBM from Nano-C. An electron blocking layer of 5-10 nm PEDOT:PSS is deposited on top following the procedure of Weickert et al.[178] 150 nm Ag are thermally evaporated (Theva evaporation system) as backmirror (backelectrode) on top. Devices are finally thermally annealed (10 min, 140°C) in a nitrogen filled glove box.

In-organic active material system. Approximately 50 nm thick Sb_2S_3 layer is prepared by chemical bath deposition (CBD) according to a previously reported procedure with minor adjustments.[179] In particular, solutions of $Na_2S_2O_3$ (4 g) in deionized water (25 ml) and $SbCl_3$ (650 mg) in acetone (2.5 ml) were prepared and cooled in an ice bath for 90 min. Precursors were mixed into 100 ml of likewise cooled deionized water and samples are immediately put into the mixed solution. After chemical bath deposition samples were rinsed with deionized water and promptly dried in a nitrogen stream. Subsequently, the coated backside of the samples was cleaned with hydrochloric acid, and the samples were annealed at 300°C for 35 min in a nitrogen atmosphere.

P3HT solution (Merck, 10 mg ml^{-1}, dissolved in chlorobenzene) was then spin-coated at 1500 rpm for 1 min to obtain an approximately 30 nm thick film. As backelectrode, 150 nm Ag was deposited via thermal evaporation.

4.2.2. A Comparison of Light-Coupling into High and Low Index Nanostructured Photovoltaic Thin-Films

Photoactive inorganic/organic multilayer structures consisting of functionally aligned material combinations have been extensively investigated in the context of low-cost thin-film solar cells.[180] Thin-film devices are typically optimized in terms of the internal quantum efficiency (IQE) - the probability for a photogenerated charge-carrier to be extracted. However, there is a tradeoff between high IQEs and the overall absorption, since reduced active layer thicknesses typically increase the IQE due to suppressed charge carrier recombination owing to transport limitations but simultaneously decrease the probability of light absorption. Beside the photocurrent generating active layer, electron and hole selective metal oxide electrodes are typically introduced to balance charge carrier extraction.[154] TiO_2 is a prominent material for an electron selective contact owing to its low valence band and its intrinsic n-type behavior.[181] Beside the application in photovoltaics, TiO_2 semiconductors are widely used in energy storage, catalysis, sensors and memristors.[182–185] On top of this electron selective glass/ITO/TiO_2 bottom support, either organic (e.g., polymer/fullerene blends) or inorganic/hybrid (e.g., antimony-sulfide (Sb_2S_3) or organometal perovskites) materials are deposited as photoactive layers.[186–188] Highly effective light-trapping and optimal in-coupling of incident solar irradiation are essential to boost efficiencies in thin-film devices. Design rules concerning refractive index matching to obtain efficient antireflection coatings and shape optimization of nanostructured texturing layers focusing on efficient broadband and omnidirectional light-coupling are discussed in literature both by experiment and simulation.[189–194] Periodically structured transparent top electrodes like inverted 3D pyramids for example were shown to simultaneously enhance absorption and photocurrent generation in thin-film microcrystalline or amorphous silicon.[195–197] Ideally, such structuring is realized using up scalable, low-cost, and fast synthesis strategies compatible with mass production. For instance, Lasagni et al. discussed the scalability of periodic structures fabricated via direct laser interference patterning (DLIP) at a rate of 0.1 $m^2 \cdot min^{-1}$ with sub-μm resolution.[198] Here, we apply DLIP on anatase TiO_2 (Figure 4.7) to obtain highly ordered periodic structures. In order to assess their potential these structures are implemented into common thin-film solar cell architectures that either use a blend of P3HT:$PC_{61}BM$ (poly(3-hexylthiophene): [6,6]-phenyl-C61-butyric acid methyl ester) or Sb_2S_3 as photoactive materials. Based on our findings we are able to spectroscopically show that wavelength-scale patterns support the in-coupling of light ($E \geq E_{bandgap}$) into an active material with higher refractive index n, but simultaneously suppress the in-coupling into a low n material like an organic semiconductor. Various interference patterns can be directly transferred via DLIP into the surface of different materials such as metals, semiconductors, polymers, and ceramics.[128–131] To the best of our knowledge, this is the first time this method

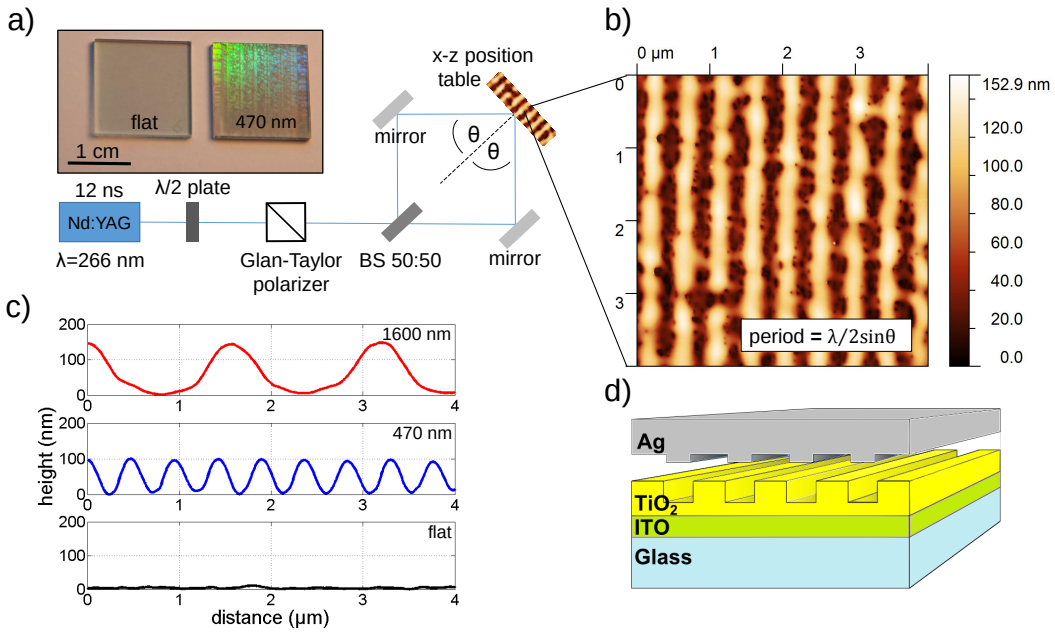

Figure 4.7.: Schematic of a two-beam direct laser interference patterning (DLIP) set-up. The periodicity (cf. equation 3.15) of the interference pattern is determined by the angle of incidence Θ. The inset of **(a)** shows a photography, which illustrates the occurrence of far-field diffraction patterns due to the wavelength-scale topography pattern of TiO_2. **(b)** AFM topographic height profile of laser structured TiO_2 featuring a periodicity of 470 nm. **(c)** Summary of the investigated structures. The shown profiles are statistically averaged over 750 AFM line scans. **(d)** Schematic drawing of a structured solar cell architecture. The gap is either filled with an organic (P3HT:$PC_{61}BM$) or an inorganic (Sb_2S_3) active material system. Reprinted with permission from Pfadler et al.[106] Copyright (2015), AIP Publishing LLC.

is applied to TiO_2. The experimental realization of a two-beam interference setup is schematically shown in Figure 4.7a. A Q-switched Nd:YAG laser produces 12 ns pulses at a repetition rate of 10 Hz and was scanned over the surface. Due to the strong absorption of TiO_2 at 266 nm, the fourth harmonic of the fundamental beam (1064 nm) is chosen to transfer the interference pattern into the TiO_2 surface. The periodicity of the interference pattern (cf. equation 3.15) is determined by the angle of incidence Θ (Figure 4.7a, b). Details on laser patterning of TiO_2 and structure formation is provided in section 3.3.

The inset of Figure 4.7a shows a photography, which illustrates the occurrence of far-field diffraction patterns due to the reflectance of visible light at the periodically patterned substrates. Corresponding height profiles of the employed patterns are summarized in Figure 4.7c. The shown profiles are statistically averaged over 750 line scans, which are extracted from atomic force microscopy (AFM) topographic height profiles such as exemplarily shown for the 470 nm period structure (Figure 4.7b). Two different photovoltaic thin-films are conformally coated on top of a flat reference and two patterned substrates featuring a 470 nm and 1600 nm pitch, respectively. Both material

systems are finalized by the thermal evaporation of a 150 nm thick Ag back reflector (Figure 4.7d). The first architecture consists of approximately 125 nm P3HT:$PC_{61}BM$ with 5-10 nm PEDOT:PSS (poly(3,4-ethylenedioxythiophene):polystyrene sulfonate) on top and serves as a model system for an inverted organic solar cell. The second architecture features approximately 50 nm Sb_2S_3 with 30 nm P3HT on top, a common combination in (extremely) thin absorber photovoltaics. Note that the photocurrent contribution of P3HT is negligible in the Sb_2S_3/P3HT system.[187] The total absorption A_{tot} of the respective solar cell architectures is determined by measuring the total reflectance R_{tot} at the backport of a 150 mm diameter integrating sphere. Accordingly, A_{tot} = 1 - R_{tot} since the transmission through the Ag back-reflector can be neglected as shown by Snaith et al.[116] The results of the spectroscopic examination are summarized in Figure 4.8. The wavelength-scale 470 nm structure shows superior total

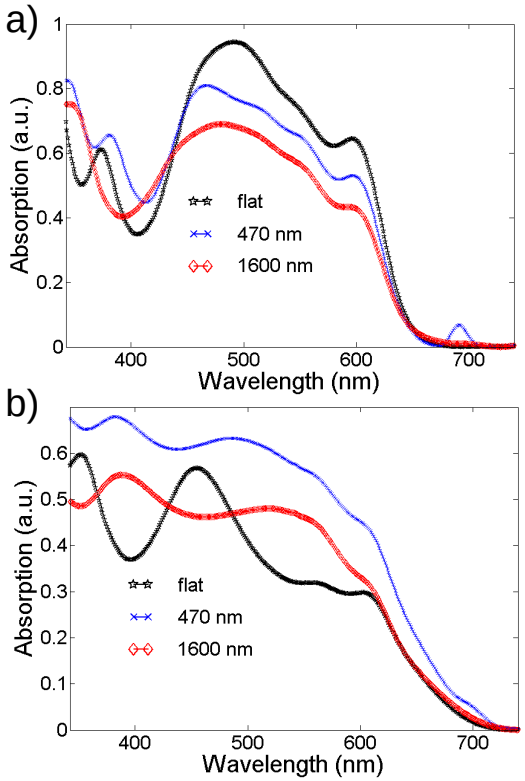

Figure 4.8.: Total absorption measurements of structured (according to Figure 4.7) thin-film solar cell systems using either P3HT:$PC_{61}BM$ **(a)** or Sb_2S_3 **(b)** as active material. The patterning is beneficial for light absorption in the Sb_2S_3 system, but detrimental for absorption in the P3HT:$PC_{61}BM$ system in the main absorption region. The total absorption is determined by measuring the total reflectance at the backport of an integrating sphere. Reprinted with permission from Pfadler et al.[106] Copyright (2015), AIP Publishing LLC.

absorption enhancement in comparison to the 1600 nm structure for both organic and inorganic active materials. Therefore, the 470 nm structure is the exemplary object of

discussion.
As apparent from direct comparison of Figures 4.8a and b there is an asymmetry in total absorption enhancement and therefore in light in-coupling into the respective active material that is caused by the patterning. In case of the organic active material, the structure induces less absorption (14 % for the 470 nm and 26 % for the 1600 nm structure) in the main absorption region of P3HT:$PC_{61}BM$ above the optical bandgap (i.e., 450 nm to 650 nm). The P3HT:$PC_{61}BM$ peak absorption (Figure 4.8a) at around 480 nm (flat) which is caused by resonant Fabry-Perot modes (Figure 3.2 and 3.3, simulated following Burkhard et al.) is suppressed due to the structuring.[124] In contrast, the total absorption of the inorganic active material greatly benefits from the structuring. There is absorption enhancement observable for all states above the optical bandgap of Sb_2S_3 (46 % for the 470 nm structure and 12 % for the 1600 nm structure in the wavelength range 400 nm to 720 nm). Even the Sb_2S_3 peak absorption (Figure 4.9) of the coherent standing wave at around 450 nm (flat) is outperformed by the structure (Figure 4.8b). We note the occurrence of resonant absorption features below the optical bandgap of P3HT:$PC_{61}BM$ at around 700 nm (Figure 4.8a), which we discuss in detail in the following section 4.2.3.
In optics, the macroscopic properties of a material are described by its dispersive refractive index $\tilde{n} = n + ik$, where n is the real part of the refractive index and k is the corresponding imaginary part, the so called extinction. Both are directly related to the intrinsic dielectric material properties.[126] The attenuation of a propagating electromagnetic wave is related to the extinction k, whereas the phase velocity within a medium and furthermore the refraction at an interface of two media is determined by the real refractive indices n_i. Reflection and transmission of light at an interface between media of differing n can be described by Fresnel equations. Therefore, one single bounce at a flat interface is considered and the angle- and polarization-dependent reflection is predicted based on a geometrical optics approach. Despite the original formulation to describe light-coupling at flat interfaces, we use Fresnel equations 4.1 to investigate the experimentally observed asymmetry in absorption enhancement, e.g., light in-coupling at the TiO_2/active material interfaces although the difference in total absorption originates from the implementation of wavelength-scale patterns in thin-film solar cell architectures. Therefore, we use spectroscopic ellipsometry to determine $\tilde{n}$ of pure Sb_2S_3, TiO_2 and P3HT:$PC_{61}BM$, respectively (Figure 4.10a and appendix Figure B1). Details on the employed ellipsometry system and the corresponding data processing are provided through the supplemental information. The inorganic Sb_2S_3 absorber shows n values around 3.5, whereas the organic P3HT:$PC_{61}BM$ absorber shows values around 1.8 for all investigated wavelength ranging from 400 nm to 880 nm (Figure 4.10a). Most important, the n values of the employed anatase TiO_2 are located between the values of Sb_2S_3 and P3HT:$PC_{61}BM$ at around 2.5. Thus, light is coupled into the active material of the solar cell architecture (Figure 4.7d) through the TiO_2, either into the high n inorganic Sb_2S_3 or into the low n organic P3HT:$PC_{61}BM$. In order to visualize the difference in light-coupling, we plot (following equations 4.1, 4.2) the dispersive Fresnel equations for unpolarized light, passing either through a flat TiO_2/P3HT:$PC_{61}BM$ interface (Figure 4.10b) or through a flat TiO_2/Sb_2S_3 interface

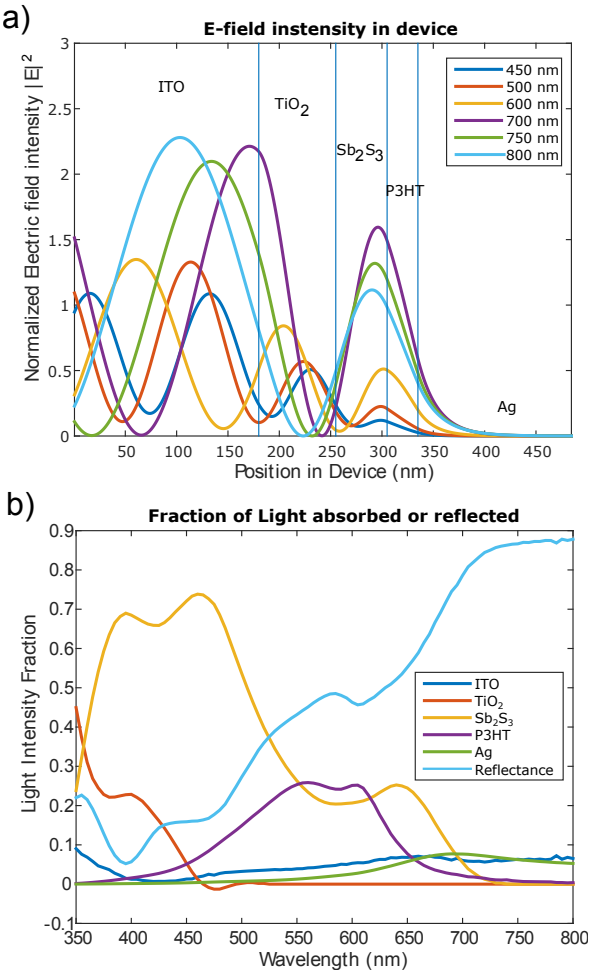

Figure 4.9.: Simulated electric field a) and absorption b) in the device configuration glass/ITO(180 nm)/TiO_2(75 nm)/Sb_2S_3(50 nm)/P3HT(30 nm)/Ag(150 nm). Reprinted with permission from Pfadler et al.[106] Copyright (2015), AIP Publishing LLC.

(Figure 4.10c) for different angle of incidence.

$$r = \frac{n_1 \cos \Theta_{\text{in}} - n_2 \cos \Theta_{\text{t}}}{n_1 \cos \Theta_{\text{in}} + n_2 \cos \Theta_{\text{t}}} \tag{4.1}$$

where r is denoted as the reflection coefficient, $n_1 = n(TiO_2)$ and n_2 is either $n(P3HT{:}PC_{61}BM)$ (Figure 4.10b) or $n(Sb_2S_3)$ (Figure 4.10c) and the angle of the incident Θ_{in} is varied between 0° and 90°. Θ_{t} is determined following Snell's law (equation 4.2)

$$\Theta_{\text{t}} = \arcsin \frac{n_1}{n_2} sin\Theta_{\text{in}} \tag{4.2}$$

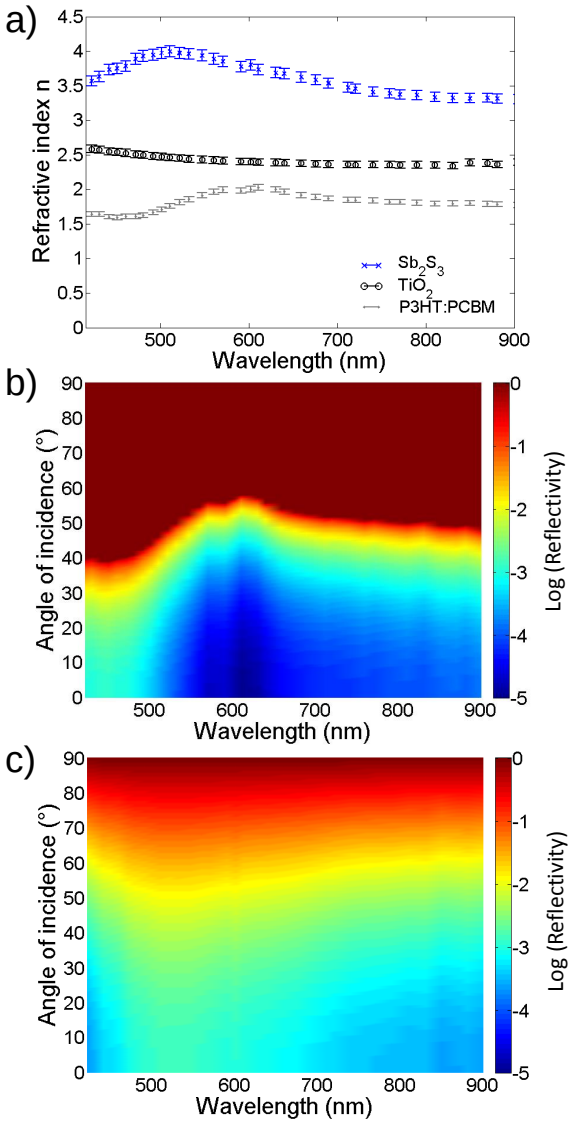

Figure 4.10.: Spectroscopic ellipsometry (a) is employed to determine the refractive indices of pure Sb_2S_3, TiO_2, and P3HT:$PC_{61}BM$, respectively. The inorganic Sb_2S_3 shows high *n* values, whereas the organic P3HT:$PC_{61}BM$ shows low *n* values in comparison to TiO_2. The contour plots show the reflectivity R on a logarithmic scale for light-coupling **(b)** at a flat TiO_2/P3HT:$PC_{61}BM$ interface and **(c)** at a flat TiO_2/Sb_2S_3 interface. The reflectivity is visualized based on Fresnel equations (equations 4.1, 4.2), for unpolarized incident light and refractive indices determined in **(a)**. Dark red indicates high reflectivity, whereas dark blue indicates low reflectivity. Total reflectance is exclusively observed in **(b)**. Reprinted with permission from Pfadler et al.[106] Copyright (2015), AIP Publishing LLC.

The obtained contour plot shows the reflectivity R ($R=|r|^2$, equation 4.1) on a logarithmic scale. Dark red indicates high reflectivity, whereas dark blue indicates low

reflectivity. The asymmetry in n observed for the two active materials with respect to TiO_2 has tremendous consequences on light-coupling into the photoactive layers, namely higher reflection losses and a wavelength-dependent line of total reflection (Figure 4.10b) for a flat TiO_2/P3HT:PC_{61}BM interface. All incident light that is reflected at the TiO_2/active material interface does not contribute to any photocurrent generation in the active materials. In general, light-trapping due to textured in-scattering layers is aiming at an enhancement of the optical path length in the photoactive material. Ideally, the incident solar flux is guided along the thin-film and the limited absorption in thin-film devices is circumvented by absorbing along the lateral direction. Diffraction at the structured TiO_2/active material interface causes the incident light to be laterally scattered, but the angle dependent reflection (Figure 4.10b,c) simultaneously plays an important role. There is a tradeoff between lateral scattering and enhanced reflection both caused by the structuring of the TiO_2/active material interface. The more efficient light-coupling into high n Sb_2S_3 (i.e., less reflection losses) causes the structuring to be beneficial for the total absorption enhancement (Figure 4.8b). In contrast, high reflection losses at the low n P3HT:PC_{61}BM are responsible for the overall reduced total absorption (Figure 4.8a). We therefore conclude that the observed asymmetry in absorption enhancement (Figure 4.8a vs. 2b), which is induced by the wavelength-scale pattern, is correlated to the angle-dependent efficiency in light in-coupling (Figure 4.10b,c) that is driven by the asymmetry in n (Figure 4.10a).

Conclusion. In conclusion, we investigated the influence of wavelength-scale patterns on light in-coupling at TiO_2 active material interfaces. DLIP is employed to implement highly ordered periodic structures into two different representative thin-film solar cell architectures: an organic solar cell featuring blended P3HT:PC_{61}BM as active material, and a hybrid solar cell with Sb_2S_3 as inorganic active material. These serve as model systems for low n and high n thin-film absorbers, respectively. A quantitative spectroscopic examination shows an asymmetry in absorption enhancement for the two solar cell architectures. The implementation of a wavelength-scale pattern is beneficial for the total absorption enhancement if an active material of higher n is deposited on the structure, but detrimental for the absorption if a low n material is deposited on top. We determined the refractive indices of the pure materials with spectroscopic ellipsometry and used the Fresnel formalism to understand and to visualize the asymmetry in refractive index and correspondingly the asymmetry in light-coupling. Our findings outline that considerations based on the macroscopic Fresnel equations enable a qualitative understanding of light-coupling at nanostructured electrode-active layer interfaces, which feature a wavelength-scale pitch. This provides an easy way to assess the potential of a functional nanostructure for light absorption enhancement in thin-film solar cells.
Device characteristics of the above discussed 2D photonic solar cells were not shown in this section on light-coupling. J-V characteristics of OPVs featuring blended P3HT:PC_{61}BM as active material are discussed in the following section 4.2.3.
Even though the inorganic active material Sb_2S_3 greatly benefits from the patterning, enhanced absorption specifically in the P3HT hole conductor (cf. Figure 4.8 vs 4.9) is not harvested due to suppressed energy transfer from P3HT to Sb_2S_3 as shown by

Zimmermann and Pfadler et al.[187] From a device point of view, such a suppressed energy transfer from P3HT to Sb_2S_3 needs to be regarded as parasitic light absorption in the polymer as long as no strategies such as interfacial modification are developed to tackle the observed energy loss due to suppressed energy transfer from P3HT to Sb_2S_3. Weickert and co-workers for instance intensively investigated interfacial modifications for hybrid solar cells which require energy transfer at TiO_2/polymer interfaces to unleash the full potential of these hybrid devices.[199–202] Therefore, optimized 1D and 2D photonic solar cells, which were presented in this section, based on Sb_2S_3/P3HT bi-layers finally showed similar overall device performance. Alternatives to solely P3HT on Sb_2S_3 need to be established to harvest the full potential of such devices featuring a 2D photonic device configuration with Sb_2S_3 deposited on periodic TiO_2 structures.

4.2.3. Structure-induced Resonant Tail-State Absorption in Polymer:Fullerene Bulk-Heterojunction Solar Cells

Organic photovoltaics (OPVs) have been extensively investigated and optimized over the past two decades.[31, 203–206] The most successful and efficient solution-processed single junction OPVs were realized using a buckminsterfullerene derivative as electron acceptor, blended with a conjugated polymer as electron donor to form a phase separated bulk-heterojunction (BHJ) morphology.[207, 208] Detailed studies on these polymer:fullerene BHJ systems led to maximum efficiencies of up to 10%.[209, 210] These efficiencies in combination with their potential of being fabricated using cheap, fast, and up-scalable techniques such as roll-to-roll processing, renders OPVs highly interesting as low-cost devices for low-power applications.[211, 212]
In contrast to most inorganic photovoltaics, where weakly bound Wannier excitons are present, OPVs are so-called excitonic devices, i.e., their operation principle relies on the migration of strongly bound Frenkel excitons towards charge-separating interfaces.[19] The exciton diffusion length in OPV materials, such as the mentioned polymer:fullerene BHJ, is typically one order of magnitude smaller than the optical absorption length.[25] This limitation determines an optimized donor-acceptor spatial arrangement as well as the overall device thickness not only in BHJ solar cells, but also in any comb-like donor-acceptor architecture.[18] Nowadays, thin-film polymer:fullerene BHJ devices (typically 100 nm thick) are optimized in terms of their electronic properties. This way, internal quantum efficiencies close to unity and fill-factors approaching 80% have been realized.[35, 213] However, obtaining efficiencies approaching the radiation limit predicted by Shockley and Queisser is still highly challenging due to two major obstacles.[42, 214] First, photons of energies above the optical bandgap (E_G) are only incompletely absorbed due to the reduced (electronically optimized) active layer thickness.[35] Second, the mechanism of free-charge carrier generation across the donor-acceptor interface leads to the formation of a low-energy interfacial charge-transfer (CT) state, which has been shown to directly determine the open-circuit voltages V_{OC} of polymer:fullerene BHJ solar cells.[24, 215] There is an energy loss between the lowest optical bandgap of the single organic materials and the effective band gap of the material blend determined from the energy of this weakly absorbing CT state (E_{CT}).[215, 216] Koster

et al. (see Ref. [42]) discuss the opportunity of increasing the efficiency of the single junction OPV by harvesting $E_\Delta = E_G - E_{CT}$ instead of the photonic bandgap energy. It was shown by Vandewal et al. that the photo-response at these energies

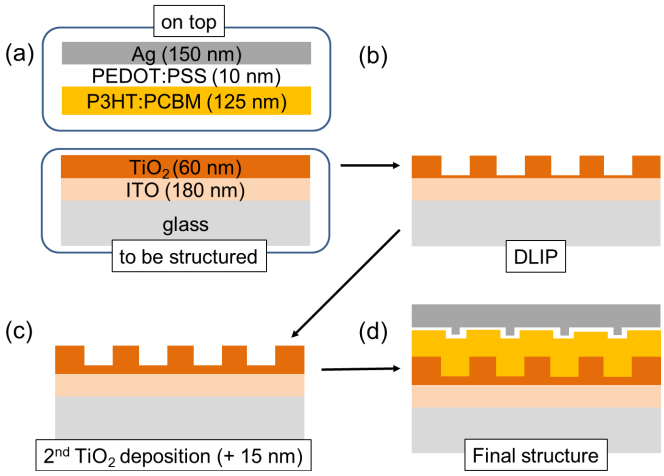

Figure 4.11.: The Figure above shows an illustrative workflow description of inverted P3HT:PCBM BHJ solar cells featuring periodically structured TiO_2 bottom electrodes. The employed materials along with the respective layer thickness are provided in Panel (a). As shown in Panel (b), Direct laser interference patterning (DLIP) is employed to transfer a two-beam interference pattern to TiO_2. After depositing an approximately 15 nm thick capping layer [Panel (c)] on structured as well as on flat reference devices, all remaining layers are deposited on top [cf. Panel (a)(d)]. Adapted from Pfadler et al.[133]

well below E_G is caused by tail-state or direct CT state absorption.[215] However, as a matter of fact this absorption is orders of magnitude lower than in the main absorption regions of the materials. To utilize this additional absorption channel, we show in this section how careful design of a solar cell consisting of periodically structured bottom electrodes, leads to an enhancement of light absorption in exactly this range of frequency. In turn, this absorption enhancement causes an increase of the external quantum efficiency (EQE) in the nanostructured devices. In addition to measurements we also provide electromagnetic simulations supporting the experimental findings. As a representative system, we employ a P3HT:PCBM BHJ in an inverted device configuration with an electron-selective TiO_2 bottom electrode (see Figure 4.11(d) and Refs. [186, 217]). Direct laser interference patterning (DLIP), a technique fully compatible with large-scale fabrication, is applied on approximately 60 nm thick anatase TiO_2 films to manufacture highly ordered structures (see Figure 4.11(b) and Refs. [128–130, 198]). We then coat the obtained TiO_2 structures, as well as the unstructured reference with another 15 nm of anatase TiO_2 to electronically guarantee comparable interfacial properties between structured and reference devices (see Figure 4.11(c)). Finally, we deposit the remaining components on top of the electrode to obtain the final device architecture (see Figure 4.11(a)(d)). In Figures 4.12(a,b), we display the TiO_2 surface topographies for two different periodicities as characterized by AFM measurements (cf. Appendix C).

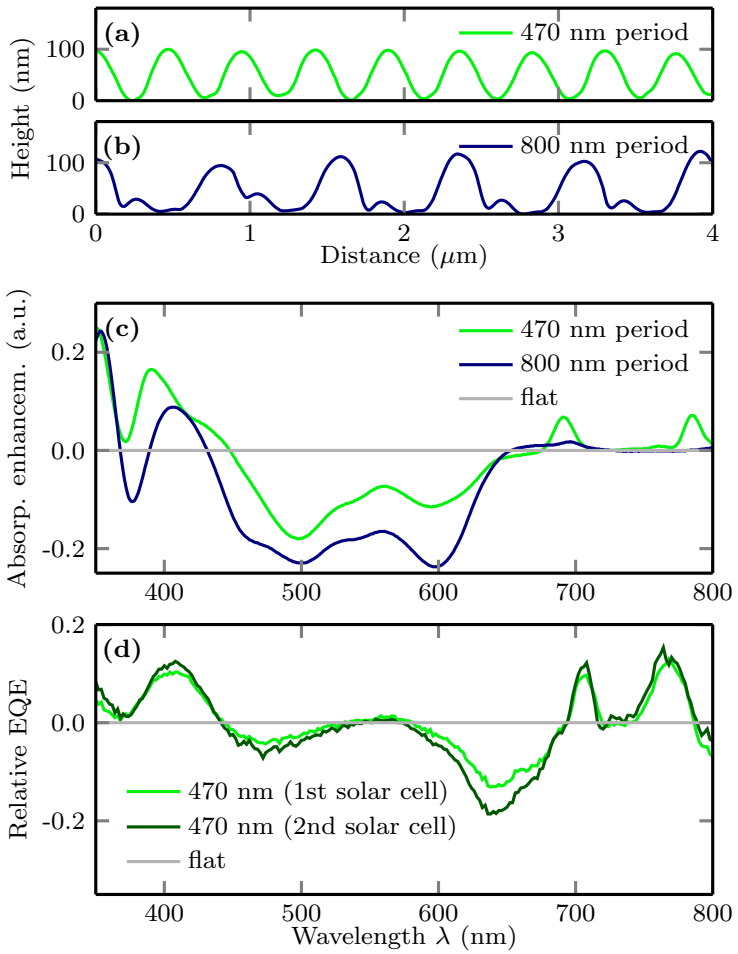

Figure 4.12.: Experimental characteristics of periodically structured solar cells. The Figure above shows in Panel (a) and (b) the surface profile of two different TiO_2 gratings created by DLIP. The measured absorption enhancements for the two solar cells built from these two different patterns with respect to the flat surface are shown in Panel (c). In Panel (d) the measured relative EQEs for two different solar cells with the same grating are shown. The two distinct absorption peaks in the red and IR in Panel (c) that were obtained by careful design of the solar cell's structure lead to a significant enhancement of the EQE [Panel (d)]. The measurements in Panel (c) and (d) were done with unpolarized light. Adapted from Pfadler et al.[133]

For two different periodicities, 470 nm and 800 nm (see Figure 4.12(a,b), respectively), we present in Figure 4.12(c) the absorption enhancement with respect to an unstructured (flat) P3HT:PCBM BHJ. In the energy range of polymer:fullerene tail-state features ($\lambda > 650$ nm), two distinct absorption enhancement peaks emerge for the 470 nm-periodicity. These resonances are structure dependent since they are barely visible in the 800 nm structure. For different solar cells with the same periodicity, these absorption resonances also lead to a strong enhancement of the EQE which can be translated into additional photocurrent (cf. Figure 4.12(d)).

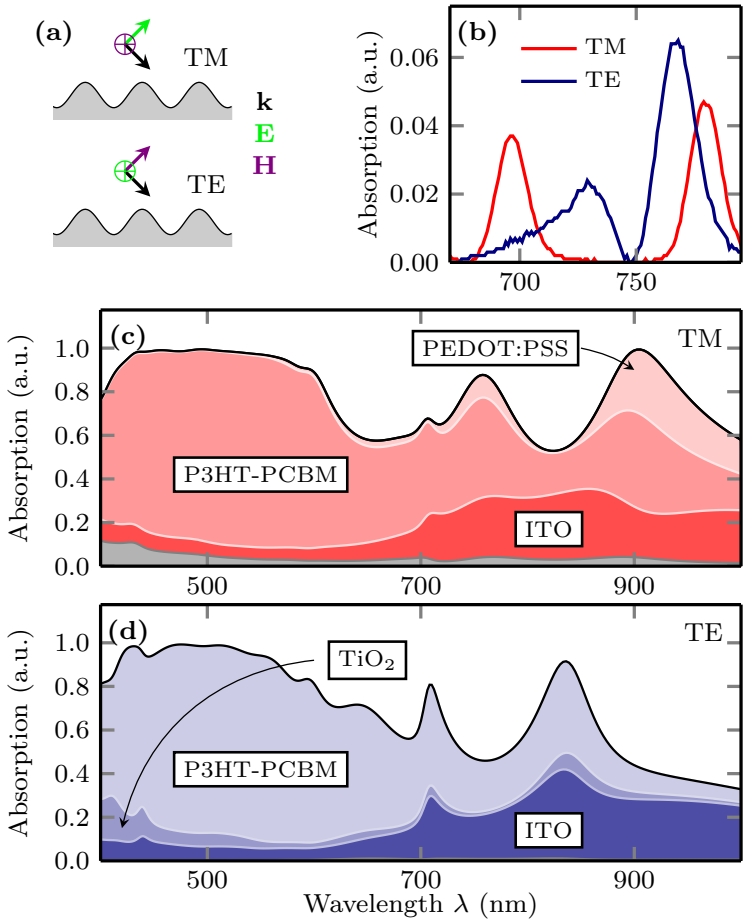

Figure 4.13.: The Figure above show experimental and theoretical results for the absorption (470 nm structure) for two different polarizations (Panel (a)). Panel (b) focuses on the two experimental absorption peaks in the tail-state absorption region, whereas Panels (c,d) present the complete numerical absorption, including the layer-dependent absorption (colored areas). This layer-resolved absorption adds up to the total absorption (black line). Adapted from Pfadler et al.[133]

As further apparent from Figure 4.12, the relative EQE is reduced in the main absorption region of P3HT. This is attributed to the large difference in refractive indices of the structured TiO_2 and the polymer:fullerene active layer, which we investigated in a corresponding study outlined in section 4.2.2.[106] The positive effect of wavelength-scale structure and refractive-index matching on light in-coupling is known from literature, e.g., at low-dielectric:amorphous silicon interfaces.[196] By inverting the direction of light coupling, e.g., from a metal-oxide into a low-dielectric OPV material, the in-coupling efficiency correspondingly decreases. While this has to be considered when finding optimized nanostructures for superlarge achievable absorption enhancement in OPVs, it only is of marginal importance for the present fundamental study focusing on resonant tail-state absorption.

In the following, we will focus on the 470 nm-periodic structure, which shows two distinct absorption resonances in the region of interest (cf. Figures. 4.12(c,d)). To further elucidate the origin and periodicity dependence of these resonances, we have performed fully vectorial electromagnetic simulations using the Discontinuous Galerkin Time Domain (DGTD) method (see Refs. [135, 136, 218] and section 3.4). The structure is represented by a sine-shaped grating as sketched in Figure 4.13(a) which is a reasonable approximation to the measured profile shown in Figure 4.12(a). We use periodic boundary conditions in the horizontal direction. Due to the translational invariance of the system the problem reduces to an effective two-dimensional problem. Further details, like the material models used as well as the strategy for computing the absorption spectrum, are outlined in section 3.4.
We compute the absorption spectrum of the idealized structure for TM and TE polarization as indicated in Figure 4.13(a). The numerical results are shown in Figure 4.13(c,d), black line. When comparing to the experimental results shown in Figure 4.13(b), we observe good qualitative agreement. Both, experiment and simulation, show absorption resonances in the wavelength region of interest $\lambda > 650$ nm. Quantitative deviations, e.g., spectral positions, can be attributed to geometrical variations present in the experimental samples. The good qualitative agreement allows us to use the numerical results to optimize structures with regard to maximum absorption in the tail state energy region. To that end, we varied the periodicity of the structure keeping all other simulation parameters constant and computed the absorption spectra. As shown in Figure 4.14, the most suited periodicities of OPV structuring are situated between 400 - 500 nm, as in our experimental samples.
So far, the structure-induced occurrence of additional absorption peaks obtained from

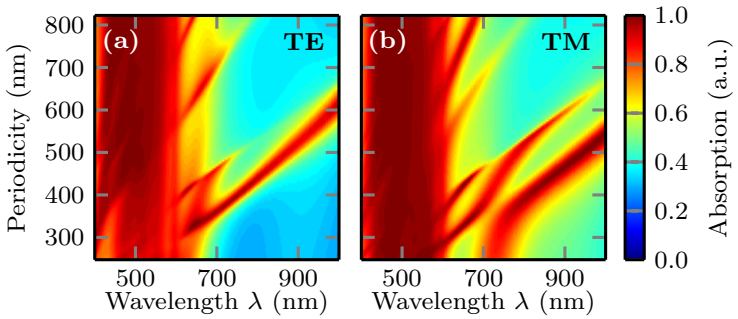

Figure 4.14.: The Figure above shows the numerical calculations of the periodicity and polarization dependent absorption. The dependence of the existence of the two to three absorption peaks for different periodicities of the structured material can be noticed. Adapted from Pfadler et al.[133]

simulation match the experiment. To resolve the spatial dependence of the absorption, we compute the time-averaged absorbed power density

$$\bar{p}_{\mathrm{loss}}(\mathbf{r},\omega) = \omega \Im\{\varepsilon(\mathbf{r},\omega)\}\mathbf{E}(\mathbf{r},\omega)\cdot\mathbf{E}^{*}(\mathbf{r},\omega). \tag{4.3}$$

The results are shown in Figure 4.15(a-e) where we plot color encoded $\bar{p}_{\text{loss}}$ at the frequencies corresponding to the five peaks observed in the absorption spectra (cf. Figure 4.13(c,d)) together with the time averaged Poynting vector

$$\bar{\mathbf{S}}(\mathbf{r},\omega) = \frac{1}{2}\Re\{\mathbf{E}(\mathbf{r},\omega) \times \mathbf{H}^*(\mathbf{r},\omega)\}. \tag{4.4}$$

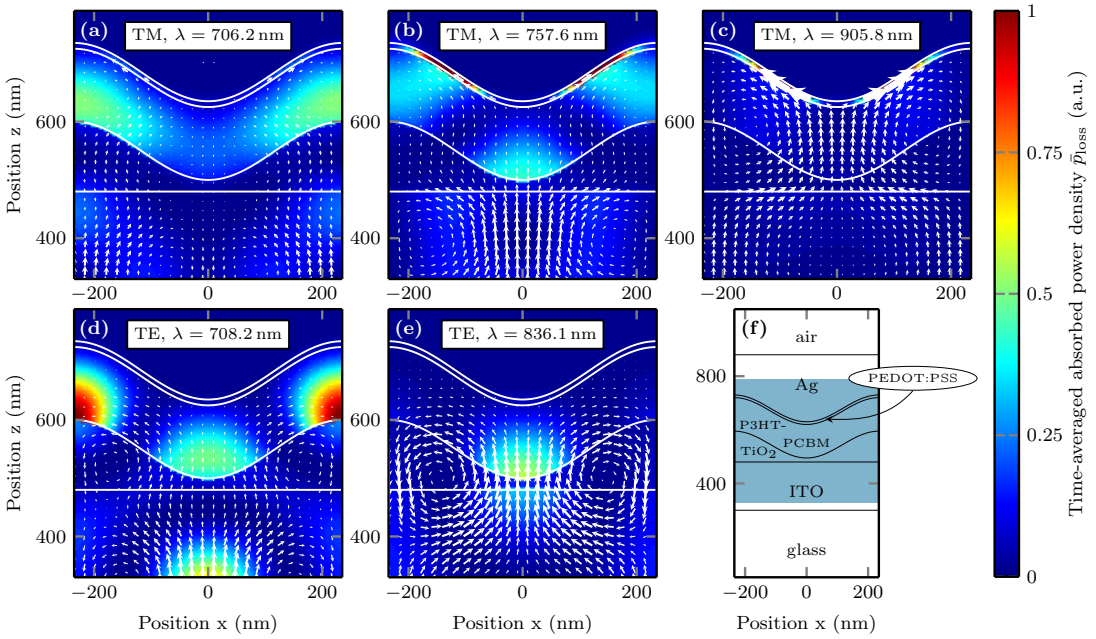

Figure 4.15.: Spatial dependence of the power loss density $\bar{p}_{\text{loss}}(\mathbf{r},\omega)$ and time averaged Poynting vector (white arrows) at frequencies corresponding to the absorption peaks at $\lambda > 700$ nm from the simulations. Panel (f) sketches the geometry, for details see supplementary information. Panels (a)-(e) only show the portion of the structure highlighted in blue in Panel (f). The active layer of the structure is P3HT-PCBM in which in Panels (a)-(e) the majority of the absorption actually takes place. Adapted from Pfadler et al.[133]

We observe high absorption in the region of the active medium, P3HT:PCBM, for all of the five frequencies. This is also stressed in Figure 4.13(c,d) where the largest fraction of the power is absorbed in the active medium, also for the absorption resonances. For the case of TM polarization [see Figure 4.15(a-c)], we observe a high loss density at the dielectric-silver interface. This is attributed to the excitation of surface plasmons at this interface, which leads to an additional light enhancement in the active medium due to waveguiding effects. For the case of TE polarization [see Figure 4.15(d,e)], the enhancement in the active material is caused by scattering at the interface between TiO_2 and the active material, leading to the formation of cavity modes.

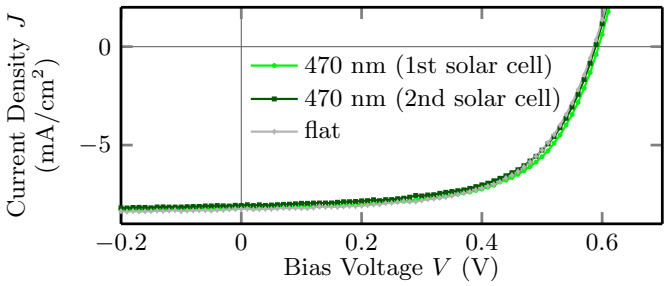

Figure 4.16.: Representative JV-characteristic of inverted P3HT:PCBM BHJ devices recorded under simulated AM1.5G conditions. The plot corresponds to the data set shown in Figure 4.12(d)). The overall device performance of structured (470 nm period) and flat reference devices is basically the same as summarized in table 4.1. Adapted from Pfadler et al.[133]

Table 4.1.: Characteristic solar cell parameters recorded under simulated AM 1.5G solar irradiance. JV parameters corresponding to the data set shown in Figure 4.16 and in Figure 4.12(d)

	J_{SC} (mA · cm^{-2})	V_{OC} (mV)	FF (%)	η (%)
470 nm (1)	-8.2	0.59	62	3.0
470 nm (2)	-8.1	0.59	61	2.9
flat	-8.3	0.59	61	3.0

These results, in combination with the experimentally observed 10% increase in EQE (cf. Figure 4.12(d)) for the 700 nm as well as the 780 nm peak, allow to conclude that a relevant part of the energy lost is transferred to tail states present in the P3HT-PCBM.[215]
We note that, owing to the reduced absorption in the main absorption range of P3HT (cf. Fig. 4.12(c)(d)), significant improvement in the overall device performance, i.e., in the JV-characteristic Figure 4.16 is not observed. However, further optimization focusing on enhanced light-coupling in the main absorption region due to refractive index matching with respect to the structured bottom electrode can lead to higher efficiencies in polymer:fullerene devices as shown by Meier et al. [219] and further discussed in section 4.2.2. Such optimization would be mandatory to assure that the acquired gain due to resonant tail-state absorption is not outbalanced by reflection losses in the main absorption region as observed in our present system.

Conclusion. The study illustrates how resonant absorption enhancement in a common OPV material system can be achieved using a rapid texturing technique like DLIP. Experimental findings of increasing tail state absorption and EQE are supported by numerical simulations, which further outline the tuneability of the absorption resonances towards arbitrary wavelength regions in the UV-Vis and NIR. We identify the possibility to precisely design the absorption properties of an OPV using a fully roll-to-roll compatible fabrication technique as a potential pathway towards absorption edge-enhanced

OPVs. It might further be possible to resonantly enhance the typically very weak absorption of charge transfer states, which could close the gap between net optical and electric band gap of OPVs.
Future studies could focus on the implementation of not only one lateral periodicity, but several ones to obtain hierarchical structures in different lateral directions in order to acquire broadband tail-state absorption in OPVs. Such hierarchical structures could be realized via a series of two-beam laser interference patterning steps (at varying periodicities) each single one with respect to different lateral in-plane directions of the thin-film.
Alternatively, non-inverted polymer:fullerene devices featuring a 2D photonic structure are expected to support efficient light-coupling due to refractive index matching (cf. section 4.2.2) and light-trapping as discussed in this section. For this purpose, electron selective TiO_2 bottom electrodes would be replaced with low n PEDOT:PSS and the Ag backelectrode would be replaced by Al. Even though a drastic change in light management is expected, such a structure has the potential to be optimized towards enhanced overall device performance due to highly effective light-trapping and optimal in-coupling of light. Note, polymer:fullerene blends typically show higher refractive indices than PEDOT:PSS and are therefore expected to support efficient light-coupling as discussed in section 4.2.2.
This section on structure-induced light-trapping focused on absorption edge-enhanced photoactive polymer:fullerene systems. Resonant absorption enhancement can be obtained for Sb_2S_3/P3HT devices as well, which is shown in Figure 4.8b for the 470 nm period structure at wavelengths around 700 nm. However, the quality of the conformal coating process following a simple chemical bath deposition of Sb_2S_3 on TiO_2 patterns turned out to be challenging and less controllable than spincoating an organic blend solution. The conformal coating and thereby the long-range order along with the occurence of resonant absorption features turned out to be disturbed by Sb_2S_3 crystallites on top of the Sb_2S_3 thin-film. These crystallites were observed to be already formed in the chemical bath solution. As shown by Wedemeyer et al. high quality and conformal Sb_2S_3 layers on high interfacial TiO_2 nanostructures can be alternatively deposited via atomic layer deposition, even though the layer by layer deposition is comparably very time consuming.[220]

5. Internal Quantum Processes

The following chapter is based on the research paper *Influence of interfacial area on exciton separation and polaron recombination in nanostructured bilayer all-polymer solar cells* which I have written as part of my Ph.D.[18] For this study I fabricated all solar cells and did most of the measurements for data shown in the publication. *M. Coric* did initial experiments and solar cell characterization. I wrote the manuscript and was responsible for editing.

5.1. Nanoembossed Donor-Acceptor Interface

Device preparation

(illustrated in Figure 5.2): ITO substrates (PGO, 10 $\Omega\,\square^{-1}$) were cleaned by ultrasonic bath using deionized water with dishwashing detergent, acetone and isopropanol for at least 5 min each followed by 7 min O_2 plasma cleaning (Diener Femto). Approximately 50 nm of TiO_2 was deposited via spray pyrolysis of a titanium diisopropoxy bisacetonate precursor (Sigma Aldrich) solution diluted 1:10 (vol:vol) in ethanol. Clean substrates were heated to 450°C with a ramp rate of 30°C min^{-1}. The precursor solution was then deposited using a spray nozzle, annealed at 450°C for 15 min, and cooled naturally. A layer of approximately 60 nm of the n-type polymer P(NDI2OD-T2) layers (10 mg ml^{-1}, dissolved in xylene) containing 5 wt% sFPA additive (synthesized according to Png et al.) were spincoated (45 s/ 1500 rpm, 15 s/ 2000 rpm) in a nitrogen filled glove box on clean glass/ITO/TiO_2 substrates.[33]
Nanoimprint lithography (cf. section 3.5) of P(NDI2OD-T2) films was performed with a mechanical hotpress (Collin GmbH) for 5 min at 60°C under a pressure of $350 \cdot 10^7$ Pa. Accordingly, flat (un-patterned) P(NDI2OD-T2) films were placed on a hotplate (5 min at 60°C) in order to maintain comparable thermal processing. The sFPA photo-crosslinker was activated by exposing the samples with a DUV (254 nm) and an approximate dose of 300 mJ cm^{-2} under controlled conditions (oxygen content below 3 ppm).
Solvent washing was realized by solvent soaking (200 μl drop) and subsequent spincoating (1 min, 2000 rpm) of pure toluene. Solvent washed films were kept overnight in a nitrogen filled glove box, equipped with a solvent absorber system. An approximately 60 nm thick layer of the p-type polymer P3HT (Merck, 10 mg ml^{-1}, dissolved in toluene) was spincoated (45 s/ 1500 rpm, 15 s/ 2000 rpm) on top of the dried P(NDI2OD-T2) films.
Finally, a thermally evaporated top contact of 5 nm WO_3/ 150 nm Ag top electrodes was added to device. Evaporation was carried out at a base pressure below $5 \cdot 10^{-4}$ Pa.

5.2. Influence of Interfacial Area on Exciton Separation and Polaron Recombination in Nanostructured Bi-Layer All-Polymer Solar Cells

The internal quantum efficiency η_{IQE} (equation 2.1 and 2.2, and Figure 2.2) is determined by processes that are covered by the electronic properties of the photoactive materials and the spatial ordering of the donor-acceptor network (Figure 2.1) of excitonic solar cells.[37] The charge carrier harvesting in a bi-layer heterojunction architecture in comparison to a BHJ device is spatially limited to excitons generated within the exciton diffusion length to the flat donor-acceptor interface. However, the perfect bi-continuous network provides direct percolation pathways for polarons to the respective electrodes. From a theoretical point of view, a bi-layer heterojunction device featuring a controlled nanostructured interface is considered as the perfect donor-acceptor morphology.[37, 221, 222] He et al. demonstrated a solvent assisted nanoimprint lithography (SANIL) technique that allowed the formation of nanostructured F8TBT/P3HT all-polymer bi-layer devices with an outstanding power conversion efficiency of 1.9 %.[147] They compared BHJ, flat bi-layer and nanopatterned bi-layer all-polymer devices with feature sizes up to 25 nm on a 50 nm pitch. A direct correlation between enhanced donor-acceptor interfacial area and η_{EQE} was found for the bi-layer devices. Finally, it has been shown that the simultaneous enhancement in short-circuit current density (J_{SC}) and the overall device efficiency, extracted from standard current-voltage measurements (J-V measurements), is directly correlated to the enhancement in interfacial area. In this section, we present new bottom-up, solution processed, nanoembossed donor-acceptor heterostructures for organic solar cells (cf. Figure 2.1d). We investigate a nanostructured bi-layer system consisting of the p-type polymer poly(3-hexylthiophene-2,5-diyl) (P3HT) and the n-type polymer poly([N,N'-bis(2-octyldodecyl)-naphthalene-1,4,5,8-bis(dicarboximide)-2,6-diyl]-alt-5,5'-(2,2'-bithiophene)) (P(NDI2OD-T2)).[217, 223–226] This material composition serves as a well-known model system. Recently, the n-type polymer P(NDI2OD-T2) has shown impressive efficiencies up to 5.7 % in combination with a NIR donor polymer.[227] Most importantly, the complementary absorption (Figure 5.1) of P(NDI2OD-T2) and P3HT facilitates the elucidation of the donor and acceptor contributions in spectrally resolved measurements. Furthermore, the tendency of P(NDI2OD-T2) to form aggregates even in solution, the necessity to use a mixture of solvents and special temperature treatments to realize sufficient BHJ solar cells are removed through the bi-layer model system.[228] A distinct donor-acceptor interface in this bottom up solution process is realized via photo-crosslinking (section 3.6) of the P(NDI2OD-T2) network and the subsequent deposition of P3HT from solution. Anodized aluminum oxide (AAO) membranes (cf. Figure 3.9), featuring self-organized hexagonally nanopore arrays of different sizes, are used in a nanoimprint lithography (NIL) process (section 3.5) to tailor the topography of the P(NDI2OD-T2) layer.[146, 150] In addition to the common local real space characterization techniques, like scanning electron microscopy (SEM) and atomic force microscopy (AFM), a statistically averaged reciprocal space analysis method (section 3.1), namely grazing incidence resonant soft x-ray

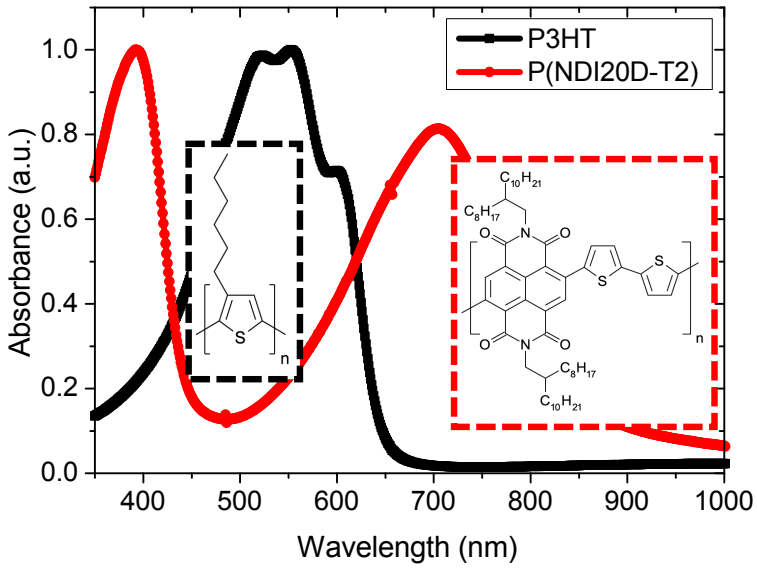

Figure 5.1.: Representative absorption characteristics of P(NDI2OD-T2) and P3HT. Three distinctive absorption peaks at around 400 nm, 550 nm and 700 nm are visible. The structural formulas of the employed polymers are provided as an inset to the absorption characteristics, respectively. Adapted with permission from Pfadler et al.[18] Copyright (2014) American Chemical Society.

scattering (GI-RSoXS), is applied to probe the quality of the nanoimprinting process and the final interdigitating structure. For this investigation, nanostructured bi-layer devices were shown to have a direct correlation between enhanced donor-acceptor interfacial area and an enhancement in EQE. As found from EQE spectra, both excitons generated in the donor as well as in the acceptor polymer equally contribute to the relative enhancement. The enhancement in EQE is subsequently visible in the corresponding J-V measurements with an increased J_{SC}. More importantly, we focus on the influence of an enhanced donor-acceptor interfacial area on polaron recombination processes for different solar cell working regimes. For this purpose, our fundamental study encloses complementary measurement techniques, such as diode dark current characteristics, transient photovoltage (TPV) and impedance spectroscopy (IS). Furthermore, our investigation shows that the controlled enhancement of donor-acceptor interfacial area on a nanometer scale is beneficial for the harvesting of photoexcitons, while simultaneously enhancing the undesired polaron recombination losses in excitonic solar cells. Finally, the measured enhancement in polaron recombination, correlated to the donor-acceptor interfacial area, potentially limits the efficiency of organic solar cells featuring the theoretically hypothesized comb-like and perfectly ordered heterostructure morphology.[221, 222]

Device Preparation and Structure Characterization

Bottom-up Processing of Nanoembossed All-Polymer Bi-Layer Solar Cells. A workflow description for the bottom up synthesis of nanostructured donor-acceptor junctions employed in this study is illustrated in Figure 5.2. The method is generally applicable

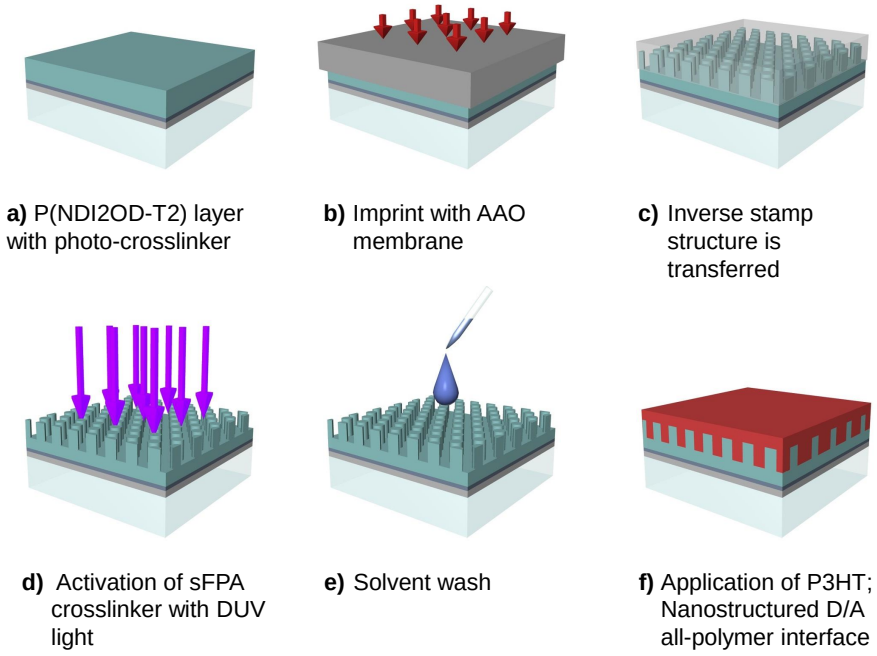

Figure 5.2.: Illustrative workflow description of nanostructured bi-layer solar cells. (a) A P(NDI2OD-T2) layer containing sFPA additive is spincoated on an electron selective glass/ITO/TiO_2 bottom support. **(b)** An AAO membrane is used as master mold structure in a NIL process. **(c)** Inside view during molding; the inverse stamp structure is transferred. **(d)** Activation of the sFPA photo-crosslinker with deep ultraviolet (DUV) light. **(e)** Removal of uncrosslinked and low molecular weight fractions in a solvent spin rinse step; denoted as solvent wash. **(f)** P3HT spincoating. Adapted with permission from Pfadler et al.[18] Copyright (2014) American Chemical Society.

to arbitrary polymer-polymer (n-type/p-type) combinations that energetically form a type II heterostructure. Furthermore, the technique can be employed with the previous requirement for additional material compositions, such as polymer-fullerene combinations in a regular solar cell configuration.[34] However, when using a fullerene acceptor as second layer it is important to consider possible interdiffusion of fullerenes into the polymer layer.[229–231] It is necessary that the bottom layer consists of a polymer material in order to successfully maintain the patterned layer after photo-crosslinking. In a NIL process, a polymer layer can be structured in-situ and thermally developed under the influence of heat and pressure due to the temperature dependent viscosity of polymers.[232] During molding, the polymer layer is softened and flows into the adjacent

stamp structure. Subsequently, the polymer crystallizes during the cool down process and the inverse master mold structure is transferred to the topography of the polymer film. The photo-crosslinking methodology is based on the usage of sterically hindered bis(fluorophenyl azide)s (sFPAs), whose dominant reaction is the alkyl side-chain insertion.[33] The semiconducting properties of the polymer are virtually unaffected due to the dominant alkyl side-chain insertion of the sFPA and the simultaneous suppressed insertion into π-conjugated cores. Additionally, Png and co-workers showed that the photo-crosslinking of polymers is more effective for high-molecular mass polymers, since statistically one sFPA molecule is necessary to crosslink two polymer chains.[33] The photo-crosslinking efficiency is determined by measuring gel curves that are plots of film-retention (cf. Figure 3.10) as a function of crosslinker concentration.[33, 34] The workflow description in Figure 5.2 illustrates the specific material processing steps that are necessary to realize a solution processed all-polymer bi-layer. A solution of the n-type high-molecular weight polymer P(NDI2OD-T2) together with the sFPA additive is spincoated on top of a glass/ITO/TiO_2 electron selective bottom support (Figure 5.2a). Such a device configuration, where electrons are extracted through the ITO layer is regarded as an inverted device structure.[186, 210] For our system, we chose a stiff photo-crosslinked P(NDI2OD-T2) network with around 95 % film retention (Figure 5.3). Next, the glass/ITO/TiO_2/P(NDI2OD-T2) plus imprinting mold sandwich

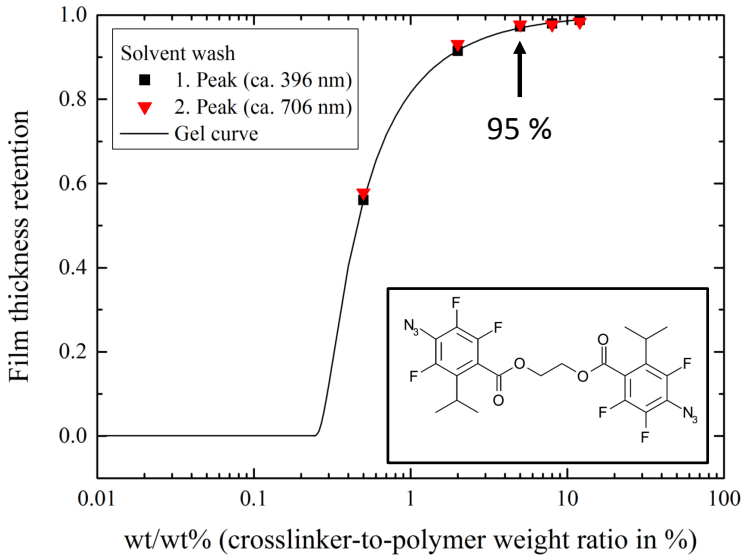

Figure 5.3.: Film-retention characteristic (gel curve) of P(NDI2OD-T2) using sFPA as photo-crosslinker. A P(NDI2OD-T2) film containing 5 wt% sFPA (inset bottom right) additive results in approximately 95 % film-retention. Compare to gel curves for monodispersed PS standards shown in Figure 3.10b. The film thickness retention is determined as discribed in section 3.6 for the two distinct P(NDI2OD-T2) absorption peaks as shown in Figure 5.1. Adapted with permission from Pfadler et al.[18] Copyright (2014) American Chemical Society.

structure is placed into a mechanical hotpress. The imprinting process and an additional inside view during molding are sketched in Figure 5.2b, c. The thermally

softened P(NDI2OD-T2) flows into the adjacent master mold structure, which is locked into the final, topographical, inverse replica of the master mold once cooled. However, at this stage, the structured n-type layer is still vulnerable and can be lost during the spincoating of the second polymer layer. An insoluble bottom layer is fabricated by activating the sFPA crosslinker additives with deep ultra-violet light (Figure 5.2d). Subsequently, uncrosslinked and low-molecular-weight fractions are removed by a solvent rinse step, denoted as solvent wash in Figure 5.2e. The well-ordered interdigitating all-polymer morphology is finalized by spincoating P3HT on top of the P(NDI2OD-T2) nanocolumns. Not shown in the schematic illustration of Figure 5.2 is the last preparation step, the thermal evaporation of a hole selective WO_3/Ag top contact.

Local Real Space Nanostructure Characterization. In this section, we investigate the influence of the controlled enhancement of donor-acceptor interfacial area on fundamental processes in organic solar cells. For this purpose, a comparison of a flat unstructured and two nanoimprinted architectures with an increasing donor-acceptor interface is performed. A summary of extracted geometries is given in Figure 5.4. SEM pictures of two different AAO membranes which serve as master mold structures in the NIL process (Figure 5.2b, c) are shown in the first column of Figure 5.4. The AAO surface formation is based on an electro-chemically driven self-organizing process. The period of the highest packing density honeycomb structure can be tuned in a range of 60 nm - 500 nm through the subsequent processing conditions and the specific pore diameter is finally tuned in an isotropic chemical etching process under controlled conditions.[150] For this study, we chose two master structures, both with the same lattice period of 100 nm, whose processing conditions only differed in terms of the final chemical etching process, thus yielding 35 nm pore diameter (Figure 5.4a) vs. 75 nm pore diameter (Figure 5.4d). Corresponding AFM topographic height profiles of the resulting nanopatterned P(NDI2OD-T2) films are shown in the same row (Figure 5.4b,e), respectively. The right hand side of each AFM picture shows the corresponding AFM line sections (Figure 5.4c,f). By assuming a simple geometrical model (Figure 5.4g), we give a quantitative starting point for the difference in surface area of the 35 nm and the 75 nm nanopore master mold structure (Figure 5.4a, d, g). The 100 nm periodicity of the honeycomb lattice also is the maximum diameter of one unit cell (Figure 5.4g). The shape of a nanopore (Figure a, d) is assumed to be a hemisphere due to the nature of the isotropic etching process. The surface area (S) of one unit cell scales quadratically with the length (L) of the 1D surface line (Figure 5.4g) of a unit cell. This length was determined from a simple one dimensional consideration taking the specific pore diameter and the width of the unit cell into account. By relating S2 to S1 (Figure 5.4g), the geometrical correction factors due to the 1D to 2D transition cancel out and a difference in total surface area of 36 % is estimated for the 35 nm and 75 nm master mold structure. Liu and co-workers showed that a good solvent causes a crosslinked polymer network (P3HT with sFPA) to swell and expand.[34] Consequently, an exact value for the height of a nanocolumn in our final interdigitating donor-acceptor network is hard to determine, but the solvent wash (Figure 5.2e) is estimated (AFM) to cause around 65 % reduction in nanocolumn height with respect to the structure size before washing (ap-

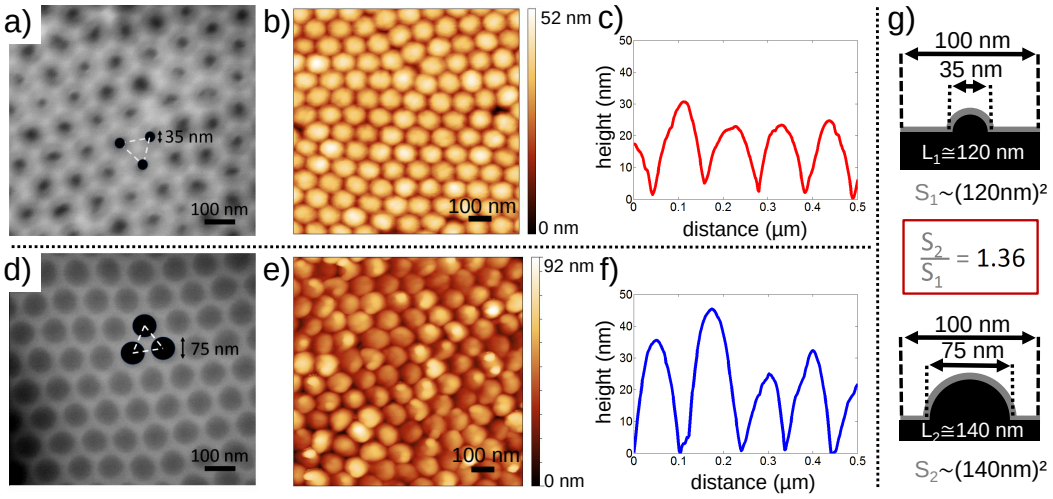

Figure 5.4.: Comparison of extracted topographies. The 35 nm structures are shown in the first row and the 75 nm structures are shown in the second row. Each column offers a direct comparison of the respective nanostructures. (a,d) SEM pictures of the master mold structures used in the NIL process. Both AAO membranes feature a honeycomb lattice with a periodicity of 100 nm and only differ from each other in terms of the specific pore diameter. **(b,e)** AFM topographic height profiles of imprinted P(NDI2OD-T2) films. **(c,f)** Corresponding AFM line sections are representatively shown. **(g)** A simplified model to give a quantitative starting point for the difference in surface area of the two employed master mold structures. The 75 nm structure is estimated to feature 36 % surface enhancement over the 35 nm structure. Adapted with permission from Pfadler et al.[18] Copyright (2014) American Chemical Society.

pendix, Figure D1). By spincoating P3HT (Figure 5.2f) on top of the nanostructure, the film swells and expands again. Opposite to the case after solvent washing (Figure D1) the swelled nanostructure is filled with P3HT, which prevents the nanotopography from contracting. Accordingly, the final nanocolumn height at the donor-acceptor interface is expected to be smaller than measured before the solvent treatment (Figure 5.4b,c,e,f), but taller than the contracted topography after solvent washing (Figure D1). Further measurements like transmission electron microscopy (TEM) cross-sections, or TEM tomographic studies could give access to the donor-acceptor interface pattern of the final architecture, although the similarity of the two interdigitating compounds is expected to limit the contrast at the polymer-polymer interface. Nevertheless, even nanocolumn heights down to a few nanometers have a strong impact on the donor-acceptor interface physics since the exciton diffusion length of typical semiconducting polymers commonly does not exceed 10 nm.[233, 234] Additionally, the overall interfacial area enhancement is affected by both the size of a single nanocolumn and the NIL large-area processability.

Statistical Averaged Reciprocal Space Nanostructure Analysis. The previous section on local real space characterization focused on the dependency of donor-acceptor interface enhancement on the shape of single nanopillars (Figure 5.4). The overall surface enhancement due to the structuring of the P(NDI2OD-T2) layer is additionally determined by the large-area processability due to the NIL process. Finally, the preservation of the distinct donor-acceptor interface after solution casting of the second polymeric layer is crucial for the overall device performance. Advanced scattering techniques like grazing incidence small angle scattering (GISAXS) give access to statistically averaged structure information on an illuminated real space area comparable to the size of our organic solar cells.[235] In this study, we characterized structured P(NDI2OD-T2) layers featuring the 75 nm structure (Figure 5.4) with GI-RSoXS and GISAXS.[235, 236] Measurements were performed at the synchrotron beamlines 11.0.1.2 and 7.3.3 of the Advanced Light Source (ALS) in Lawrence Berkeley National Lab (USA) and offer the possibility to probe samples at material specific resonant scattering features.[237–239] Hard X-ray GISAXS measurements statistically verified the large area processability due to the NIL process when investigating imprinted P(NDI20D-T2) films without a P3HT capping layer.[240] However, the buried interdigitating donor-acceptor interface after deposition of the second polymeric layer could not be resolved (Figure 5.5). RSoXS shares many advantages with GISAXS in characterizing the mor-

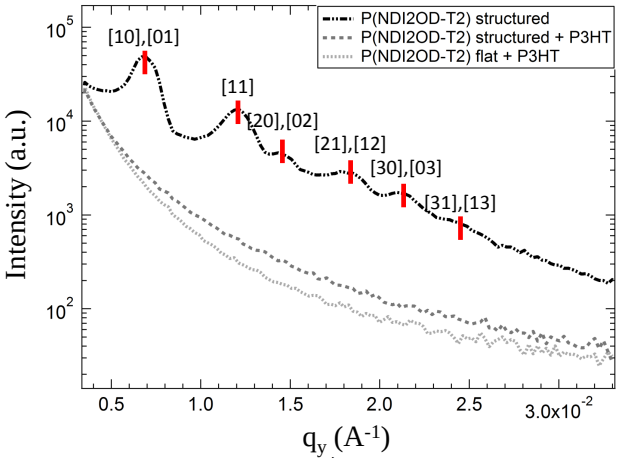

Figure 5.5.: GISAXS reciprocal space analysis of the hexagonally structured polymer-polymer interface. GISAXS reciprocal space analysis of the hexagonally structured polymer-polymer interface. Scattering patterns (cf. Figure 5.6) are originating from the structured P(NDI2OD-T2) film. The filling of the structured P(NDI2OD-T2) topography with solution coated P3HT is complete and the pattern is furthermore not transferred to the P3HT-air interface, since no coherent scattering is observable for the structured P(NDI2OD-T2) with P3HT on top. Adapted with permission from Pfadler et al.[18] Copyright (2014) American Chemical Society.

phology of a large variety of materials.[235, 241–245] For characterizing the structure of organic soft matter with hard X-rays, the contrast of scattering between two materials relies on the difference in electron densities in the first and second material.[235] In

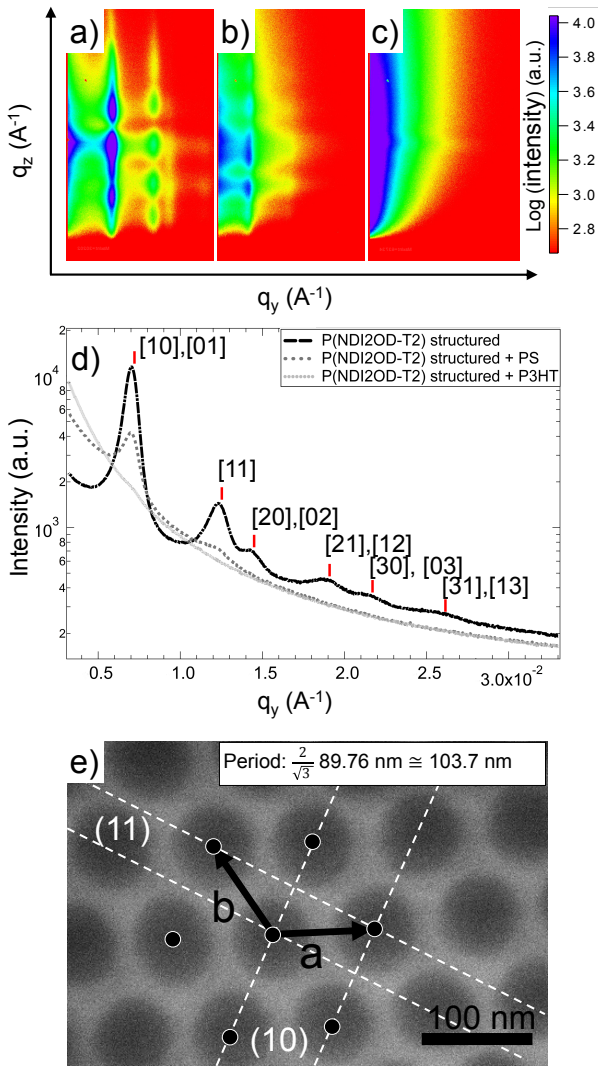

Figure 5.6.: GI-RSoXS reciprocal space analysis of the hexagonally structured polymer-polymer interface. Scattering patterns originating from the imprinted P(NDI2OD-T2) film without capping layer **(a)**, with solution coated PS homopolymer on top **(b)** and with solution coated P3HT on top **(c)**. The logarithmic scale of the scattering intensity is in arbitrary units. Red represents low intensity and blue represents high intensity. A horizontal cut summary of the three different architectures with the corresponding Miller indices is given in **(d)** and further summarized in Table 5.1. The **(10)** and **(11)** scattering planes originating from the 2D AAO honeycomb master mold structure are highlighted in **(e)**. A period of 103.7 nm is calculated from the **(10)** scattering plane **(inset of e)**. Adapted with permission from Pfadler et al.[18] Copyright (2014) American Chemical Society.

the case of P(NDI2OD-T2):P3HT this electron density difference gives insufficient contrast between the materials.[246] With RSoXS and the possibility of varying the energy of the soft X-rays one can yield chemical contrast between the two components near

Table 5.1.: Reciprocal scattering peaks (q), real space lattice parameters (D) of the imprinted 2D honeycomb lattice and the ratio of higher order peak positions corresponding to a 2D hexagonal packing (2D HXP) arrangement. Scattering features up to the third order (Figure 5.6) are measured by GI-RSoXS on nanostructured P(NDI2OD-T2) layers that feature a 75 nm topography (Figure 5.4e,f) with a spacing of 103.7 nm calculated from the scattering results according to Figure 5.6e.

[hk]	[10],[01]	[11]	[20],[02]	[21],[12]	[30],[03]	[31],[13]
q [nm-1]	0.070	0.121	0.140	0.185	0.210	0.252
D [nm]	89.76	51.83	44.88	33.96	29.92	24.89
2D HXP-ratio	1	$\sqrt{3}$	2	$\sqrt{7}$	3	$\sqrt{13}$

the absorption edge for specific elements.[241, 242, 247–249] This contrast arises due to differences in the chemical structures reflected as the complex refractive indices of P(NDI2OD-T2) and P3HT. Traces of the resonant first order scattering feature (Figure 5.6c) that coincides with the first order feature of the structured P(NDI2OD-T2) without P3HT on top (Figure 5.6a) could be observed by minimizing diffuse scattering from the P3HT-air(vacuum) interface.[250] The strongest contrast was found at an energy of 283.8 eV. The comparably weak scattering signal shown in Figure 5.6c is attributed to a weak contrast between P(NDI2OD-T2) and P3HT rather than a structural damage of the nanopattern upon solution coating. In order to verify this, a polystyrene (PS) homopolymer, instead of P3HT, was solution coated on the P(NDI2OD-T2) structure. The difference in refractive index between P(NDI2OD-T2) and PS is higher in comparison to P(NDI2OD-T2) and P3HT at an energy of 283.8 eV. Samples with PS on P(NDI2OD-T2) show resonant first and second order scattering features (Figure 5.6b) due to the honeycomb structured interface and significantly more contrast. This becomes apparent when exemplarily comparing the amplitudes of the first order scattering feature for the three samples without capping layer, with P3HT and with PS in the horizontal cut plot summary of Figure 5.6d. Hexagonal scattering is observed up to the third order, which is strong evidence for a good ordering over the whole illuminated area, i.e., the large-area processability due to the NIL process. Each point, and thereby each scattering peak position of the nanostructured P(NDI2OD-T2) (shown in Figure 5.6d and summarized in Table 5.1), corresponds to a set of lattice planes in the real space that are represented for the master mold structure in Figure 5.6e. From the spacing of the real space planes the pillar-to-pillar spacing of 103.7 nm (inset of Figure 5.6e) is calculated from scattering along the (10) lattice axis. Results from the GI-RSoXS characterization of the nanostructured bi-layer architectures show that the NIL process of the first polymer layer in combination with solution casting of the second layer is successful over the whole imprinted surface. At the same time the absence of contrast in hard GISAXS scattering (Figure 5.5) is indicative of two important aspects. First, it is direct evidence that the filling of the P3HT into the nanostructured P(NDI2OD-T2) is complete. Additionally, it demonstrates that the periodic patterning of the polymer:polymer interface is not transferred to the P3HT:air(vacuum) interface, indicating that the geometry of the Ag backelectrode is independent of the patterned

bi-layer interface. Note that air enclosures both at the interface and the structured P3HT:air(vacuum) interface would dramatically increase coherent scattering reflected in strong scattering features.

Device Physics

The performance of excitonic solar cells is drastically influenced by the spatial ordering, a type II heterostructure energy level alignment of donor and acceptor, and the total donor-acceptor interfacial area. In this work, we prepared nanoembossed bi-layer, all-polymer solar cells with a distinct and enhanced donor-acceptor interface (Figure 5.2, 5.4). The complementary absorption (Figure 5.1) of the n-type P(NDI2OD-T2) and the p-type P3HT together with the well-ordered, bi-continuous morphology featuring a controlled enhancement in interfacial area allow the investigation of the influence of the donor-acceptor interfacial area on fundamental polaron generation and recombination processes in our model system for an comb-like all-polymer device. Different complementary solar cell characterization techniques, focusing at different working regimes of the excitonic solar cells are presented and discussed in the following sections.

JV and EQE Measurements. The results of the J-V and the EQE measurements are plotted in Figure 5.7. Inverted all-polymer solar cells featuring a flat, a 35 nm, and a 75 nm pore diameter structure were examined (Figure 5.4). The results of representative J-V measurements under simulated AM 1.5G solar illumination are plotted in Figure 4a and the corresponding characteristic solar cell parameters are summarized in Table 5.2. There are three different working regimes of the solar cells shown in Figure 5.7a. Starting at negative bias, the crossing point of a J-V characteristic with the vertical current density axis is denoted as short-circuit current density J_{SC}.[251] At zero bias, in good approximation no charge-carriers are injected through the electrodes and only photo-generated charge-carriers contribute to the measured current. The origin of the J_{SC} in excitonic solar cells is the photoinduced charge transfer across the donor-acceptor heterojunction.[24] The generated photocurrent in our model system is directly correlated to the enhancement in donor-acceptor interfacial area, the origin of which will be discussed in more detail with the spectrally resolved EQE measurement. The area covered by the fourth quadrant of the J-V plot is the regime where a photovoltaic device generates power.[251] The crossing point of an J-V characteristic with the horizontal bias axis is denoted as the open circuit voltage V_{OC}.[251] The origin of the V_{OC} is still a hot topic in the organic solar cell community, but a detailed discussion of theoretical approaches that describe the V_{OC} is beyond the scope of this section. However, from a device point of view, the value of the V_{OC} that is extracted from a J-V measurement mirror the point at which the device is in a dynamic steady state between photo-generated charge carriers and charge carriers that are injected through the electrodes since there is no net current in the electrical circuit. Values of the V_{OC} for the different geometries are summarized in Table 5.2.

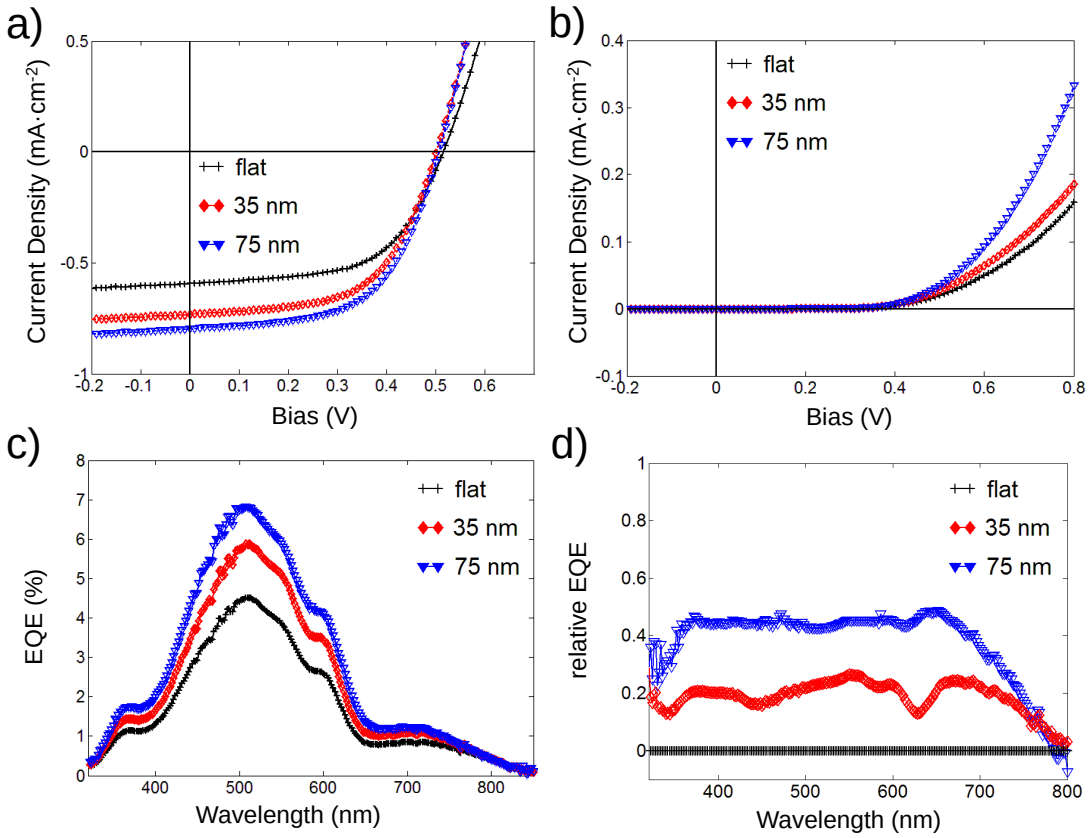

Figure 5.7.: Representative J-V and EQE characteristics of comb-like bi-layer devices featuring an enhancement in interfacial area. **(a)** J-V characteristics recorded under simulated AM 1.5G solar illumination. **(b)** Diode dark current characteristics emphasizing polaron recombination in forward direction. **(c)** Corresponding EQE of nanostructured devices. **(d)** Relative EQE enhancement: [EQE(structured)-EQE(flat)] · [EQE(flat)]$^{-1}$. Adapted with permission from Pfadler et al.[18] Copyright (2014) American Chemical Society.

Table 5.2.: Characteristic solar cell parameters recorded under simulated AM 1.5G solar irradiance. The values are extracted from the J-V characteristics shown in Figure 5.7a

	V_{OC} (mV)	J_{SC} (mA cm^{-2})	FF (%)	η (%)
flat	515	- 0.59	58	0.18
35 nm	501	- 0.73	57	0.21
75 nm	506	- 0.80	58	0.23

The flat reference shows the highest V_{OC} of 515 mV and a significantly lower slope in forward direction (bias larger than the V_{OC}) than the 35 nm and 75 nm structure. This is a first indication of enhanced recombination in the nanostructured devices, since a dependency of the V_{OC} on dynamic processes like interface recombination is already known from literature.[215, 252, 253] It is important to note that the effect of enhanced photocurrent and increased recombination is indicative for an enhanced donor-acceptor interfacial area. A similar trend in J-V characteristics (Figure 5.8, Table 5.3) was found by tuning the interfacial area via back-infiltration of P3HT into P(NDI2OD-T2) devices following the procedure of Liu et al.[34] In order to simplify the discussion of

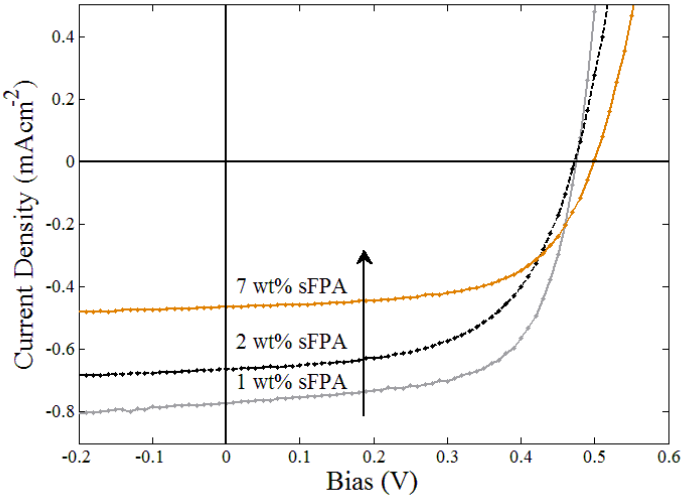

Figure 5.8.: Representative J-V characteristics of photo-crosslinked and back-infiltrated P(NDI2OD-T2):P3HT devices featuring an increasing amount of the sFPA molecule. The donor-acceptor interfacial area is reduced by increasing the amount of sFPA (cf. Figure 5.3). J-V characteristics are recorded under simulated AM 1.5G solar illumination. Adapted with permission from Pfadler et al.[18] Copyright (2014) American Chemical Society.

the nanostructured bi-layer devices at the V_{OC} and further focus on the forward bias working regime, photo-generated charge carriers are excluded by measuring the diode dark current characteristics (Figure 5.7b). If a forward bias larger than the injection barrier is applied, the electrodes effectively inject charges into the organic bi-layer de-

Table 5.3.: Characteristic solar cell parameters recorded under simulated AM 1.5G solar irradiance. The values are extracted from the J-V characteristics shown in Figure 5.8

	V_{OC} (mV)	J_{SC} (mA cm^{-2})	FF (%)	η (%)
7 wt% sFPA	499	- 0.47	61	0.14
2 wt% sFPA	477	- 0.69	63	0.20
1 wt% sFPA	475	- 0.77	64	0.23

vice. If these injected charges, (i.e., polarons) recombine radiatively the device works as a LED.[254] The higher the slope of the diode characteristic in forward direction, the higher is the polaron recombination yield (radiative and non-radiative) in the device. The diode dark current characteristics shown in Figure 5.7b mirror a direct correlation between polaron recombination and an enhancement in interfacial donor-acceptor area due to the NIL process. It has to be stressed that the difference in device performance is not induced by the NIL process itself, but by the effectively enhanced interfacial area (Figure 5.7a vs. Figure 5.8) that is maintained after the processing route (Figure 5.2). Furthermore, the direct correlation between the enhanced interfacial area and polaron recombination in forward direction appears to be insensitive on the alignment of the donor-acceptor interface (parallel or perpendicular) with respect to the external electric field. This becomes obvious considering that the projection of the interface perpendicular to the external field is identical for the flat and the nanostructured interfaces. However, it is not verified so far whether the dominant interface recombination channel is trap-assisted recombination or bimolecular recombination.[255, 256] From a theoretical point of view the EQE of a nanostructured bi-layer heterojunction solar cell can be expressed according to Equation 2.1. The measurement is performed under short-circuit condition, no charge carriers are injected through the electrodes and the photo-generated current is spectrally resolved. The EQE measurement illustrated in Figure 5.7c shows a direct correlation between donor-acceptor interfacial area and η_{EQE}. The direct relation between the spectrally resolved photo-generated current density (Figure 5.7c) and the J_{SC} (Figure 5.7a) is verified. By assuming $\eta_{\mathrm{absorption}}$ being independent of the donor-acceptor interface texturing, the enhancement in η_{EQE} can be directly addressed at an enhancement in η_{IQE}, i.e., enhanced harvesting of photoexcitons from exciton diffusion to charge carrier collection (Equation 2.1). Steady state photoluminescence (PL) measurements (Figure 5.9) show reduced radiative recombination of excitons correlated to the enhancement in donor-acceptor interfacial area. The integrated PL signal for the 35 nm and 75 nm structure relative to the flat reference structure is 84 % and 74 %, respectively when exciting P3HT at 510 nm. The relative EQE enhancement (Figure 5.7d), together with the knowledge of the complementary absorption of our model system (Figure 5.1), allows for the interpretation of the fundamental processes of exciton separation that exclusively occurs at the nanostructured P(NDI2OD-T2):P3HT heterojunction. The relative EQE enhancement is wavelength independent, all three absorption features the characteristic P(NDI2OD-T2) (at around 400 nm and 700 nm) and the P3HT (at around 550 nm) equally contribute and directly correlate with the enhancement in interfacial area. Enhanced photoexciton harvesting, originating from both P(NDI2OD-T2) and P3HT, contribute to the enhancement in η_{EQE} (Figure 5.7c) and consequently to the increased J_{SC} shown in Figure 5.7a. The J_{SC} (Table 5.2) for the 75 nm and 35 nm device is 35 % and 24 % higher than for the flat reference device, respectively. This is consistent with the measured 26 % and 16 % lower photoluminescence signal (Figure 5.9) with respect to the flat interface sample. When directly comparing the 75 nm and 35 nm devices, a surface enhancement of 36 % (Figure 5.4) enhances the overall PL quenching by 11 % and the J_{SC} by 9 %.

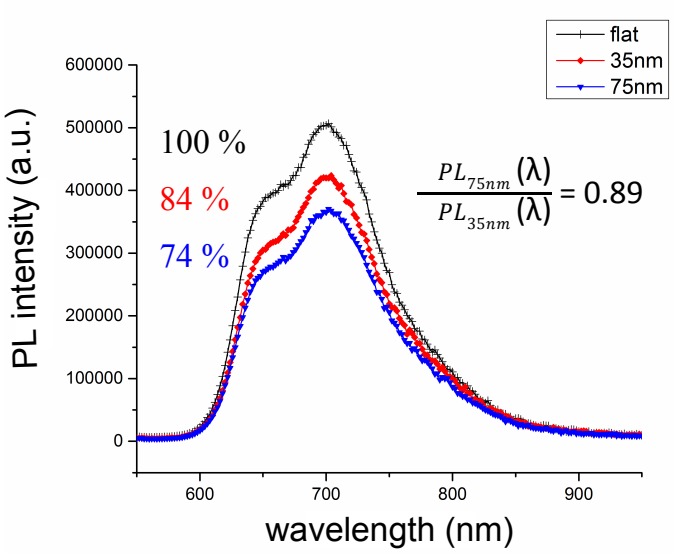

Figure 5.9.: Steady state photoluminescence measurement of nanostructured bi-layer P(NDI2OD-T2):P3HT samples. By increasing the donor-acceptor interfacial area, the radiative recombination yield of photoexcitons is reduced, i.e., excitons are more efficient separated. The quenching behavior with respect to the enhanced interface is investigated by exciting P3HT at 510 nm. Adapted with permission from Pfadler et al.[18] Copyright (2014) American Chemical Society.

Transient Photovoltage and Impedance Spectroscopy Measurements. The results of the transient photovoltage (TPV) measurements are shown in Figure 5.10. The technique allows for the investigation of the influence of the enhanced donor-acceptor interfacial area on polaron recombination kinetics directly in the time domain. A schematic illustration of the measurement technique is given in Figure 5.10a. Devices are illuminated using a 100 mW cm^{-2} AM 1.5G solar simulator ("light biased") and a quasi-open circuit condition is established by suppressing a net current flow in the electrical circuit due to the 1 MΩ termination resistance of the oscilloscope.[109] A laser pulse (Figure 5.10a) introduces a small optical perturbation, polarons are generated, and the disturbed system is simultaneously forced to equilibrate since additionally generated polarons recombine in the active layer of the device due to the high termination resistance, which does not allow charge collection via the external electrodes. Time resolved polaron recombination is determined by monitoring the TPV decay rate with an oscilloscope. The results of the polaron recombination kinetics are plotted in Figure 5.10b. The inset summarizes the mono-exponential fit to the extracted polaron decay kinetics (with the recombination rate (k) as a fit parameter). The inverse value of the estimated k is denoted as the polaron lifetime (τ).[257] Results of the TPV measurements are summarized in Table 5.4. By increasing the donor-acceptor interfacial area, the corresponding polaron lifetime under quasi-open circuit condition is decreased from 13.0 μs (flat reference), over 11.6 μs (35 nm structure) to 9.98 μs (75 nm structure). The con-

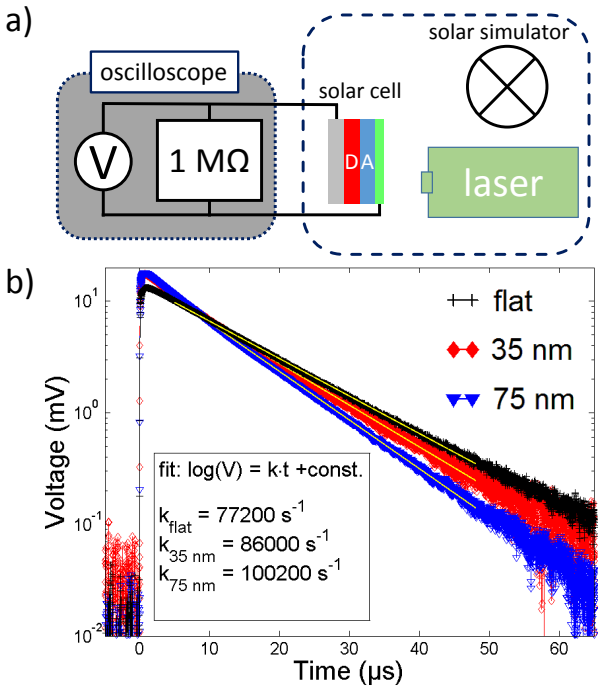

Figure 5.10.: (a) Schematic illustration of the TPV set-up. Devices are "light-biased" using a 100 mW cm^{-2} AM 1.5G solar simulator, a small optical perturbation is introduced (532 nm laser pulse) and subsequent polaron recombination kinetics back to equilibrium is monitored with an oscilloscope. **(b)** TPV measurements correlated with an enhancement in donor-acceptor interfacial area. The inset summarizes the results of the mono-exponential fits. Adapted with permission from Pfadler et al.[18] Copyright (2014) American Chemical Society.

trolled enhancement in interfacial area causes increased polaron recombination rates which consistently outbalance the increased charge carrier generation rates under open circuit condition, where there is no net current generation.[258] Impedance spectroscopy gives experimental access to characterize our model system under working conditions. The bias region around the maximum power point is of greatest interest, since all dynamic excitonic and polaronic processes - generation, transport and recombination contribute to the overall device performance. For this purpose, devices are illuminated and the frequency dependent impedance is recorded for a range of DC applied biases that cover the power generation regime of the nanostructured bi-layer devices. A cole-cole plot (Figure 5.11a) is a complex plane representation of the imaginary (Z") and the real part (Z') of the impedance response. The measurement conditions and a representative cole-cole plot are summarized in Figure 5.11. The equivalent circuit (Figure 5.11b) that is used to fit (solid lines in Figure 5.11a) the experimental data needs to be highlighted, since the dependency of donor-acceptor interfacial area on recombination kinetics is based on discussing the electrical components of this circuit (Figure 5.12). The simple equivalent circuit shown in Figure 5.11b that is used to model the acquired data consists of a resistor (R_s) in series with a geometrical capacitor (C_{geo}), a resistor (R_p), and

Table 5.4.: Fitted TPV decay rates k and corresponding ($\tau \equiv k^{-1}$) polaron lifetimes τ. The measurement is shown in Figure 5.10

	k(s^{-1})	$\tau(\mu s)$
flat	77200	13.0
35 nm	86000	11.6
75 nm	100200	9.98

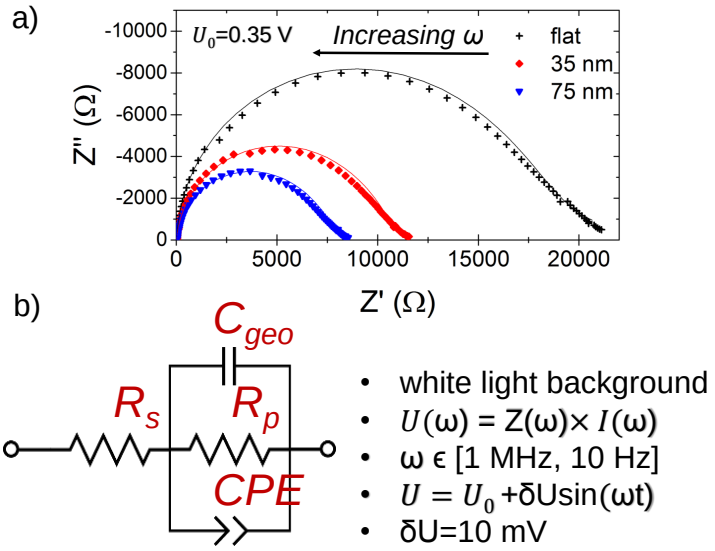

Figure 5.11.: Impedance spectroscopy (IS) on nanostructured all-polymer devices. The geometrical capacitance C_{geo} **(a)** in parallel with the recombination resistance R_p **(b)**. The geometrical capacitance is essentially independent of the polymer-polymer texturing that is indicative for two important aspects: the volume of the active material is conserved and the interface structuring is not transferred to the Ag backelectrode. Adapted with permission from Pfadler et al.[18] Copyright (2014) American Chemical Society.

a constant phase element (CPE) in parallel. In general, the most fundamental model that can be applied to describe a solar cell is known to be a resistor in series with an R-C element.[112] Leever and co-workers successfully applied this simple model to an organic single-layer (P3HT) solar cell and further developed it to model P3HT:$PC_{61}BM$ BHJ devices.[259] The model we employ to describe all-polymer bi-layer devices is the simplest one extended by a CPE in parallel to the R-C element (Figure 5.11b). The additional CPE is necessary to accurately model low frequency (ω) data points shown in the cole-cole plot (Figure 5.11a). The R_s circuit element represents resistive losses due to the electric contacting and charge transport through the electrodes. The capacitor C_{geo} is determined to be a geometrical capacitor whose value is calculated by assuming the equation for a simple parallel plate capacitor. The capacitance of the three thin-

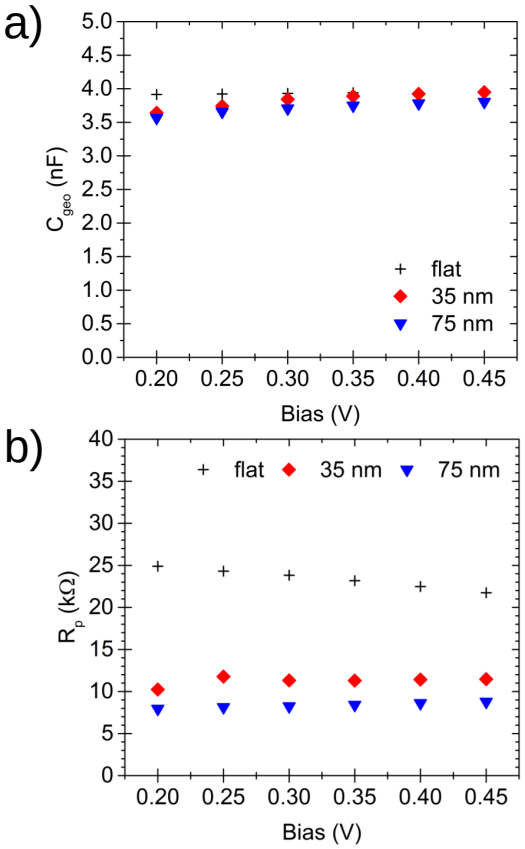

Figure 5.12.: Electrical components of the equivalent circuit that corresponds to the IS measurement summarized in Figure 5.11. The geometrical capacitance C_{geo} **(a)** in parallel with the recombination resistance R_p **(b)**. The geometrical capacitance is essentially independent of the polymer-polymer texturing that is indicative for two important aspects: the volume of the active material is conserved and the interface structuring is not transferred to the Ag backelectrode. Adapted with permission from Pfadler et al.[18] Copyright (2014) American Chemical Society.

film solar cells with different interface geometry is calculated to be 3.7 nF by taking the device area of 0.168 cm^2, the spacing between ITO and Ag (50 nm TiO_2/ 60 nm P(NDI2OD-T2) and 60 nm P3HT), a dielectric constant (ϵ) of 31 for the anatase TiO_2 and a dielectric constant (ϵ) of 3 for the organic bi-layer into account.[42, 260] Note that the geometry of the polymer-polymer interface does not influence the geometrical capacitance due to the (supposedly) identical dielectric constants in the materials. Since the nanoimprint only introduces an ordered structure to the interface but maintains the volume of both P(NDI2OD-T2) and P3HT, the combined capacitance of the polymer layer stack would not change even for differences in the dielectric constants. The calculated value of 3.7 nF coincides with the values extracted from impedance fits shown in Figure 5.12a. C_{geo} is essentially independent of both bias and polymer-polymer interface structuring that is additionally consistent with the idea of a purely geometrical

origin of this capacitor in the equivalent circuit. In correlation with the GISAXS measurements (Figure 5.5), the similarity of C_{geo} for the flat and the structured devices gives additional experimental evidence that the geometry of the Ag backelectrode is independent of the patterned bi-layer interface. The extracted key parameter of the IS measurement is the recombination resistance (R_p) that describes polaron recombination under working conditions. The recombination resistance as a function of the applied bias ranging from 0.20 V to 0.45 V covering the power generation regime (cf. Figure 5.7a) is shown for the different donor-acceptor interface patterns. As seen in the figure, the recombination resistance decreases for increasing interfacial area for all bias voltages around the maximum power point. This finding is in good accordance with the TPV results describing the situation at open circuit conditions, where polaron extraction is suppressed as well as with dark J-V measurements characterizing the polaron injection regime. The extracted polaron lifetimes from the TPV measurement under quasi open circuit conditions ranging from 13 μs to 9.98 μs are within the range of non-optimized P3HT:PC_{61}BM BHJ solar cells under working conditions varying from 7.8 μs to 22 μs that is known from literature.[259]

5.3. Conclusion

The presented synthesis strategy for all-solution processed nanostructured bi-layer solar cells allows the controlled enhancement of donor-acceptor interfacial area in all-polymer devices. This enables for the investigation of fundamental exciton separation and polaron recombination processes in a comb-like donor-acceptor architecture that has often been considered as ideal for excitonic solar cells. Our bottom-up synthesized devices feature nanopatterned donor-acceptor interfaces with very good control over the size of the employed nanostructures. Anodized aluminum oxide (AAO) membranes are used in a nanoimprint lithography (NIL) process to tailor the topography of the organic bottom layer. The nanostructured bottom layer is developed via photo-crosslinking, which allows the subsequent solution processing of the second polymer. Nanostructure topographies have been consistently characterized both locally and globally using SEM/AFM and GI-RSoXS/GISAXS, respectively. The origin of an improvement in device performance of nanostructured over flat bi-layer devices is directly correlated to the enhancement in donor-acceptor interfacial area. Furthermore, due to complementary spectral features of the employed model donor and acceptor polymers, it is possible to conclude from EQE results that exciton separation across the donor-acceptor interface due to both electron transfer to the acceptor as well as hole transfers to the donor equally contribute to a relative enhancement in photocurrent. Apart from improved exciton harvesting upon nanopatterning of the polymer-polymer interface there is significant enhancement of polaron recombination correlated to the enhanced interfacial area supposedly owing to an increased number of interface states.[90] Several complementary characterization techniques focusing on different working regimes of the solar cells were employed to investigate the influence of the interface enhancement. Dark diode current characteristics show an enhanced recombination yield of injected polarons that has strong impact on the shape of the J-V characteristics. Additionally,

the recombination of injected polarons in forward direction exclusively depends on the total interfacial area and seems to be insensitive to the interface alignment with respect to the external electric field. TPV measurements consistently show that enhanced polaron generation rates are outbalanced by enhanced polaron recombination rates at the V_{OC}. Increased recombination is not only found in forward bias and at open circuit voltage, but under solar cell working conditions around the maximum power point as inferred from impedance spectroscopy results. According to the findings of Mandoc and co-workers who investigated recombination mechanisms in all-polymer BHJ devices, we assume that the dominant recombination mechanism (at 1 sun) in our system is bimolecular recombination.[255] However, a detailed study of light intensity dependent current-voltage curves, which was not in the scope of this fundamental study, could give access to the exact order of the recombination. The investigation of our model system shows that polaron recombination not only limits the efficiency of BHJ solar cells, but limits the efficiency of well-ordered heterostructure devices as well.[112] In efficient polymer-fullerene BHJ solar cells the issue of interface recombination is partly solved due to different phases (amorphous and crystalline, mixed and pure phases).[261] As discussed by Jamieson and co-workers pure crystalline fullerene domains can act as energetic sinks for photogenerated charge carriers, which allow efficient charge collection and hinder polaron recombination.[262] This in combination with our findings

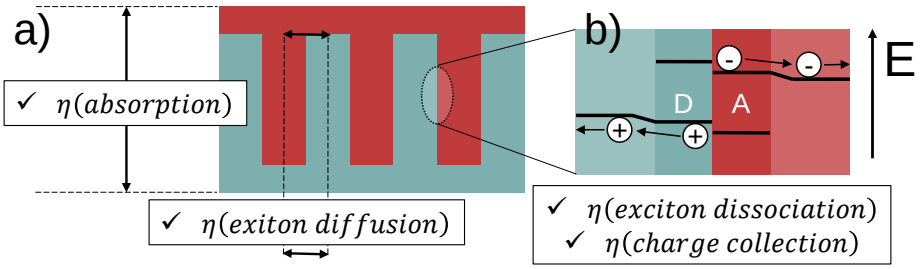

Figure 5.13.: Illustration of the perfect comb-like morphology for a high efficiency excitonic solar cell (Equation 2.1). A vertically optimized spacing guarantees optimized $\eta_{absorption}$, whereas a horizontal spacing of the donor-acceptor interfaces with respect to the exciton diffusion length guarantees optimized $\eta_{exciton\ diffusion}$. Beside the bi-continuous spatial optimization **(a)**, the perfect morphology needs to be energetically optimized **(b)**. In the ideal energy landscape both holes and electrons are funneled away from the interface immediately after exciton splitting through slight steps in the HOMO and LUMO levels of donor and acceptor, respectively. This can for instance be realized via changes in the local crystallinity or different phases as discussed by Jamieson and Burke and co-workers for polymer-fullerene bulk heterojunctions.[261, 262]. Adapted with permission from Pfadler et al.[18] Copyright (2014) American Chemical Society.

implies that the often postulated ideal comb-like donor-acceptor morphology is indeed spatially optimized (Figure 5.13a) in terms of absorption, exciton diffusion, and direct charge percolation pathways towards the external electrodes, but the proposed ideal morphology ignored the energy landscape (Figure 5.13b) which has the potential to limit recombination. Therefore, a perfect morphology for an excitonic solar cell is a

multiphase (or multilayer) system as discussed by Burke et al. but includes the spatial arrangement, i.e., a comb-like geometry (Figure 5.13).[261]

6. Conclusion and Outlook

It was the aim of this dissertation to find and to further develop approaches to manipulate thin-film solar cells in a highly controlled manner, such that structure-induced influences can be both micro- and macroscopically investigated in parallel. Different up-scalable nanotechnological strategies were embarked to manipulate optoelectronic device properties of organic thin-film solar cells and to provide better understanding regarding the limits in efficiency of organic thin-film devices.
In general, materials with the right stoichiometry need to be combined in a functionally aligned material stack to fulfill basic requirements of solar cells – a photoactive material to generate charge carriers upon light absorption which needs to be embedded in an environment that provides an asymmetric resistance for electrons and holes to be finally collected at different electrodes. If an organic semiconductor is used as photoactive material, the underlying device physics is typically described within the framework of excitonic (cf. section 2) solar cells. The binding energy of coulombically bound electron-hole pairs (i.e., excitons) in this class of solar cells cannot be thermally overcome and these *Frenkel* type excitons need to be separated with help of the electrochemical driving force given at a type II heterojunction. Asymmetric exciton dissociation at a type II organic-organic heterojunction for instance exclusively leads to increased majority charge densities in the p-type and n-type semiconductor. The limiting factor of this class of solar cells is the so-called exciton bottleneck, i.e., the typically relatively long optical absorption length which is one order of magnitude larger than the typical length scale for exciton diffusion ($L_D \approx 10\ nm$). This limitation determines the spatial arrangement of n-type/p-type material phases to be on the order of L_D to be highly efficient in terms of exciton harvesting. Direct percolation pathways for electron and hole polarons to the respective electrodes in addition to the efficiency of exciton harvesting determine the electronic properties of the photoactive film reflected in the internal quantum efficiency (IQE). Highest efficiencies in organic single absorber layer devices are based on the so-called bulk heterojunction (BHJ) concept, which morphologically features a spontaneous phase separated interpenetrating n-type/p-type nanonetwork. Optimized BHJ solar cells obtain IQEs close to unity at typical layer thicknesses of 100 nm, but suffer from incomplete light absorption.
The first part of this dissertation focused on different approaches to enhance the absorption of the photoactive material by changing the surrounding optical cavity at optimized electronic conditions. The second part focused on enhanced IQEs by artificially changing the spatial arrangement of the photoactive material at fixed conditions of the optical cavity.
First, the coherent electric-field distribution in (flat interfaces) 1D photonic multilayer solar cells was investigated (cf. section 4.1) both by experiment and simulation. There-

fore the transparent indium tin oxide (ITO) electrode was replaced and further compared to a novel high-performance and temperature-stable TiO_2/Ag/TiO_2 (TAT) multilayer electrode. Such a multilayer electrode allows a decoupled optimization of the absorption and photoexciton conversion processes with respect to the employed photoactive material. A transfer-matrix algorithm was used to computationally maximize the photocurrent generation in the active medium of BHJ solar cells featuring a 1D photonic device configuration. The photocurrent maximization has been accessible by maximizing the electric field intensity in the active material by varying the geometry of the TAT multilayer electrode, thereby tuning the occurrence of coherent *Fabry-Perot* cavity modes. High-performing organic photovoltaics (OPVs) exhibiting state-of-the-art efficiencies were achieved with PTB7:PC_{71}BM BHJ devices using a TAT multilayer electrode as replacement for ITO. The TAT multilayers show a superior thermal stability than ITO making them viable for application in other photovoltaic systems like dye-sensitized solar cells and perovskite solar cells. As outlined by a combination of experiments and optical simulation it was possible to tune the electric field intensity inside the device by adjusting the thickness of the TAT layer, and as a consequence the properties of the optical cavity. The results show that in particular the front (or bottom) TiO_2 layer can be tuned in thickness without changing the electronic properties of the TAT electrode, which allows the tailored optimization of device performance for arbitrary active layer compositions and thicknesses.
Second, periodically structured TiO_2 electrodes were introduced to thin-film photovoltaics to tackle the typically present partial light absorption. Arising consequences on light management in such thin-film solar cells featuring a 2D photonic structure were elucidated. Wavelength-scale patterns were transferred to the electron-selective TiO_2 bottom electrodes via direct laser interference patterning (DLIP). In the main absorption region (cf. section 4.2.2) of the employed photoactive materials, the efficiency of the structure-induced light in-coupling has been spectroscopically shown to be determined by the refractive index n(active material) with respect to $n(TiO_2)$. Two different representative thin-film solar cell architectures were investigated: an organic solar cell featuring a P3HT:PC_{61}BM BHJ as active material, and a hybrid solar cell with Sb_2S_3 as inorganic active material. These served as model systems for low n and high n thin-film absorbers. A quantitative spectroscopic examination shows an asymmetry in absorption enhancement for the two solar cell architectures. The implementation of a wavelength-scale pattern was beneficial for the total absorption enhancement in case of an active material of higher n was deposited on the structure, but detrimental for the absorption in case of a low n material was deposited on top. The refractive indices of the single materials were determined with spectroscopic ellipsometry and the *Fresnel* formalism was used to understand and to visualize the asymmetry in refractive index and correspondingly the asymmetry in light-coupling. These findings outline that considerations based on the macroscopic *Fresnel* equations enable a qualitative understanding of light-coupling at nanostructured electrode/active layer interfaces which feature a wavelength-scale pitch. This provides an easy way to assess the potential of a functional nanostructure for light absorption enhancement in thin-film solar cells.
Beside the elucidation of light in-coupling in the main absorption region of the photoactive material, structure-induced light-trapping effects (cf. section 4.2.3) target-

ing at a resonant enhancement of the very weak tail-state absorption present in polymer:fullerene BHJ solar cells were additionally investigated. The study illustrates how resonant absorption enhancement in a common OPV material system can be achieved using a rapid texturing technique like DLIP. Experimental findings of increasing tail state absorption and EQE were supported by numerical simulations which further show the tuneability of the absorption resonances towards arbitrary wavelength regions in the UV-Vis and NIR. Fully vectorial electromagnetic simulations using the Discontinuous Galerkin Time Domain (DGTD) method were performed to obtain time-averaged Poynting vectors along with spatially resolved dependencies of the power loss densities. Possibilities are identified to precisely design the absorption properties of an OPV using a fully roll-to-roll compatible fabrication technique as a potential pathway towards absorption edge-enhanced OPVs. It might further be possible to resonantly enhance the typically very weak absorption of charge transfer states which could close the gap between net optical and electric band gap of OPVs. Future studies on absorption edge-enhanced low-dielectric polymer:fullerene devices should additionally include a maximization of light-coupling in the main absorption region, e.g., by replacing TiO_2 with periodically structured low-dielectric PEDOT:PSS in a non-inverted device configuration. Furthermore, future studies could focus on the implementation of not only one lateral periodicity, but several ones to obtain hierarchical structures in different lateral directions in order to acquire broadband tail-state absorption in OPVs.

Electronic manipulation in terms of the macroscopic device performance of organic solar cells was obtained by artificially controlling the (n-type/p-type) donor-acceptor interfacial geometry on a nanometer scale. Comb-like bilayer all-polymer morphologies (cf. section 5) featuring a controlled enhancement in donor–acceptor interfacial area were experimentally realized. This allows for a systematic investigation of fundamental exciton separation and polaron recombination processes in a comb-like donor-acceptor architecture that has often been considered as ideal for excitonic solar cells. The bottom-up synthesized devices feature nanopatterned donor-acceptor interfaces with very good control over the size of the employed nanostructures. Anodized aluminum oxide membranes were used in a nanoimprint lithography process to tailor the topography of the organic bottom layer. The nanostructured bottom layer was developed via photo-crosslinking which allows the subsequent solution processing of the second polymer. Nanostructure topographies have been consistently characterized both locally and globally using SEM/AFM and GI-RSoXS/GISAXS, respectively. The origin of an improvement in device performance of nanostructured over flat bilayer devices was directly correlated to the enhancement in donor-acceptor interfacial area. Furthermore, due to complementary spectral features of the employed model donor and acceptor polymers it was possible to conclude from EQE results that exciton separation across the donor-acceptor interface due to both electron transfer to the acceptor as well as hole transfers to the donor equally contribute to a relative enhancement in photocurrent. Apart from improved exciton harvesting upon nanopatterning of the polymer-polymer interface there was significant enhancement of polaron recombination correlated to the enhanced interfacial area. Several complementary characterization

techniques focusing on different working regimes of the solar cells were employed to investigate the influence of the interface enhancement. Dark diode current characteristics showed an enhanced recombination yield of injected polarons that had strong impact on the shape of the J-V characteristics. Additionally, the recombination of injected polarons in forward direction exclusively depends on the total interfacial area and seems to be insensitive to the interface alignment with respect to the external electric field. Transient photovoltage measurements consistently show that enhanced polaron generation rates were outbalanced by enhanced polaron recombination rates at the V_{OC}. Increased recombination was not only found in forward bias and at open circuit voltage, but also under solar cell working conditions around the maximum power point as inferred from impedance spectroscopy results. According to the findings of Mandoc and co-workers, who investigated recombination mechanisms in all-polymer BHJ devices, it is assumed that the dominant recombination mechanism (at 1 sun) in such a system is bi-molecular recombination.[255] However, a detailed study of light intensity dependent current-voltage curves could give access to the exact order of the recombination. The investigation of the model system showed that polaron recombination not only limits the efficiency of BHJ solar cells, but limits the efficiency of well-ordered heterostructure devices as well.[112] In efficient polymer-fullerene BHJ solar cells the issue of interface recombination is partly solved due to different phases (amorphous and crystalline, mixed and pure phases).[261] As discussed by Jamieson and co-workers pure crystalline fullerene domains can act as energetic sinks for photogenerated charge carriers which allow efficient charge collection and hinder polaron recombination.[262] This in combination with our findings implies that the often postulated ideal comb-like donor-acceptor morphology is indeed spatially optimized in terms of absorption, exciton diffusion, and direct charge percolation pathways towards the external electrodes, but the proposed ideal morphology ignored the energy landscape which potentially limits recombination. Therefore, a perfect morphology for an excitonic solar cell is a multiphase (or multilayer) system as discussed by Burke et al. but includes the spatial arrangement, i.e., a comb-like geometry.[261]

A. Appendix to section 4.1.2

The following data corresponds to section 4.1, which is based on the research paper *Decoupling Optical and Electronic Optimization of Organic Solar Cells using High-Performance Temperature-Stable $TiO_2/Ag/TiO_2$ Electrodes* which was written as part of my Ph.D.[153] All experiments and measurements for this study were performed by *Dr. Kwang-Dea Kim*. I designed the project, helped with simulations and interpretation of the data and wrote most parts of the manuscript.

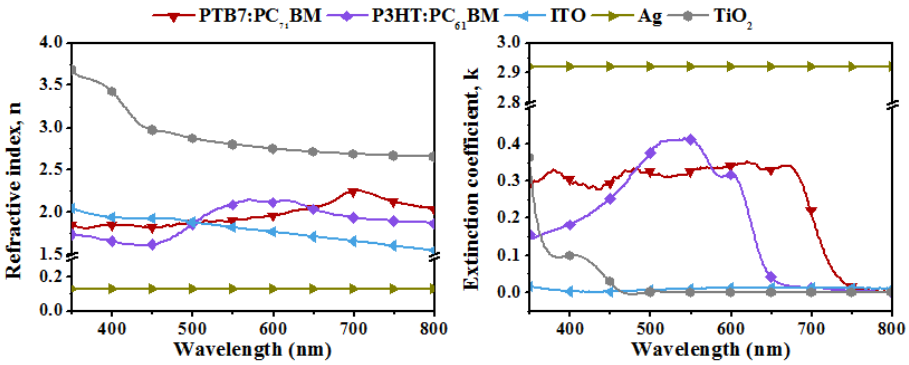

Figure A1.: (a) Refractive indices n and (b) extinction coefficients k of used materials PTB7:PC_{71}BM, P3HT:PC_{61}BM, ITO, Ag, and TiO_2. Values for ITO, P3HT:PC_{61}BM and Ag have been taken from the database of the simulation software, and values of anatase TiO_2, and PTB7:PC_{71}BM were taken from literature.[124, 140, 263] Reprinted with permission from Kim and Pfadler et al.[153] Copyright (2015), AIP Publishing LLC.

Table A1.: Characteristic solar cell parameters recorded under simulated AM 1.5G solar irradiance of devices featuring different electrodes. The values corresponds to J-V characteristics disscussed in Figure 4.6. Averaged performance of device for T/ITO and TAT with different thickness of the bottom-TiO_2 (5, 10, 28, 40 and 55 nm).

Device	V_{OC} (mV)	J_{SC} (mA $\cdot$ cm^{-2})	FF (%)	η (%) Average/Best
ITO	0.74±0.01	- 15.43±0.35	62.5±1.6	7.13±0.25 / 7.50
ITO free/ $T_{bottom\text{-}TiO_2}$				
5 nm	0.74±0.01	- 17.08±0.22	62.5±1.5	7.86±0.20 / 8.09
10 nm	0.74±0.01	- 16.89±0.23	62.5±1.5	7.81±0.19 / 8.05
28 nm	0.75±0.01	- 17.78±0.31	63.5±1.8	8.45±0.19 / 8.73
40 nm	0.74±0.01	- 16.30±0.28	60.2±2.5	7.26±0.46 / 7.82
55 nm	0.72±0.04	- 15.49±0.80	52.1±4.1	5.84±0.83 / 7.01

B. Appendix to section 4.2.2

The following data corresponds to section 4.2.2, which is based on the research paper *A comparison of light-coupling into high and low index nanostructured photovoltaic thin films* which I have written as part of my Ph.D.[106] For this study I fabricated all solar cells and absorption samples for data shown in the publication. I wrote the manuscript and was responsible for editing.

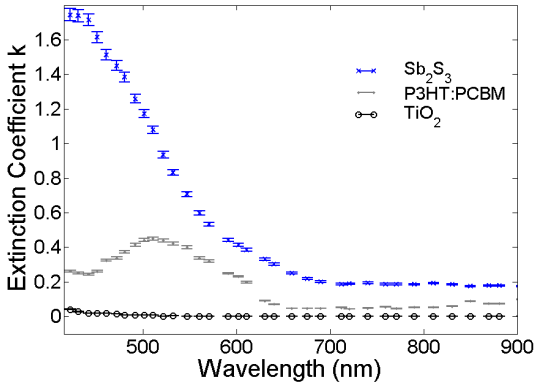

Figure B1.: Spectroscopic ellipsometry is employed to determine the extinction k of pure Sb_2S_3, TiO_2, and P3HT:$PC_{61}BM$, respectively. The corresponding refractive indices are shown in Figure 4.10a. Reprinted with permission from Pfadler et al.[106] Copyright (2015), AIP Publishing LLC.

C. Appendix to section 4.2.3

The following data corresponds to section 4.2.3 and is based on the research paper *Structure-induced Resonant Tail-State Absorption in Polymer:Fullerene Bulk-Heterojunction Solar Cells* which I have written as part of my Ph.D.[133] For this study I fabricated all solar cells and absorption samples for data shown in the publication. Direct laser interference patterning (DLIP) was realized with the help of *M. Stärk* (cf. section 3.3) and full-vectorial electromagnetic simulations (cf. section 3.4) were performed in collaboration with *T. Kiel* and co-workers. I wrote the manuscripts and was responsible for editing.

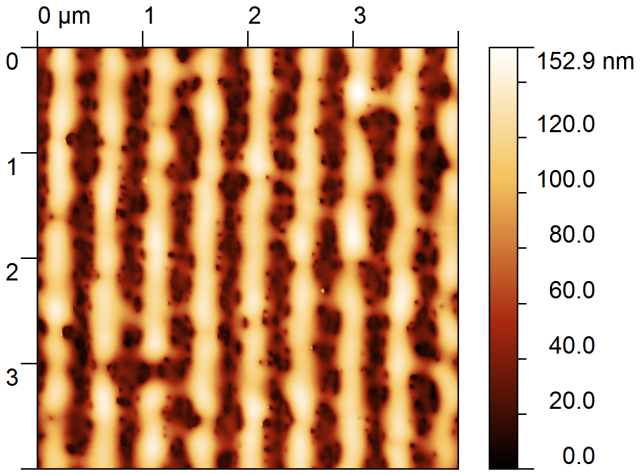

Figure C1.: AFM topographic height profile of laser patterned TiO_2. The structure features a periodicity of 470 nm. A corresponding statistically averaged line profile is shown in Figure 4.12a. Adapted from Pfadler et al.[133]

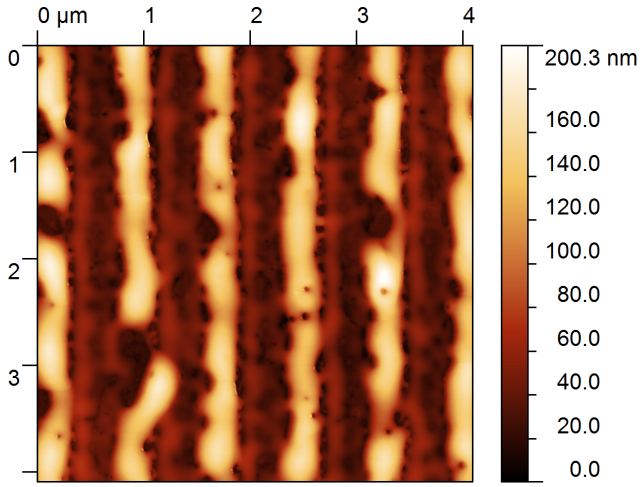

Figure C2.: AFM topographic height profile of laser patterned TiO_2. The structure features a periodicity of 800 nm. A corresponding statistically averaged line profile is shown in Figure 4.12b. Adapted from Pfadler et al.[133]

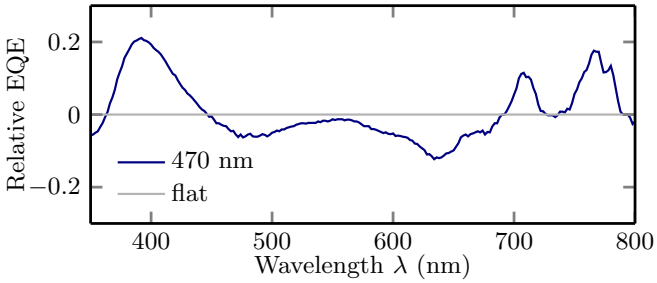

Figure C3.: Statistical independent second data set on structured P3HT:PCBM BHJ. Relative EQE of a device featuring a laser patterned $Ti0_2$ bottom electrode. Adapted from Pfadler et al.[133]

Table C1.: JV-characteristic of a statistical independent second data set on structured P3HT:PCBM BHJ. JV parameters corresponding to the second statistical independent data set shown in Figure C3 and Figure C4.

	J_{SC} (mA · cm^{-2})	V_{OC} (mV)	FF (%)	η (%)
470 nm	-7.0	0.57	59	2.3
flat	-7.2	0.55	58	2.3

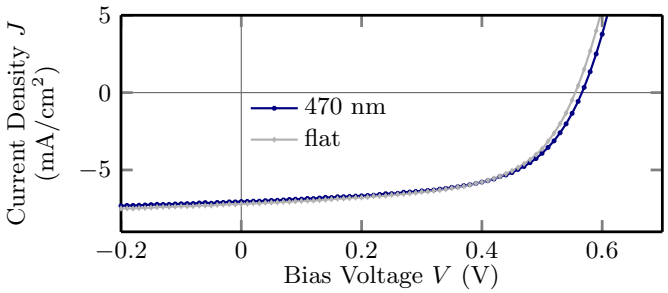

Figure C4.: JV-characteristic of a statistical independent second data set on structured P3HT:PCBM BHJ. JV-characteristic are recorded under simulated AM1.5G conditions. The corresponding relative EQE is shown in figure C3 and summarized in table C1. Adapted from Pfadler et al.[133]

D. Appendix to section 5

The following data corresponds to section 5, which is based on the research paper *Influence of interfacial area on exciton separation and polaron recombination in nanostructured bilayer all-polymer solar cells* which I have written as part of my Ph.D.[18] For this study I fabricated all solar cells and did most of the measurements for data shown in the publication. *M. Coric* did initial experiments and solar cell characterization. I wrote the manuscript and was responsible for editing.

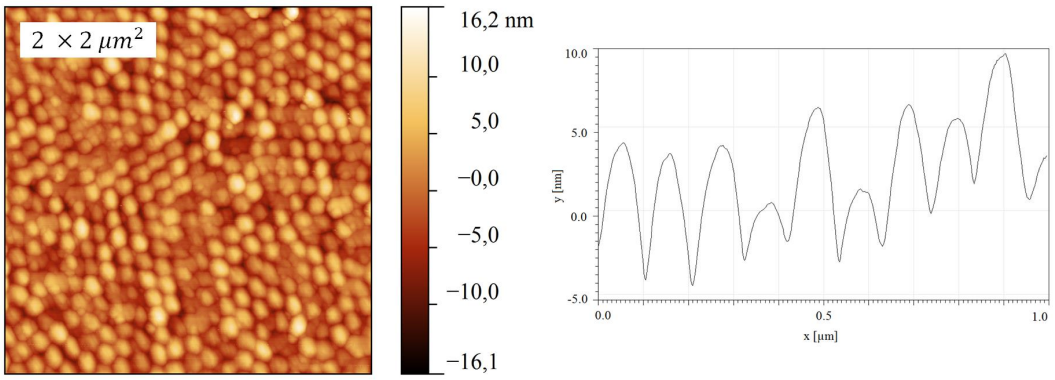

Figure D1.: AFM topographic height profile and a representative line-section. The structure is exemplarily shown and corresponds to the 75 nm structure (Figure 5.2e) after solvent wash. The structure after solvent wash underestimates the final interdigitating P(NDI2OD-T2):P3HT interface since the P3HT prevents the nanocolumns from contracting when the solvent evaporates. Adapted with permission from Pfadler et al.[18] Copyright (2014) American Chemical Society.

Bibliography

[1] W.A. Goddard III, D. Brenner, S.E. Lyshevski, and G.J. Iafrate. *Handbook of nanoscience, engineering, and technology*. CRC press, 2007.

[2] D. Bhattacharyya, S. Singh, N. Satnalika, A. Khandelwal, and S.-H. Jeon. Nanotechnology, big things from a tiny world: a review. *Nanotechnology*, 2(3), 2009.

[3] N. Taniguchi et al. On the basic concept of nanotechnology. In *Proc. Intl. Conf. Prod. Eng. Tokyo, Part II, Japan Society of Precision Engineering*, pages 18–23, 1974.

[4] K.E. Drexler and M. Minsky. *Engines of creation*. Fourth Estate London, 1990.

[5] R.P. Feynman. There's plenty of room at the bottom. *Engineering and Science*, 23(5):22–36, 1960.

[6] D. McMullan. Scanning electron microscopy 1928–1965. *Scanning*, 17(3):175–185, 1995.

[7] G.K. Binnig. Atomic force microscope and method for imaging surfaces with atomic resolution, October 16 1990. US Patent RE33,387.

[8] G. Binnig, C.F. Quate, and C. Gerber. Atomic force microscope. *Physical Review Letters*, 56(9):930, 1986.

[9] W.F. Brinkman, D.E. Haggan, and W.W. Troutman. A history of the invention of the transistor and where it will lead us. *Solid-State Circuits, IEEE Journal of*, 32(12):1858–1865, 1997.

[10] M.A. Green, K. Emery, Y. Hishikawa, W. Warta, and E.D. Dunlop. Solar cell efficiency tables (version 45). *Progress in Photovoltaics: Research and Applications*, 23(1):1–9, 2015.

[11] R.M. Swanson. Photovoltaics power up. *Science*, 324(5929):891–892, 2009.

[12] B. O'regan and M. Grätzel. A low-cost, high-efficiency solar cell based on dye-sensitized colloidal tio2 films. *Nature*, 353(6346):737–740, 1991.

[13] UN Resolution A/RES/68/221. `http://www.light2015.org/Home/About.html`. Accessed: 2015-18-08.

[14] G. Clayden, W. Warren, N. Greeves, and P. Wothers. Organic chemistry, 2001.

[15] H. Shirakawa, E.J Louis, A.G. MacDiarmid, C.K. Chiang, and A.J. Heeger. Synthesis of electrically conducting organic polymers: halogen derivatives of polyacetylene,(ch) x. *Journal of the Chemical Society, Chemical Communications*, (16):578–580, 1977.

[16] C.K. Chiang, C.R. Fincher Jr, Y.W. Park, A.J. Heeger, H. Shirakawa, E.J. Louis, S.C. Gau, and A.G. MacDiarmid. Electrical conductivity in doped polyacetylene. *Physical Review Letters*, 39(17):1098, 1977.

[17] W.P. Su, J.R. Schrieffer, and A.J. Heeger. Solitons in polyacetylene. *Physical Review Letters*, 42(25):1698, 1979.

[18] T. Pfadler, M. Coric, C.M. Palumbiny, A.C. Jakowetz, K.P. Strunk, J.A. Dorman, P. Ehrenreich, C. Wang, A. Hexemer, R.Q. Png, P.K. Ho, P. Müller-Buschbaum, J. Weickert, and L. Schmidt-Mende. Influence of interfacial area on exciton separation and polaron recombination in nanostructured bilayer all-polymer solar cells. *ACS Nano*, 8(12):12397–409, 2014.

[19] B.A. Gregg. Excitonic solar cells. *The Journal of Physical Chemistry B*, 107(20):4688–4698, 2003.

[20] J. Singh. *Electronic and optoelectronic properties of semiconductor structures*. Cambridge University Press, 2003.

[21] M. Knupfer. Exciton binding energies in organic semiconductors. *Applied Physics A*, 77(5):623–626, 2003.

[22] C.W. Tang. Two-layer organic photovoltaic cell. *Applied Physics Letters*, 48(2):183–185, 1986.

[23] G. Yu, J. Gao, J.C. Hummelen, F. Wudl, and A.J. Heeger. Polymer photovoltaic cells: enhanced efficiencies via a network of internal donor-acceptor heterojunctions. *Science-AAAS-Weekly Paper Edition*, 270(5243):1789–1790, 1995.

[24] G. Yu and A.J. Heeger. Charge separation and photovoltaic conversion in polymer composites with internal donor/acceptor heterojunctions. *Journal of Applied Physics*, 78(7):4510–4515, 1995.

[25] J.J.M. Halls, C.A. Walsh, N.C. Greenham, E.A. Marseglia, R.H. Friend, S.C. Moratti, and A.B. Holmes. Efficient photodiodes from interpenetrating polymer networks. *Nature*, 376(6540):498–500, 1995.

[26] C.J. Brabec, N.S. Sariciftci, and J.C. Hummelen. Plastic solar cells. *Advanced Functional Materials*, 11(1):15–26, 2001.

[27] P. Peumans, A. Yakimov, and S.R. Forrest. Small molecular weight organic thin-film photodetectors and solar cells. *Journal of Applied Physics*, 93(7):3693–3723, 2003.

[28] P.E. Shaw, A. Ruseckas, and I.D.W. Samuel. Exciton diffusion measurements in poly (3-hexylthiophene). *Advanced Materials*, 20(18):3516–3520, 2008.

[29] H.C. Hesse, C. Schaffer, C. Hundschell, A. Narita, X. Feng, K. Müllen, B. Nickel, and L. Schmidt-Mende. Large polycyclic aromatic hydrocarbons for application in donor–acceptor photovoltaics. *Physica Status Solidi (a)*, 209(4):785–789, 2012.

[30] M.C. Scharber, D. Muhlbacher, M. Koppe, P. Denk, C. Waldauf, A.J. Heeger, and C.J. Brabec. Design rules for donors in bulk-heterojunction solar cells-towards 10% energy-conversion efficiency. *Advanced Materials*, 18(6):789, 2006.

[31] Y. Liang, Z. Xu, J. Xia, S.-T. Tsai, Y. Wu, G. Li, C. Ray, and L. Yu. For the bright future—bulk heterojunction polymer solar cells with power conversion efficiency of 7.4%. *Advanced Materials*, 22(20):E135–E138, 2010.

[32] G. Dennler, M.C. Scharber, C.J. Brabec, et al. Polymer-fullerene bulk-heterojunction solar cells. *Advanced Materials*, 21(13):1323–1338, 2009.

[33] R.-Q. Png, P.-J. Chia, J.-C. Tang, B. Liu, S. Sivaramakrishnan, M. Zhou, S.-H. Khong, H. S. O. Chan, J.H. Burroughes, L.-L. Chua, R.H. Friend, and P.K.H. Ho. High-performance polymer semiconducting heterostructure devices by nitrene-mediated photocrosslinking of alkyl side chains. *Nature Materials*, 9(2):152–158, 2010.

[34] B. Liu, R.-Q. Png, L.-H. Zhao, L.-L. Chua, R.H. Friend, and P.K.H. Ho. High internal quantum efficiency in fullerene solar cells based on crosslinked polymer donor networks. *Nature Communications*, 3:1321, 2012.

[35] S.H. Park, A. Roy, S. Beaupre, S. Cho, N. Coates, J.S. Moon, D. Moses, M. Leclerc, K. Lee, and A.J. Heeger. Bulk heterojunction solar cells with internal quantum efficiency approaching 100%. *Nature Photonics*, 3(5):297–302, 2009.

[36] C. Deibel and V. Dyakonov. Polymer-fullerene bulk heterojunction solar cells. *Reports on Progress in Physics*, 73(9), 2010.

[37] P.K. Watkins, A.B. Walker, and G.L.B. Verschoor. Dynamical Monte Carlo modelling of organic solar cells: The dependence of internal quantum efficiency on morphology. *Nano Letters*, 5(9):1814–1818, 2005.

[38] S.M. Menke and R.J. Holmes. Exciton diffusion in organic photovoltaic cells. *Energy & Environmental Science*, 7(2):499–512, 2014.

[39] M. Grundmann. *The physics of semiconductors: an introduction including devices and nanophysics*. Springer Science & Business Media, 2006.

[40] W. Shockley and H.J. Queisser. Detailed balance limit of efficiency of pn junction solar cells. *Journal of Applied Physics*, 32(3):510–519, 1961.

[41] W. Brütting. *Physics of organic semiconductors*. John Wiley & Sons, 2006.

[42] L.J.A. Koster, S.E. Shaheen, and J.C. Hummelen. Pathways to a new efficiency regime for organic solar cells. *Advanced Energy Materials*, 2(10):1246–1253, 2012.

[43] C. Piliego and M.A. Loi. Charge transfer state in highly efficient polymer–fullerene bulk heterojunction solar cells. *Journal of Materials Chemistry*, 22(10):4141–4150, 2012.

[44] K. Hasharoni, M. Keshavarz-K, A. Sastre, R. González, C. Bellavia-Lund, Y. Greenwald, T. Swager, F. Wudl, and A.J. Heeger. Near IR photoluminescence in mixed films of conjugated polymers and fullerenes. *Journal of Chemical Physics*, 107(7):2308–2312, 1997.

[45] H. Kim, J.Y. Kim, S.H. Park, K. Lee, Y. Jin, J. Kim, and H. Suh. Electroluminescence in polymer-fullerene photovoltaic cells. *Applied Physics Letters*, 86(18):–, 2005.

[46] R.Al. Marcus and N. Sutin. Electron transfers in chemistry and biology. *Biochimica et Biophysica Acta (BBA)-Reviews on Bioenergetics*, 811(3):265–322, 1985.

[47] H.Y. Fan. Infra-red absorption in semiconductors. *Reports on Progress in Physics*, 19(1):107, 1956.

[48] A. Beer. Bestimmung der absorption des rothen lichts in farbigen flüssigkeiten. *Annalen der Physik*, 162(5):78–88, 1852.

[49] J.H. Lambert. Photometria sive de mensura et gradibus luminis colorum et umbrae (augsburg, 1760). *German translation by E. Anding (Leipzig, Verlag von Wilhelm Engelmann, 1892)*, 1892.

[50] A.D. McNaught. *IUPAC Compendium of Chemical Terminology: The Gold Book.* International Union of Pure and Applied Chemistry, 2005.

[51] N.J. Turro, V. Ramamurthy, and J.C. Scaiano. *Principles of molecular photochemistry: an introduction.* University science books, 2009.

[52] O.V. Mikhnenko, P.W.M. Blom, and T.-Q. Nguyen. Exciton diffusion in organic semiconductors. *Energy & Environmental Science*, 2015.

[53] R.C. Powell and Z.G. Soos. Singlet exciton energy transfer in organic solids. *Journal of Luminescence*, 11(1):1–45, 1975.

[54] T. Főrster. 10th spiers memorial lecture. transfer mechanisms of electronic excitation. *Discussions of the Faraday Society*, 27:7–17, 1959.

[55] G.D. Scholes. Long-range resonance energy transfer in molecular systems. *Annual Review of Physical Chemistry*, 54(1):57–87, 2003.

[56] S.R. Scully, P.B. Armstrong, C. Edder, J.M. Frechet, and M.D McGehee. Long-range resonant energy transfer for enhanced exciton harvesting for organic solar cells. *Advanced Materials*, 19(19):2961, 2007.

[57] B.E. Hardin, E.T. Hoke, P.B. Armstrong, J.-H. Yum, P. Comte, T. Torres, J.M.J. Fréchet, M.K. Nazeeruddin, M. Grätzel, and M.D. McGehee. Increased light harvesting in dye-sensitized solar cells with energy relay dyes. *Nature Photonics*, 3(7):406–411, 2009.

[58] W.A. Luhman and R.J. Holmes. Investigation of energy transfer in organic photovoltaic cells and impact on exciton diffusion length measurements. *Advanced Functional Materials*, 21(4):764–771, 2011.

[59] D.L. Dexter. A theory of sensitized luminescence in solids. *The Journal of Chemical Physics*, 21(5):836–850, 1953.

[60] C.J. Bardeen. The structure and dynamics of molecular excitons. *Annual Review of Physical Chemistry*, 65(1):127–148, 2014. PMID: 24313684.

[61] A. Köhler and H. Bässler. Triplet states in organic semiconductors. *Materials Science and Engineering: R: Reports*, 66(4–6):71–109, 2009.

[62] J.-L. Brédas, D. Beljonne, V. Coropceanu, and J. Cornil. Charge-transfer and energy-transfer processes in ϕ-conjugated oligomers and polymers: a molecular picture. *Chemical Reviews*, 104(11):4971–5004, 2004. PMID: 15535639.

[63] J.A. Bjorgaard and M.E. Kose. Simulations of singlet exciton diffusion in organic semiconductors: a review. *RSC Advances*, 5:8432–8445, 2015.

[64] T.-S. Ahn, N. Wright, and C.J. Bardeen. The effects of orientational and energetic disorder on forster energy migration along a one-dimensional lattice. *Chemical Physics Letters*, 446(1):43–48, 2007.

[65] T.M. Clarke and J.R. Durrant. Charge photogeneration in organic solar cells. *Chemical Reviews*, 110(11):6736–6767, 2010.

[66] L. Schmidt-Mende and J. Weickert. *Organic and Hybrid Solar Cells*. De Gruyter, 2016.

[67] T.M. Clarke and J.R. Durrant. Charge photogeneration in organic solar cells. *Chemical Reviews*, 110(11):6736–6767, 2010.

[68] K. Pakbaz, C.H. Lee, A.J. Heeger, T.W. Hagler, and D. McBranch. Nature of the primary photoexcitations in poly (arylene-vinylenes). *Synthetic metals*, 64(2):295–306, 1994.

[69] D. Moses, J. Wang, A.J. Heeger, N. Kirova, and S. Brazovski. Singlet exciton binding energy in poly (phenylene vinylene). *Proceedings of the National Academy of Sciences*, 98(24):13496–13500, 2001.

[70] T. Offermans, P.A. van Hal, S.C.J. Meskers, M.M. Koetse, and R.A.J. Janssen. Exciplex dynamics in a blend of π-conjugated polymers with electron donating and accepting properties: Mdmo-ppv and PCnepv. *Physical Review B*, 72(4):045213, 2005.

[71] P.W.M. Blom, V.D. Mihailetchi, L.J.A. Koster, and D.E. Markov. Device physics of polymer: fullerene bulk heterojunction solar cells. *Advanced Materials*, 19(12):1551–1566, 2007.

[72] M. Hallermann, S. Haneder, and E. Da Como. Charge-transfer states in conjugated polymer/fullerene blends: Below-gap weakly bound excitons for polymer photovoltaics. *Applied Physics Letters*, 93(5):053307, 2008.

[73] B.P. Rand, D.P. Burk, and S.R. Forrest. Offset energies at organic semiconductor heterojunctions and their influence on the open-circuit voltage of thin-film solar cells. *Physical Review B*, 75(11):115327, 2007.

[74] M.A. Loi, S. Toffanin, M. Muccini, M. Forster, U. Scherf, and M. Scharber. Charge transfer excitons in bulk heterojunctions of a polyfluorene copolymer and a fullerene derivative. *Advanced Functional Materials*, 17(13):2111–2116, 2007.

[75] D. Veldman, O. Ipek, S.C.J. Meskers, J. Sweelssen, M.M. Koetse, S.C. Veenstra, J.M. Kroon, S.S. van Bavel, J. Loos, and R.A.J. Janssen. Compositional and electric field dependence of the dissociation of charge transfer excitons in alternating polyfluorene copolymer/fullerene blends. *Journal of the American Chemical Society*, 130(24):7721–7735, 2008.

[76] K. Vandewal, A. Gadisa, W.D. Oosterbaan, S. Bertho, F. Banishoeib, I. Van Severen, L. Lutsen, T.J. Cleij, D. Vanderzande, and J.V. Manca. The relation between open-circuit voltage and the onset of photocurrent generation by charge-transfer absorption in polymer: Fullerene bulk heterojunction solar cells. *Advanced Functional Materials*, 18(14):2064–2070, 2008.

[77] J.J. Benson-Smith, L. Goris, K. Vandewal, K. Haenen, J.V. Manca, D. Vanderzande, D.D.C. Bradley, and J. Nelson. Formation of a ground-state charge-transfer complex in polyfluorene//[6, 6]-phenyl-c61 Butyric acid methyl ester (PCBm) blend films and its role in the function of polymer/PCBm solar cells. *Advanced Functional Materials*, 17(3):451–457, 2007.

[78] E.R. Bittner, V. Lankevich, S. Gélinas, A. Rao, D.A. Ginger, and R.H. Friend. How disorder controls the kinetics of triplet charge recombination in semiconducting organic polymer photovoltaics. *Physical Chemistry Chemical Physics*, 16(38):20321–20328, 2014.

[79] A. Rao, P.C.Y. Chow, S. Gélinas, C.W. Schlenker, C.-Z. Li, H.-L. Yip, A.K.-Y. Jen, D.S. Ginger, and R.H. Friend. The role of spin in the kinetic control of recombination in organic photovoltaics. *Nature*, 500(7463):435–439, 2013.

[80] K. Tvingstedt, K. Vandewal, A. Gadisa, F. Zhang, J. Manca, and O. Inganas. Electroluminescence from charge transfer states in polymer solar cells. *Journal of the American Chemical Society*, 131(33):11819–11824, 2009.

[81] N. Banerji. Sub-picosecond delocalization in the excited state of conjugated homopolymers and donor–acceptor copolymers. *Journal of Materials Chemistry C*, 1(18):3052–3066, 2013.

[82] G. Grancini, M. Maiuri, D. Fazzi, H.J. Petrozza, A .and Egelhaaf, D. Brida, G. Cerullo, and G. Lanzani. Hot exciton dissociation in polymer solar cells. *Nature Materials*, 12(1):29–33, 2013.

[83] K. Vandewal, S. Albrecht, E.T. Hoke, K.R. Graham, J. Widmer, J.D. Douglas, M. Schubert, W.R. Mateker, J.T. Bloking, G.F. Burkhard, et al. Efficient charge generation by relaxed charge-transfer states at organic interfaces. *Nature Materials*, 13(1):63–68, 2014.

[84] L. Onsager. Initial recombination of ions. *Physical Review*, 54(8):554, 1938.

[85] C.L. Braun. Electric field assisted dissociation of charge transfer states as a mechanism of photocarrier production. *The Journal of Chemical Physics*, 80(9):4157–4161, 1984.

[86] M. Tachiya. Breakdown of the onsager theory of geminate ion recombination. *The Journal of Chemical Physics*, 89(11):6929–6935, 1988.

[87] R. Häusermann, E. Knapp, M. Moos, N.A. Reinke, T. Flatz, and B. Ruhstaller. Coupled optoelectronic simulation of organic bulk-heterojunction solar cells: Parameter extraction and sensitivity analysis. *Journal of Applied Physics*, 106(10):104507, 2009.

[88] C. Deibel, T. Strobel, and V. Dyakonov. Origin of the efficient polaron-pair dissociation in polymer-fullerene blends. *Physical Review Letters*, 103(3):036402, 2009.

[89] M. Hilczer and M. Tachiya. Unified theory of geminate and bulk electron-hole recombination in organic solar cells. *The Journal of Physical Chemistry C*, 114(14):6808–6813, 2010.

[90] R.A. Street, M. Schoendorf, A. Roy, and J.H. Lee. Interface state recombination in organic solar cells. *Physical Review B*, 81(20):205307, 2010.

[91] G. Lakhwani, A. Rao, and R.H. Friend. Bimolecular recombination in organic photovoltaics. *Annual Review of Physical Chemistry*, 65:557–581, 2014.

[92] D. Credgington and J.R. Durrant. Insights from transient optoelectronic analyses on the open-circuit voltage of organic solar cells. *The Journal of Physical Chemistry Letters*, 3(11):1465–1478, 2012.

[93] P.G. Le Comber and W.E. Spear. Electronic transport in amorphous silicon films. *Physical Review Letters*, 25(8):509, 1970.

[94] E.A. Schiff. Diffusion-controlled bimolecular recombination of electrons and holes in a-si: H. *Journal of Non-Crystalline Solids*, 190(1):1–8, 1995.

[95] W.B. Jackson. Role of bimolecular recombination in picosecond photoinduced absorption of hydrogenated amorphous silicon. *Philosophical Magazine Letters*, 60(6):277–282, 1989.

[96] P. Langevin. Recombinaison et mobilites des ions dans les gaz. *Annales de Chimie et de Physique*, 28(433):122, 1903.

[97] R. Kepler. Charge carrier production and mobility in anthracene crystals. *Physical Review*, 119(4):1226, 1960.

[98] R.G. Kepler and F.N. Coppage. Generation and recombination of holes and electrons in anthracene. *Physical Review*, 151(2):610, 1966.

[99] M. Silver and R. Sharma. Carrier generation and recombination in anthracene. *The Journal of Chemical Physics*, 46(2):692–696, 1967.

[100] N. Karl and G. Sommer. Field dependent losses of electrons and holes by bimolecular volume recombination in the excitation layer of anthracene single crystals studied by drift current pulses. *Physica Status Solidi (a)*, 6(1):231–241, 1971.

[101] C. Goh, R.J. Kline, M.D. McGehee, E.N. Kadnikova, and J.M.J. Fréchet. Molecular-weight-dependent mobilities in regioregular poly (3-hexyl-thiophene) diodes. *Applied Physics Letters*, 86(12):122110, 2005.

[102] A.J. Mozer and N.S. Sariciftci. Negative electric field dependence of charge carrier drift mobility in conjugated, semiconducting polymers. *Chemical Physics Letters*, 389(4):438–442, 2004.

[103] M.B. Prince. Drift mobilities in semiconductors. i. germanium. *Physical Review*, 92(3):681, 1953.

[104] V. Coropceanu, J. Cornil, D.A. da Silva Filho, Y. Olivier, R. Silbey, and J.-L. Brédas. Charge transport in organic semiconductors. *Chemical Reviews*, 107(4):926–952, 2007.

[105] H. Bässler and A. Köhler. Charge transport in organic semiconductors. In *Unimolecular and Supramolecular Electronics I*, pages 1–65. Springer, 2012.

[106] T. Pfadler, M. Stärk, E. Zimmermann, M. Putnik, J. Boneberg, J. Weickert, and L. Schmidt-Mende. A comparison of light-coupling into high and low index nanostructured photovoltaic thin films. *APL Materials*, 3(6):066101, 2015.

[107] H.J. Snaith. How should you measure your excitonic solar cells? *Energy & Environmental Science*, 5(4):6513–6520, 2012.

[108] H.C. Hesse. *Supramolecular assembly and nanoscale morphologies for organic photovoltaic devices*. PhD thesis, lmu, 2011.

[109] C.G. Shuttle, B. O'Regan, A.M. Ballantyne, J. Nelson, D.D.C. Bradley, J. De Mello, and J.R. Durrant. Experimental determination of the rate law for charge carrier decay in a polythiophene: Fullerene solar cell. *Applied Physics Letters*, 92(9):3311, 2008.

[110] T. Kirchartz, J. Bisquert, I. Mora-Sero, and G. Garcia-Belmonte. Classification of solar cells according to mechanisms of charge separation and charge collection. *Physical Chemistry Chemical Physics*, 17(6):4007–4014, 2015.

[111] F. Fabregat-Santiago, G. Garcia-Belmonte, I. Mora-Seró, and J. Bisquert. Characterization of nanostructured hybrid and organic solar cells by impedance spectroscopy. *Physical Chemistry Chemical Physics*, 13(20):9083–9118, 2011.

[112] G. Garcia-Belmonte and J. Bisquert. Open-circuit voltage limit caused by recombination through tail states in bulk heterojunction polymer-fullerene solar cells. *Applied Physics Letters*, 96(11):113301, 2010.

[113] M. Puls. Impedance spectroscopy for nanostructured solar cells. Master's thesis, lmu, 2011.

[114] E. Zimmermann. Nanostructured extremely thin absorber solar cells. Master's thesis, University of Konstanz, 2013.

[115] C.F. Klingshirn. *Semiconductor optics*. Springer Science & Business Media, 2012.

[116] H.J. Snaith and C. Ducati. Sno2-Based dye-sensitized hybrid solar cells exhibiting near unity absorbed photon-to-electron conversion efficiency. *Nano Letters*, 10(4):1259–1265, 2010.

[117] V. Mazet, C. Carteret, D. Brie, J. Idier, and B. Humbert. Background removal from spectra by designing and minimising a non-quadratic cost function. *Chemometrics and Intelligent Laboratory Systems*, 76(2):121–133, 2005.

[118] D. Tranchida, S. Piccarolo, and R.A.C. Deblieck. Some experimental issues of afm tip blind estimation: the effect of noise and resolution. *Measurement Science and Technology*, 17(10):2630, 2006.

[119] P. Markiewicz and M.C. Goh. Simulation of atomic force microscope tip–sample/sample–tip reconstruction. *Journal of Vacuum Science & Technology B*, 13(3):1115–1118, 1995.

[120] D. McMullan. Scanning electron microscopy 1928–1965. *Scanning*, 17(3):175–185, 1995.

[121] H. Tompkins and E.A. Irene. *Handbook of ellipsometry*. William Andrew, 2005.

[122] T. Pfadler, C.M. Palumbiny, P. Wojciech, H.C. Hesse, X. Feng, K. Müllen, P. Müller-Buschbaum, and L. Schmidt-Mende. *Advances in Polymer Science; Chapter: Controlled morphologies by molecular design and nano-imprint*. Springer, 2015.

[123] L.A.A. Pettersson, L.S. Roman, and O. Inganäs. Modeling photocurrent action spectra of photovoltaic devices based on organic thin films. *Journal of Applied Physics*, 86(1):487, 1999.

[124] G.F. Burkhard, E.T. Hoke, and M.D. McGehee. Accounting for interference, scattering, and electrode absorption to make accurate internal quantum efficiency measurements in organic and other thin solar cells. *Advanced Materials*, 22(30):3293–3297, 2010.

[125] F.B. George. Transfer-matrix matlab script, *http://web.stanford.edu/group/mcgehee/transfermatrix*, June 2010.

[126] S. Hunklinger. *Festkörperphysik*. Oldenbourg Verlag, 2009.

[127] E. Hecht. Hecht optics. *Addison Wesley*, 997:213–214, 1998.

[128] I. Martín-Fabiani, S. Riedel, D.R. Rueda, J. Siegel, J. Boneberg, T.A. Ezquerra, and A. Nogales. Micro- and submicrostructuring thin polymer films with two and three-beam single pulse laser interference lithography. *Langmuir*, 30(29):8973–8979, 2014.

[129] S. Riedel, M. Schmotz, P. Leiderer, and J. Boneberg. Nanostructuring of thin films by ns pulsed laser interference. *Applied Physics A*, 101(2):309–312, 2010.

[130] F. Mücklich, A. Lasagni, and C. Daniel. Laser interference metallurgy—periodic surface patterning and formation of intermetallics. *Intermetallics*, 13(3–4):437–442, 2005.

[131] M. Stärk, F. Schlickeiser, D. Nissen, B. Hebler, P. Graus, D. Hinzke, E. Scheer, P. Leiderer, M. Fonin, and M. Albrecht. Controlling the magnetic structure of co/pd thin films by direct laser interference patterning. *Nanotechnology*, 26(20):205302, 2015.

[132] S. Riedel. *Oberflächenstrukturierung mittels gepulster Laserinterferenz: Grundlagen und Anwendungen*. PhD thesis, University of Konstanz, 2012.

[133] T. Pfadler, T. Kiel, M. Stärk, J.F.M. Werra, C. Matyssek, J. Boneberg, Busch K., J. Weickert, and L. Schmidt-Mende. Structure-induced resonant tail-state absorption in polymer:fullerene bulk-heterojunction solar cells. *submitted 2015*.

[134] J.S. Hesthaven and T. Warburton. Discontinuous Galerkin methods for time-domain Maxwell's equations. *Applied Computational Electromagnetics Society Newsletter*, 19(1), 2004.

[135] J. Niegemann, M. König, K. Stannigel, and K. Busch. Higher-order time-domain methods for the analysis of nano-photonic systems. *Photonics and Nanostructures - Fundamentals and Applications*, 7(1):2–11, 2009.

[136] K. Busch, M. König, and J. Niegemann. Discontinuous Galerkin methods in nanophotonics. *Laser Photonics Review*, 5(6):773–809, 2011.

[137] A. Taflove and S.C. Hagness. *Computational Electrodynamics: The Finite-Difference Time-Domain Method*. Artech House, Boston, 2005.

[138] M. König, C. Prohm, K. Busch, and J. Niegemann. Stretched-coordinate pmls for maxwell's equations in the discontinuous galerkin time-domain method. *Optics Express*, 19(5):4618–4631, 2011.

[139] L.A.A. Pettersson, S. Ghosh, and O. Inganäs. Optical anisotropy in thin films of poly (3, 4-ethylenedioxythiophene)–poly (4-styrenesulfonate). *Organic Electronics*, 3(3):143–148, 2002.

[140] E.F. Schubert. Refractive index and extinction coefficient of materials, ITO. `http://www.ecse.rpi.edu/~schubert/Educational-resources/Materials-Refractive-index-and-extinction-coefficient.pdf`, accessed: Oct, 2014.

[141] P.B. Johnson and R.W. Christy. Optical constants of the noble metals. *Physical Review B*, 6:4370–4379, Dec 1972.

[142] SOPRA S.A. Optical constants of titanium dioxide. `http://refractiveindex.info`, accessed: Oct, 2014.

[143] J.A. Dorman, T. Pfadler, J. Weickert, and L. Schmidt-Mende. Controlled nanostructures in organic and hybrid solar cells. In *Nanotechnology for Energy Conversion and Storage*. Wiley VCH, 2015.

[144] S.Y. Chou, P.R. Krauss, and P.J. Renstrom. Imprint of sub-25 nm vias and trenches in polymers. *Applied Physics Letters*, 67(21):3114–3116, 1995.

[145] S.Y. Chou, P.R. Krauss, and P.J. Renstrom. Imprint lithography with 25-nanometer resolution. *Science*, 272(5258):85–87, 1996.

[146] L.J. Guo. Nanoimprint lithography: Methods and material requirements. *Advanced Materials*, 19(4):495–513, 2007.

[147] X. He, F. Gao, G. Tu, D. Hasko, S. Hüttner, U. Steiner, N.C. Greenham, R.H. Friend, and W.T.S. Huck. Formation of nanopatterned polymer blends in photovoltaic devices. *Nano Letters*, 10(4):1302–1307, 2010.

[148] C. Vieu, F. Carcenac, A. Pepin, Y. Chen, M. Mejias, A. Lebib, L. Manin-Ferlazzo, L. Couraud, and H. Launois. Electron beam lithography: resolution limits and applications. *Applied Surface Science*, 164(1):111–117, 2000.

[149] H. Jansen, H. Gardeniers, M. deBoer, M. Elwenspoek, and J. Fluitman. A survey on the reactive ion etching of silicon in microtechnology. *Journal of Micromechanics and Microengineering*, 6(1):14–28, 1996.

[150] W. Lee, R. Ji, U. Gosele, and K. Nielsch. Fast fabrication of long-range ordered porous alumina membranes by hard anodization. *Nature Materials*, 5(9):741–7, 2006.

[151] J.P. Rolland, E.C. Hagberg, G.M. Denison, K.R. Carter, and J.M. De Simone. High-resolution soft lithography: Enabling materials for nanotechnologies. *Angewandte Chemie*, 116(43):5920–5923, 2004.

[152] M. Beck, M. Graczyk, I. Maximov, E.L. Sarwe, T.G.I. Ling, M. Keil, and L. Montelius. Improving stamps for 10 nm level wafer scale nanoimprint lithography. *Microelectronic Engineering*, 61–62(0):441–448, 2002.

[153] K.-D. Kim, T. Pfadler, E. Zimmermann, Y. Feng, J.A. Dorman, J. Weickert, and L. Schmidt-Mende. Decoupling optical and electronic optimization of organic solar cells using high-performance temperature-stable $tio_2/ag/tio_2$ electrodes. *APL Materials*, 3(10):106105, 2015.

[154] S. Günes, H. Neugebauer, and N.S. Sariciftci. Conjugated polymer-based organic solar cells. *Chemical Reviews*, 107(4):1324–1338, 2007.

[155] J. Peet, A.J. Heeger, and G.C. Bazan. "plastic" solar cells: Self-assembly of bulk heterojunction nanomaterials by spontaneous phase separation. *Accounts of Chemical Research*, 42(11):1700–1708, 2009.

[156] G. Li, R. Zhu, and Y. Yang. Polymer solar cells. *Nature Photonics*, 6(3):153–161, 2012.

[157] Z. He, B. Xiao, F. Liu, H. Wu, Y. Yang, S. Xiao, C. Wang, T.P. Russell, and Y. Cao. Single-junction polymer solar cells with high efficiency and photovoltage. *Nature Photonics*, 9(3):174–179, 2015.

[158] J.-D. Chen, C. Cui, Y.-Q. Li, L. Zhou, Q.-D. Ou, C. Li, Y. Li, and J.-X. Tang. Single-junction polymer solar cells exceeding 10efficiency. *Advanced Materials*, 27(6):1035–1041, 2015.

[159] R.A.J. Janssen and J. Nelson. Factors limiting device efficiency in organic photovoltaics. *Advanced Materials*, 25(13):1847–1858, 2013.

[160] A. Armin, M. Velusamy, P. Wolfer, Y. Zhang, P.L. Burn, P. Meredith, and A. Pivrikas. Quantum efficiency of organic solar cells: Electro-optical cavity considerations. *ACS Photonics*, 1(3):173–181, 2014.

[161] Q.Q. Lin, A. Armin, R.C.R. Nagiri, P.L. Burn, and P. Meredith. Electro-optics of perovskite solar cells. *Nature Photonics*, 9(2):106–112, 2015.

[162] S. Loser, B. Valle, K.A. Luck, C.K. Song, G. Ogien, M.C. Hersam, K.D. Singer, and T.J. Marks. High-efficiency inverted polymer photovoltaics via spectrally tuned absorption enhancement. *Advanced Energy Materials*, 4(14), 2014.

[163] H.A. Atwater and A. Polman. Plasmonics for improved photovoltaic devices. *Nature Materials*, 9(3):205–213, 2010.

[164] E. Stratakis and E. Kymakis. Nanoparticle-based plasmonic organic photovoltaic devices. *Materials Today*, 16(4):133–146, 2013.

[165] K. Ellmer. Past achievements and future challenges in the development of optically transparent electrodes. *Nature Photonics*, 6(12):809–817, 2012.

[166] D.S. Ginley, H. Hosono, and D.C. Paine. *Handbook of transparent conductors*. Springer, New York, 2010.

[167] T. Minami. Transparent conducting oxide semiconductors for transparent electrodes. *Semiconductor Science and Technology*, 20(4):S35–S44, 2005.

[168] D. Angmo and F.C. Krebs. Flexible ito-free polymer solar cells. *Journal of Applied Polymer Science*, 129(1):1–14, 2013.

[169] C.J.M. Emmott, A. Urbina, and J. Nelson. Environmental and economic assessment of ito-free electrodes for organic solar cells. *Solar Energy Materials and Solar Cells*, 97(0):14–21, 2012.

[170] T. Kawashima, T. Ezure, K. Okada, H. Matsui, K. Goto, and N. Tanabe. Fto/ito double-layered transparent conductive oxide for dye-sensitized solar cells. *Journal of Photochemistry and Photobiology A: Chemistry*, 164(1–3):199–202, 2004.

[171] F. Bonaccorso, Z. Sun, T. Hasan, and A.C. Ferrari. Graphene photonics and optoelectronics. *Nature Photonics*, 4(9):611–622, 2010.

[172] D. Alemu, H.-Y. Wei, K.-C. Ho, and C.-W. Chu. Highly conductive pedot:pss electrode by simple film treatment with methanol for ito-free polymer solar cells. *Energy & Environmental Science*, 5(11):9662–9671, 2012.

[173] A. Dhar and T.L. Alford. High quality transparent tio2/ag/tio2 composite electrode films deposited on flexible substrate at room temperature by sputtering. *APL Materials*, 1(1):012102, 2013.

[174] N.P. Sergeant, A. Hadipour, B. Niesen, D. Cheyns, P. Heremans, P. Peumans, and B.P. Rand. Design of transparent anodes for resonant cavity enhanced light harvesting in organic solar cells. *Advanced Materials*, 24(6):728–732, 2012.

[175] D.R. Sahu, S.-Y. Lin, and J.-L. Huang. Zno/ag/zno multilayer films for the application of a very low resistance transparent electrode. *Applied Surface Science*, 252(20):7509–7514, 2006.

[176] P. Tao, Y. Li, A. Rungta, A. Viswanath, J.N. Gao, B.C. Benicewicz, R.W. Siegel, and L.S. Schadler. Tio2 nanocomposites with high refractive index and transparency. *Journal of Materials Chemistry*, 21(46):18623–18629, 2011.

[177] D.-H. Kim, M.-R. Park, H.-J. Lee, and G.-H. Lee. Thickness dependence of electrical properties of ito film deposited on a plastic substrate by RF magnetron sputtering. *Applied Surface Science*, 253(2):409–411, 2006.

[178] J. Weickert, H. Sun, C. Palumbiny, H.C. Hesse, and L. Schmidt-Mende. Spray-deposited pedot: Pss for inverted organic solar cells. *Solar Energy Materials and Solar Cells*, 94(12):2371–2374, 2010.

[179] S. Messina, M.T.S. Nair, and P.K. Nair. Antimony sulfide thin films in chemically deposited thin film photovoltaic cells. *Thin Solid Films*, 515(15):5777–5782, 2007.

[180] K.L. Chopra, P.D. Paulson, and V. Dutta. Thin-film solar cells: an overview. *Progress in Photovoltaics: Research and Applications*, 12(2-3):69–92, 2004.

[181] R.L.Z. Hoye, K.P. Musselman, and J.L. MacManus-Driscoll. Research update: Doping zno and tio2 for solar cells. *APL Materials*, 1(6):060701, 2013.

[182] X. Chen and S.S. Mao. Titanium dioxide nanomaterials: synthesis, properties, modifications, and applications. *Chemical Reviews*, 107(7):2891–2959, 2007.

[183] A.R. Armstrong, G. Armstrong, J. Canales, R. García, and P.G. Bruce. Lithium-ion intercalation into tio2-B nanowires. *Advanced Materials*, 17(7):862–865, 2005.

[184] S.N. Habisreutinger, L. Schmidt-Mende, and J.K. Stolarczyk. Photocatalytic reduction of CO2 on tio2 and other semiconductors. *Angewandte Chemie International Edition*, 52(29):7372–7408, 2013.

[185] K. Miller, Kanwar S. Nalwa, A. Bergerud, N.M. Neihart, and S. Chaudhary. Memristive behavior in thin anodic titania. *Electron Device Letters, IEEE*, 31(7):737–739, 2010.

[186] C. Waldauf, M. Morana, P. Denk, P. Schilinsky, K. Coakley, S.A. Choulis, and C.J. Brabec. Highly efficient inverted organic photovoltaics using solution based titanium oxide as electron selective contact. *Applied Physics Letters*, 89(23):–, 2006.

[187] E. Zimmermann, T. Pfadler, J. Kalb, J.A. Dorman, D. Sommer, G. Hahn, J. Weickert, and L. Schmidt-Mende. Toward high-efficiency solution-processed planar heterojunction sb2S3 Solar cells. *Advanced Science*, 2(5), 2015.

[188] S A. Bretschneider, J. Weickert, J.A. Dorman, and L. Schmidt-Mende. Research update: Physical and electrical characteristics of lead halide perovskites for solar cell applications. *APL Materials*, 2(4):040701, 2014.

[189] V.E. Ferry, M.A. Verschuuren, M.C. van Lare, R.E.I. Schropp, H.A. Atwater, and A. Polman. Optimized spatial correlations for broadband light trapping nanopatterns in high efficiency ultrathin film a-si:h solar cells. *Nano Letters*, 11(10):4239–4245, 2011.

[190] W. Zhou, M. Tao, L. Chen, and H. Yang. Microstructured surface design for omnidirectional antireflection coatings on solar cells. *Journal of Applied Physics*, 102(10):103105, 2007.

[191] Y.-J. Lee, D.S. Ruby, D.W. Peters, B.B. McKenzie, and J.W.P. Hsu. Zno nanostructures as efficient antireflection layers in solar cells. *Nano Letters*, 8(5):1501–1505, 2008.

[192] E. Yablonovitch. Statistical ray optics. *Journal of the Optical Society of America*, 72(7):899–907, 1982.

[193] T.V. Amotchkina, M.K. Trubetskov, V. Pervak, and A.V. Tikhonravov. Design, production, and reverse engineering of two-octave antireflection coatings. *Applied Optics*, 50(35):6468–6475, 2011.

[194] A. Raman, Z. Yu, and S. Fan. Dielectric nanostructures for broadband light trapping in organic solar cells. *Optics Express*, 19(20):19015–19026, 2011.

[195] C. Haase and H. Stiebig. Thin-film silicon solar cells with efficient periodic light trapping texture. *Applied Physics Letters*, 91(6):061116, 2007.

[196] J. Zhu, C.-M. Hsu, Z. Yu, S. Fan, and Y. Cui. Nanodome solar cells with efficient light management and self-cleaning. *Nano Letters*, 10(6):1979–1984, 2009.

[197] M. Agrawal and P. Peumans. Broadband optical absorption enhancement through coherent light trapping in thin-film photovoltaic cells. *Optics Express*, 16(8):5385–5396, 2008.

[198] A.F. Lasagni, T. Roch, J. Berger, T. Kunze, V. Lang, and E. Beyer. To use or not to use (direct laser interference patterning), that is the question. In *SPIE LASE*, pages 935115–935115–7. International Society for Optics and Photonics, 2015.

[199] J. Weickert, E. Zimmermann, J.B. Reindl, T. Pfadler, J.A. Dorman, A. Petrozza, and L. Schmidt-Mende. Synergistic effects of interfacial modifiers enhance current and voltage in hybrid solar cells. *APL Materials*, 1(4):042109, 2013.

[200] J. Weickert and L. Schmidt-Mende. Perspective: Hybrid solar cells: How to get the polymer to cooperate? *APL Materials*, 1(2):020901, 2013.

[201] J. Weickert, F. Auras, T. Bein, and L. Schmidt-Mende. Characterization of interfacial modifiers for hybrid solar cells. *The Journal of Physical Chemistry C*, 115(30):15081–15088, 2011.

[202] P. Ehrenreich, T. Pfadler, F. Paquin, L.-I. Dion-Bertrand, O. Paré-Labrosse, C. Silva, J. Weickert, and L. Schmidt-Mende. Role of charge separation mechanism and local disorder at hybrid solar cell interfaces. *Physical Review B*, 91(3):035304, 2015.

[203] C.J. Brabec, S. Gowrisanker, J.J. Halls, D. Laird, S. Jia, and S. P. Williams. Polymer-fullerene bulk-heterojunction solar cells. *Advanced Materials*, 22(34):3839–56, 2010.

[204] G. Li, R. Zhu, and Y. Yang. Polymer solar cells. *Nature Photonics*, 6(3):153–161, 2012.

[205] F. Padinger, R.S. Rittberger, N.S. Sariciftci, et al. Effects of postproduction treatment on plastic solar cells. *Advanced Functional Materials*, 13(1):85–88, 2003.

[206] J. Peet, J.Y. Kim, N.E. Coates, W.L. Ma, D. Moses, A.J. Heeger, and G.C. Bazan. Efficiency enhancement in low-bandgap polymer solar cells by processing with alkane dithiols. *Nature materials*, 6(7):497–500, 2007.

[207] G. Dennler, M.C. Scharber, and C.J. Brabec. Polymer-fullerene bulk-heterojunction solar cells. *Advanced Materials*, 21(13):1323–1338, 2009.

[208] L.-M. Chen, Z. Hong, G. Li, and Y. Yang. Recent progress in polymer solar cells: Manipulation of polymer:fullerene morphology and the formation of efficient inverted polymer solar cells. *Advanced Materials*, 21(14-15):1434–1449, 2009.

[209] P.W.M. Blom, V.D. Mihailetchi, L.J.A. Koster, and D.E. Markov. Device physics of polymer:fullerene bulk heterojunction solar cells. *Advanced Materials*, 19(12):1551–1566, 2007.

[210] Z. He, C. Zhong, S. Su, M. Xu, H. Wu, and Y. Cao. Enhanced power-conversion efficiency in polymer solar cells using an inverted device structure. *Nature Photonics*, 6(9):591–595, 2012.

[211] F.C. Krebs, S.A. Gevorgyan, and J. Alstrup. A roll-to-roll process to flexible polymer solar cells: model studies, manufacture and operational stability studies. *Journal of Materials Chemistry*, 19(30):5442–5451, 2009.

[212] F.C. Krebs. All solution roll-to-roll processed polymer solar cells free from indium-tin-oxide and vacuum coating steps. *Organic Electronics*, 10(5):761–768, 2009.

[213] X. Guo, N. Zhou, S.J. Lou, J. Smith, D.B. Tice, J.W. Hennek, R.P. Ortiz, J.T.L. Navarrete, S. Li, J. Strzalka, L.X. Chen, R.P.H. Chang, A. Facchetti, and T.J. Marks. Polymer solar cells with enhanced fill factors. *Nature Photonics*, 7(10):825–833, 2013.

[214] W. Shockley and H.J. Queisser. Detailed balance limit of efficiency of pn junction solar cells. *Journal of Applied Physics*, 32(3):510–519, 1961.

[215] K. Vandewal, K. Tvingstedt, A. Gadisa, O. Inganas, and J. V. Manca. On the origin of the open-circuit voltage of polymer-fullerene solar cells. *Nature Materials*, 8(11):904–909, 2009.

[216] K. Vandewal, A. Gadisa, W.D. Oosterbaan, S. Bertho, F. Banishoeib, I. Van Severen, L. Lutsen, T.J. Cleij, D. Vanderzande, and J.V. Manca. The relation between open-circuit voltage and the onset of photocurrent generation by charge-transfer absorption in polymer:fullerene bulk heterojunction solar cells. *Advanced Functional Materials*, 18(14):2064–2070, 2008.

[217] M.T. Dang, L. Hirsch, and G. Wantz. P3Ht:pcbm, best seller in polymer photovoltaic research. *Advanced Materials*, 23(31):3597–3602, 2011.

[218] J. Niegemann, R. Diehl, and K. Busch. Efficient low-storage runge–kutta schemes with optimized stability regions. *Journal of Computational Physics*, 231(2):364–372, 2012.

[219] R. Meier, C. Birkenstock, C.M. Palumbiny, and P. Müller-Buschbaum. Efficiency-improved organic solar cells based on plasticizer assisted soft embossed pedot: Pss layers. *Physical Chemistry Chemical Physics*, 14(43):15088–15098, 2012.

[220] H. Wedemeyer, J. Michels, R. Chmielowski, S. Bourdais, T. Muto, M. Sugiura, G. Dennler, and J. Bachmann. Nanocrystalline solar cells with an antimony sulfide solid absorber by atomic layer deposition. *Energy & Environmental Science*, 6(1):67–71, 2013.

[221] J. Weickert, R.B. Dunbar, H.C. Hesse, W. Wiedemann, and L. Schmidt-Mende. Nanostructured organic and hybrid solar cells. *Advanced Materials*, 23(16):1810–1828, 2011.

[222] K.M. Coakley and M.D. McGehee. Conjugated polymer photovoltaic cells. *Chemistry of Materials*, 16(23):4533–4542, 2004.

[223] H. Yan, Z. Chen, Y. Zheng, C. Newman, J.R. Quinn, F. Dotz, M. Kastler, and A. Facchetti. A high-mobility electron-transporting polymer for printed transistors. *Nature*, 457(7230):679–686, 2009.

[224] J. Rivnay, M.F. Toney, Y. Zheng, I.V. Kauvar, Z. Chen, V. Wagner, A. Facchetti, and A. Salleo. Unconventional face-on texture and exceptional in-plane order of a high mobility n-type polymer. *Advanced Materials*, 22(39):4359–4363, 2010.

[225] J. Rivnay, R. Steyrleuthner, L.H. Jimison, A. Casadei, Z. Chen, M.F. Toney, A. Facchetti, D. Neher, and A. Salleo. Drastic control of texture in a high performance n-type polymeric semiconductor and implications for charge transport. *Macromolecules*, 44(13):5246–5255, 2011.

[226] D. Venkataraman, Serkan Yurt, B. Harihara Venkatraman, and N. Gavvalapalli. Role of molecular architecture in organic photovoltaic cells. *The Journal of Physical Chemistry Letters*, 1(6):947–958, 2010.

[227] D. Mori, H. Benten, I. Okada, H. Ohkita, and S. Ito. Highly efficient charge-carrier generation and collection in polymer/polymer blend solar cells with a power conversion efficiency of 5.7%. *Energy Environ. Sci.*, 7(9):2939–2943, 2014.

[228] M. Schubert, D. Dolfen, J. Frisch, S. Roland, R. Steyrleuthner, B. Stiller, Z. Chen, U. Scherf, N. Koch, A. Facchetti, and D. Neher. Influence of aggregation on the performance of all-polymer solar cells containing low-bandgap naphthalenediimide copolymers. *Advanced Energy Materials*, 2(3):369–380, 2012.

[229] N.D. Treat, M.A. Brady, G. Smith, M.F. Toney, E.J. Kramer, C.J. Hawker, and M.L. Chabinyc. Interdiffusion of PCBm and p3Ht reveals miscibility in a photovoltaically active blend. *Advanced Energy Materials*, 1(1):82–89, 2011.

[230] J.A. Bartelt, Z.M. Beiley, E.T. Hoke, W.R. Mateker, J.D. Douglas, B.A. Collins, J.R. Tumbleston, K.R. Graham, A. Amassian, H. Ade, J. M.J. Frechet, M.F. Toney, and M.D. McGehee. The importance of fullerene percolation in the mixed

regions of polymer-fullerene bulk heterojunction solar cells. *Advanced Energy Materials*, 3(3):364–374, 2013.

[231] N.C. Cates, R. Gysel, J.E.P. Dahl, A. Sellinger, and M.D. McGehee. Effects of intercalation on the hole mobility of amorphous semiconducting polymer blends. *Chemistry of Materials*, 22(11):3543–3548, 2010.

[232] M.L. Williams, R.F. Landel, and J.D. Ferry. The temperature dependence of relaxation mechanisms in amorphous polymers and other glass-forming liquids. *Journal of the American Chemical Society*, 77(14):3701–3707, 1955.

[233] T. Stübinger and W. Brütting. Exciton diffusion and optical interference in organic donor-acceptor photovoltaic cells. *Journal of Applied Physics*, 90(7):3632–3641, 2001.

[234] S.R. Scully and M.D. McGehee. Effects of optical interference and energy transfer on exciton diffusion length measurements in organic semiconductors. *Journal of Applied Physics*, 100(3):–, 2006.

[235] P. Müller-Buschbaum. The active layer morphology of organic solar cells probed with grazing incidence scattering techniques. *Advanced Materials*, 2014.

[236] M.A. Ruderer, C. Wang, E. Schaible, A. Hexemer, T. Xu, and P. Müller-Buschbaum. Morphology and optical properties of p3Ht:meh-cn-ppv blend films. *Macromolecules*, 46(11):4491–4501, 2013.

[237] E. Gann, A.T. Young, B.A. Collins, H. Yan, J. Nasiatka, H.A. Padmore, H. Ade, A. Hexemer, and C. Wang. Soft x-ray scattering facility at the advanced light source with real-time data processing and analysis. *Review of Scientific Instruments*, 83(4):045110, 2012.

[238] C. Wang, A. Hexemer, J. Nasiatka, E.R. Chan, A.T. Young, H.A. Padmore, W.F. Schlotter, J. Lüning, S. Swaraj, and B. Watts. Resonant soft x-ray scattering of polymers with a 2D detector: Initial results and system developments at the advanced light source. In *IOP Conference Series: Materials Science and Engineering*, volume 14, page 012016. IOP Publishing, 2010.

[239] A. Hexemer, W. Bras, J. Glossinger, E. Schaible, E. Gann, R. Kirian, A. MacDowell, M. Church, B. Rude, and H. Padmore. A saxs/waxs/GISaxs beamline with multilayer monochromator. In *Journal of Physics: Conference Series*, volume 247, page 012007. IOP Publishing, 2010.

[240] P. Müller-Buschbaum. Grazing incidence small-angle x-ray scattering: an advanced scattering technique for the investigation of nanostructured polymer films. *Analytical and Bioanalytical Chemistry*, 376(1):3–10, 2003.

[241] S.C.B. Mannsfeld. X-ray scattering: In tune with organic semiconductors. *Nature materials*, 11(6):489–490, 2012.

[242] B.A. Collins, J.E. Cochran, H. Yan, E. Gann, C. Hub, R. Fink, C. Wang, T. Schuettfort, C.R. McNeill, and M.L. Chabinyc. Polarized x-ray scattering reveals non-crystalline orientational ordering in organic films. *Nature Materials*, 11(6):536–543, 2012.

[243] O. Glatter and O. Kratky. *Small angle X-ray scattering*, volume 102. Academic press London, 1982.

[244] R.-J. Roe and R.J. Roe. *Methods of X-ray and neutron scattering in polymer science*, volume 739. Oxford University Press New York, 2000.

[245] N. Stribeck. *X-ray scattering of soft matter*. Springer, 2007.

[246] H. Yan, B.A. Collins, E. Gann, C. Wang, H. Ade, and C.R. McNeill. Correlating the efficiency and nanomorphology of polymer blend solar cells utilizing resonant soft x-ray scattering. *ACS Nano*, 6(1):677–688, 2011.

[247] S. Swaraj, C. Wang, H. Yan, B. Watts, J. Luning, C.R. McNeill, and H. Ade. Nanomorphology of bulk heterojunction photovoltaic thin films probed with resonant soft x-ray scattering. *Nano letters*, 10(8):2863–2869, 2010.

[248] J.M. Virgili, Y. Tao, J.B. Kortright, N.P. Balsara, and R.A. Segalman. Analysis of order formation in block copolymer thin films using resonant soft x-ray scattering. *Macromolecules*, 40(6):2092–2099, 2007.

[249] G.E. Mitchell, B.G. Landes, J. Lyons, B.J. Kern, M.J. Devon, I. Koprinarov, E.M. Gullikson, and J.B. Kortright. Molecular bond selective x-ray scattering for nanoscale analysis of soft matter. *Applied Physics Letters*, 89(4):044101, 2006.

[250] G. Materlik, C.J. Sparks, and K. Fischer. *Resonant anomalous X-ray scattering: theory and applications*. North-Holland Amsterdam, 1994.

[251] J. Nelson. *The physics of solar cells*, volume 57. World Scientific, 2003.

[252] J. Nelson, J. Kirkpatrick, and P. Ravirajan. Factors limiting the efficiency of molecular photovoltaic devices. *Physical Review B*, 69(3):035337, 2004.

[253] K. Vandewal, J. Widmer, T. Heumueller, C.J. Brabec, M.D. McGehee, K. Leo, M. Riede, and A. Salleo. Increased open-circuit voltage of organic solar cells by reduced donor-acceptor interface area. *Advanced Materials*, 2014.

[254] H. Hoppe and N.S. Sariciftci. Organic solar cells: An overview. *Journal of Materials Research*, 19(7):1925, 2004.

[255] M.M. Mandoc, W. Veurman, L.J.A. Koster, B. de Boer, and P.W.M. Blom. Origin of the reduced fill factor and photocurrent in mdmo-ppv:pcnepv all-polymer solar cells. *Advanced Functional Materials*, 17(13):2167–2173, 2007.

[256] M.M. Mandoc, F.B. Kooistra, J.C. Hummelen, B. De Boer, and P.W.M. Blom. Effect of traps on the performance of bulk heterojunction organic solar cells. *Applied Physics Letters*, 91(26):263505, 2007.

[257] O. Von Roos. Analysis of the photo voltage decay (PVd) method for measuring minority carrier lifetimes in p-n junction solar cells. *Journal of Applied Physics*, 52(9):5833–5837, 1981.

[258] L.J.A. Koster, V.D. Mihailetchi, R. Ramaker, and P.W.M. Blom. Light intensity dependence of open-circuit voltage of polymer: fullerene solar cells. *Applied Physics Letters*, 86(12):123509–123509–3, 2005.

[259] B. J. Leever, C.A. Bailey, T.J. Marks, M.C. Hersam, and M.F. Durstock. In situ characterization of lifetime and morphology in operating bulk heterojunction organic photovoltaic devices by impedance spectroscopy. *Advanced Energy Materials*, 2(1):120–128, 2012.

[260] H. Tang, K. Prasad, R. Sanjines, P.E. Schmid, and F. Levy. Electrical and optical properties of tio2 anatase thin films. *Journal of Applied Physics*, 75(4):2042–2047, 1994.

[261] T.M. Burke and M.D. McGehee. How high local charge carrier mobility and an energy cascade in a three-phase bulk heterojunction enable >90% quantum efficiency. *Advanced Materials*, 26(12):1923–1928, 2014.

[262] F.C. Jamieson, E.B. Domingo, T. McCarthy-Ward, M. Heeney, N. Stingelin, and J.R. Durrant. Fullerene crystallisation as a key driver of charge separation in polymer/fullerene bulk heterojunction solar cells. *Chemical Science*, 3(2):485–492, 2012.

[263] G.J. Hedley, A.J. Ward, A. Alekseev, C.T. Howells, E.R. Martins, L.A. Serrano, G. Cooke, A. Ruseckas, and I.D.W. Samuel. Determining the optimum morphology in high-performance polymer-fullerene organic photovoltaic cells. *Nature Communications*, 4, 2013.

List of Figures

List of Tables

Publications, Conferences and Teaching

List of Publications

Publications in Peer-Reviewed Journals

(11) **Pfadler, T.**; Kiel, T.; Stärk, M.; Werra J. F.M.; Matyssek Ch.; Boneberg, J.; Busch K.; Weickert, J. & Schmidt-Mende, L. *Structure-induced Resonant Tail-State Absorption in Polymer:Fullerene Bulk-Heterojunction Solar Cells*, **submitted 2015**.

(10) Kim, K.-D.; **Pfadler, T.**; Zimmermann, E.; Feng, Y.; Dorman, J.A.; Weickert, J. & Schmidt-Mende, L. *Decoupling Optical and Electronic Optimization of Organic Solar Cells using High-Performance Temperature-Stable TiO_2/Ag/TiO_2 Electrodes*, APL Materials, **2015**, 3, 106105.

(9) **Pfadler, T.**; Stärk, M.; Zimmermann, E.; Putnik, M.; Boneberg, J.; Weickert, J. & Schmidt-Mende, L. *A comparison of light-coupling into high and low index nanostructured photovoltaic thin films*, APL Materials, **2015**, 3, 066101.

(8) Zimmermann, E.; **Pfadler, T.**; Kalb, J.; Dorman, J.A.; Sommer, D.; Hahn, G.; Weickert, J. & Schmidt-Mende, L. *Toward High-Efficiency Solution-Processed Planar Heterojunction Sb_2S_3 Solar Cells*, Advanced Science, **2015**, 2, 1500059.

(7) Wisnet, A.; Bader, K.; Betzler, S.; Handloser, M.; Ehrenreich, P.; **Pfadler, T.**; Weickert, J.; Hartschuh, A.; Schmidt-Mende, L.; Scheu, C. & Dorman, J.A. *Defeating loss mechanisms in 1D TiO_2-based hybrid solar cells*, Advanced Functional Materials, **2015**, 25, 2601-2608.

(6) Ehrenreich, P.; **Pfadler, T.**; Paquin, F.; Dion-Bertrand, L.-I.; Paré-Labrosse, O.; Silva, C.; Weickert, J. & Schmidt-Mende, L. *Role of Charge Separation Mechanism and Local Disorder at Hybrid Solar Cell Interfaces*, Physical Review B, **2015**, 91, 035304.

(5) **Pfadler, T.**; Coric, M.; Palumbiny, C.M.; Jakowetz, A.C.; Strunk, K.P.; Dorman, J.A.; Ehrenreich, P.; Wang, C.; Hexemer, A.; Png, R.Q.; Ho, P.K.; Müller-Buschbaum, P.; Weickert, J. & Schmidt-Mende, L. *Influence of Interfacial Area on Exciton Separation and Polaron Recombination in Nanostructured Bi-Layer All-Polymer Solar Cells*, ACS Nano, **2014**, 8, 12397-409.

(4) Zimmermann, E.; Ehrenreich, P.; **Pfadler, T.**; Dorman, J.A.; Weickert, J. & Schmidt-Mende, L. *Erroneous efficiency reports harm organic solar cell research*, Nature Photonics, **2014**, 8, 669-672.

(3) Weickert, J.; Zimmermann, E.; Reindl, J.B.; **Pfadler, T.**; Dorman, J.A.; Petrozza, A. & Schmidt-Mende, L. *Synergistic Effects of Interfacial Modifiers Enhance Current and Voltage in Hybrid Solar Cells*, APL Materials, **2013**, 1, 042109.

(2) Dunbar, R.B.; **Pfadler, T.**; Lal, N.N.; Baumberg, J.J. & Schmidt-Mende, L. *Imprinting localized plasmons for enhanced solar cells*, Nanotechnology, **2012**, 23, 385202.

(1) Dunbar, R.B.; **Pfadler, T.** & Schmidt-Mende, L., *Highly absorbing solar cells - a survey of plasmonic nanostructures*, Optics Express, **2012**, 20, A177-A189.

Book Chapters

(2) **Pfadler, T.**; Palumbiny C.M.; Wojciech P.; Hesse H.C.; Feng X.; Müllen K.; Müller-Buschbaum P. & Schmidt-Mende L. *Controlled morphologies by molecular design and nano-imprint*, book chapter in *Advances in Polymer Science*, Springer, **2015**.

(1) Dorman, J.; **Pfadler, T.**; Weickert, J. & Schmidt-Mende, L. *Controlled Nanostructures in Organic and Hybrid Solar Cells*, book chapter in *Nanotechnology for Energy Conversion and Storage*, Wiley-VCH, **2015**.

Conferences, Workshops and Scientific Visits

2015

Annual Meeting of the German Physical Society (DPG), *Condensed Matter*; Berlin, Germany; 5 days conference

Final workshop in the DFG priority program SPP1355; Bad Honnef, Germany; 3 days; **poster presentation**

2014

MRS fall meeting; Boston, USA; 5 days conference; **poster presentation**

Annual Meeting of the German Physical Society (DPG), *Condensed Matter*; Dresden, Germany; 5 days conference; **oral presentation**

2013

International conference - Next Generation Solar Energy; Erlangen, Germany; 3 days; **poster presentation**

International conference - Nanosystems for Solar Energy Conversion; Munich, Germany; 3 days; **poster presentation**

Research visit of the group of Prof. Ron Naaman at the Weizmann Institute of Science; Rehovot, Israel; 14 days; **oral presentation**

International Workshop: Global Challenges – Opportunities for Nanotechnology; Venice, Italy; 4 days; **oral presentation and poster presentation**

DFG priority program SPP1355 spring school for Ph.D. students and Postdocs; Weinböhla, Germany; 4 days; **poster presentation**

Annual Meeting of the German Physical Society (DPG), *Condensed Matter*; Regensburg, Germany; 5 days conference; **poster presentation**

2012

Nanostructures as Efficient Solar Energy converters (NESEC); PROMES Laboratory Perpignan, France; 2 days conference; **oral presentation as invited speaker**

International Conference on Organic Photovoltaics; Würzburg, Germany; 1 day; **poster presentation**

DFG priority program SPP1355 workshop for Ph.D. students and Postdocs; Residenz Würzburg, Germany; 2 days; **poster presentation**

4th International Conference on Hybrid and Organic Photovoltaic (HOPV2012); Uppsala, Sweden; 4 days conference; **poster presentation**

Annual Meeting of the German Physical Society (DPG), *Condensed Matter*; Berlin, Germany; 5 days conference; **poster presentation**

Supervision and Teaching

Supervision

Master thesis Mihael Coric, University of Konstanz: *Nanostructured Bi-Layer in All-Polymer Solar Cells* (12 months)

Master thesis Karl-Philipp Strunk, University of Konstanz: *Excitonic Processes in Flat Heterojunction Organic Solar Cells* (12 months)

Bachelor thesis Samuel Greiner, University of Konstanz: *Local light intensity dependent device physics of organic bilayer solar cells* (4 months)

Bachelor thesis Karl-Philipp Strunk, University of Konstanz: *Inverted All-Polymer Solar Cells* (4 months)

Bachelor thesis Markus Ritter, University of Konstanz: *Flat junction evaporated organic solar cells featuring plasmonic up-conversion particles* (4 months)

Project Internship Jörg Roller, University of Konstanz: *Kontrollierte Nanostrukturen durch Anodisation von Aluminium* (3 months)

Teaching

SS2015 Lecture *Organic Solar Cells*, University of Konstanz (giving the tutorial)

WS2014/15 Tutorial for the lecture *Integrated Cours 1 (IK1) for Physicists*, University of Konstanz

SS2014 Seminar (Master course), *Integriertes Studentenseminar: Photonik und Plasmonik*, University of Konstanz

WS2013/14 Seminar (Master course), *The physics of organic and hybrid organic/inorganic solar cells*, University of Konstanz

SS2013 Lecture *Organic Solar Cells*, University of Konstanz (giving 1/3 of the lectures and the tutorial)

WS2012/13 Tutorial for the lecture *Integrated Cours 1 (IK1) for Physicists*, University of Konstanz

Acknowledgement

In retrospective, a dissertation is a long-term experience of ups and downs, profoundly affected by enlightening realizations based on trial and error along with an extensive study of literature. It was not only the comprehensive scientific but also the personal input of my supervisor, my collaboration partners, my colleagues, my friends and my family who altogether contributed in their own way to make this a very enjoyable time. Therefore, it is a sincere pleasure for me to thank all of those in particular who helped me with my dissertation.

First, I like to show my gratitude to Prof. Lukas Schmidt-Mende for his comprehensive supervision and guidance during the past years. Lukas, I am especially grateful for the freedom you gave me to follow my interests by designing and carrying out my own projects. I am equally thankful that you always took time to discuss my results and to give me direction.

I also want to thank Prof. Johannes Boneberg for the scientific input he gave me, the great collaboration we had, and that he always provided time to support me. Johannes, it was your suggestion at the very beginning of my time in Konstanz to elaborate the applicability of direct laser interference patterning to functional materials like TiO_2 that brought me to the investigation of photonic structures in organic solar cells.
In this regard, my further thanks go to Martin Stärk, a Ph.D. student of Johannes and an expert in laser patterning, for providing several hours every week over a period of one and a half years to achieve our goals, even though it was never his main project. Martin, your help on this project was crucial for its final success and I further thank you as a friend for making my time in Konstanz so enjoyable.

Throughout my dissertation I took pleasure in visiting conferences, discussing results and projects with collaborators, and sharing my interests in science with researchers from all over the world. I would like to thank Claudia Palumbiny (TUM) for the great time we had at conferences and for successfully collaborating in a shared DFG project. Claudia, I really appreciate your achievement of convincing the scientists from the ALS in Berkley to help us with our sophisticated measurements, which turned out to be suitable to check the resolution limit of their instruments. This was the reason for them being tremendously interested and supportive and therefore complemented our research. Furthermore, I would like to say thank you to Thomas Kiel, Julia Werra and Christian Matyssek (HU Berlin) for their great theoretical input to our shared project on structured thin-film solar cells. I regret having only met them once at the annual

meeting of the DPG to discuss our results, but I will never forget Thomas' honest enthusiasm for your computational approach. Your great contribution to the project made it so special. Moreover, I would like to thank my collaborators from Singapore. Prof. L.-L. Chua and her team for providing the cross-linking molecules and Prof. Peter Ho and Dr. Rui-Qi Png for giving valuable feedback to our project. Although we never met, we were able to walk away with a fruitful collaboration.

I would like to thank all people from the Schmidt-Mende group for the great time we had in the lab, during coffee breaks or when we had barbecue together. I specifically enjoyed having a shared project with Dr. Kwang-Dae Kim. KD, I have never met a person like you - your precision, your work ethic and your very successful lab work ineffably accelerated progress in our project.
I am grateful to Eugen Zimmermann for being such a cheerful person. Eugen, thank you for helping me with programming details in situations when my patience was about to run out.
I am also very grateful to Philipp Ehrenreich and Martin Putnik. It was always scientifically as well as personally entertaining to work with you two guys. The great time we had outside work when going out to the Strandbar or to Berrys. A special thanks to you Philipp for the restorative cycling tours we had and thank you Martin for going hiking and skiing with me. Martin, your indescribable way to laugh was always the best medicine against bad mood.
I was lucky enough to supervise exclusively great students during my time in Konstanz. Thank you Mihi, Kalli, Sammy and Markus for your trust, hard work and patience. It was a pleasure working with all of you and I want to express my gratitude for the chance to meet each single one of you.
I also would like to express my deep gratitude to my colleagues from Munich who started with me in Konstanz and Dr. Michael Krumm who I met in Konstanz. Especially the first summer at lake Konstanz was awesome - swimming, playing beach volleyball and having several barbecues and beers every week felt like being permanently on vacation. Thank you Julian R., Max S., Andi J., Severin H., and Michi K. for the great start we had together.
Most importantly, I want to thank the persons I was working with the most time. Having such nice colleagues made the scientific work feel like meeting friends and sharing common interests. Thanks to all of you: Julian K., Matthias, Maren, Simon, Susi, Yuyi, Alex, Kevin, Hao, Chaw Loon, William, Said, Luis, Sajad and Christina.

I strongly acknowledge Dr. James Dorman and Dr. Jonas Weickert for accompanying my whole Ph.D. In general, you two were the ones leading the projects in our group to success. Thank you for involving me in your discussions and decisions. James, thank you for always helping me when I was not sure on how to formulate specific ideas in written English. You my friend, had a formative influence on my time in Konstanz. Jonas, thanks for being my friend, mentor and drinking buddy. On the one hand, we never stopped to puzzle over science even when things got more and more complex. On the other hand, we never stopped having fun and continued joking even though our

sense of humor turned out to be black as cole. I additionally do not want to miss the great time we always had with your lovely wife Sabrina and your awesome son Tammo.

Finally, I want to thank those people who make my life complete: my friends, my girlfriend Jenny, and my family.
Having finally become a physicist is largely based on my father's positive influence. My entire childhood, you already taught me a lot of helpful things. I esteem your honest scientific interest by constructing Stirling engines, by building up electronic devices, and your interest in amateur radio. Things you do in your spare time and not for your publication list or career.

Special thanks goes to Lukas, Jonas, James, my friend Tobi, Jenny, and my father for revising sections of this thesis and for giving valuable feedback.